TRANSIENTS

WORKING GROUP FINAL REPORT

P. García-Lario[1], A. Coulais[2], D. Kester[3], E. Caux[4],

with the collaboration of:

A. Abergel[2], P. Ábráham[5], J. Acosta-Pulido[1,6], B. Ali[7], C. Gabriel[1], B.I Fouks[8], K. Ganga[7], F. Lahuis[3], R. Laureijs[1], T. Lim[9], M.-A. Miville-Deschênes[2], A. Noriega-Crespo[7] S. Pezzuto[10], B. Schulz[1], R.J. Tuffs[1]1

SAI/2000-057/Dc, Version 0.7

March 22, 2001

[1] ISO Data Centre, Astrophysics Division, Space Science Department of ESA, Villafranca, P.O. Box 50727, E-28080 Madrid, Spain
[2] Institut d'Astrophysique Spatiale, Universite d'Orsay, F-91405 Orsay, France
[3] SRON, P.O. Box 800, NL-9700 AV Groningen, The Netherlands
[4] Centre d'Etude Spatiale des Rayonnements, CNRS-UPS, BP 4346, F-31028 Toulouse, CEDEX 04, France
[5] Max-Planck-Institut für Astronomie, Königstuhl 17, D-69117 Heidelberg, Germany
[6] Instituto de Astrofísica de Canarias, C/ Via Láctea s/n, E-38200 La Laguna, Tenerife, Spain
[7] Infrared Processing and Analysis Center, Caltech, Mail Code 100-22, 770 S. Wilson Avenue, Pasadena, CA 91125, USA
[8] Institute of Radioengineering and Electronics, Russian Academy of Sciences, Mokhovaya Str., 11, GSP-3, Moscow, 103907, Russia
[9] Rutherford Appleton Laboratory, Chilton, Didcot, Oxon OX11 0QX, UK
[10] Istituto di Fisica dello Spazio Interplanetario - CNR, Via Fosso del Cavaliere, I-00133 Roma, Italy
[11] Max-Planck-Institut für Kernphysik, Saupfercheckweg 1, D-69117 Heidelberg, Germany

Document Information

Document:	Transients WG Final Report
Title:	Transients WG Final Report
Reference Number:	SAI/2000-057/Rp
Issue:	Draft Version 0.7
Issue Date:	22 March 2001
Authors:	P. Garcia-Lario

Document Change Record

Date	**Revision**	**Comments**
15 November 2000	Version 0.1	First Draft
15 January 2001	Version 0.5	Change of structure
02 March 2001	Version 0.6	Bibliography added
22 March 2001	Version 0.7	Some sections expanded

Contents

1 Introduction **6**

1.1 Purpose of the Transients WG 6

1.2 Transients WG Webpage 6

2 Transient effects in IR detectors **7**

2.1 A description of the problem 7

2.2 Physical and empirical models 8

2.3 Applicability of models as a function of the detector material in ISO detectors . . 10

2.3.1 Si:Ga detectors on board ISO 10

2.3.2 Ge:Ga detectors on board ISO 10

3 Transient effects in PHT data **12**

3.1 Impact on PHT detectors 12

3.1.1 Introduction 12

3.2 Efforts developed to correct PHT data for transient effects 15

3.2.1 Transient effects in staring PHT-P and PHT-C observations: Drift recognition 15

3.2.2 Applicability of Fouks-Schubert method to PHT-S and PHT-P observations 15

3.2.3 Transient corrections in PHT-S chopped measurements 16

3.2.4 Dynamic calibration of PHT-S staring measurements 20

3.2.5 Empirical solution for ISOPHOT far-IR detectors P3 and PHT-C: staring observations 28

3.2.6 Transient effects in chopped PHT-P and PHT-C observations 33

3.2.7 Transient effects in PHT32 chopped raster maps 34

3.2.8 Transients in Ge:Ga PHT C-100 detectors: an empirical non-linear approach 35

3.2.9 Detector responsitivity drifts 36

3.2.10 Observing strategies developed during operations 39

3.3 Results achieved 40

3.3.1 Drift recognition *vs* empirical models in staring PHT-P and PHT-C observations 40

3.3.2 Calibration of PHT-S chopped observations 40

3.3.3 Dynamic calibration of PHT-S staring measurements 41

3.3.4 Transient effects in PHT32 chopped raster maps 42

3.3.5 Transients in Ge:Ga PHT C-100 detectors 42

3.4 Implementation in PIA/PHT pipeline 50
3.4.1 Transient corrections in PIA 50
3.4.2 Transient corrections in OLP 51

4 Transient effects in SWS data 54
4.1 Impact on SWS detectors 54
4.2 Efforts developed to correct SWS data for transient effects 55
4.2.1 Memory effects in band 2 data 55
4.2.2 Memory effects in band 4 data 63
4.2.3 Memory effects in the Fabry-Pérot bands 63
4.2.4 The 'Pulse-shape' correction 63
4.3 Results achieved 64
4.3.1 Adapted Fouks-Schubert method applied to band 2 data 64
4.4 Implementation in OSIA/pipeline 72

5 Transient effects in CAM data 73
5.1 Impact on CAM detectors 73
5.2 Efforts developed to correct CAM data for transient effects 74
5.2.1 Transient effects in SW detectors 74
5.2.2 Transient effects in LW detectors 76
5.2.3 Cross-talk : the problem with point sources 77
5.2.4 Application of inversion methods to CAM-LW detectors 80
5.2.5 Spatial and temporal filterings: use of redundancy 80
5.3 Results achieved 82
5.3.1 Transient correction in SW detectors 82
5.3.2 Transient correction under quasi-uniform illumination in LW detectors . . 83
5.3.3 Transient correction of point sources 84
5.3.4 The use of redundancy in raster maps 87
5.4 Implementation in CIA/pipeline 88

6 Transient effects in LWS data 89
6.1 Impact on LWS detectors 89
6.2 Efforts developed to correct LWS data for transient effects 90
6.3 Results achieved 93
6.4 Implementation in LIA/pipeline 93

7 Lessons applicable to the Future 94
7.1 Acknowledgements 95

A 99
A.1 SWS: Some Algebra used in the application of Fouks-Schubert model to band 2 99
A.2 SWS: Temperature Dependency 100
A.3 SWS: Error messages in DYNADARK and subsidiaries. 100

B **103**
B.1 Inversion methods 103
B.1.1 Inverse problems 103

C **105**
C.1 Implementation of the dynamic calibration method in PIA 105
C.1.1 Program to fit Chebyshev polinomials to a given measurement 105
C.1.2 Program to select best Chebyshev polinomials to a given measurement . . 107

D **109**
D.1 Documentation 109
D.1.1 Technical Reports/Papers 109
D.1.2 Relevant contributions presented at the ISO Calibration Legacy Conference 110
D.1.3 A bibliographic database on 'Transients in IR detectors' 110

Chapter 1

Introduction

The Transients Working Group is one of the eight Calibration Working Groups constituted at the ISO Data Centre to address different calibration topics during the Post-Operational Phase of the ISO Project in the framework of the global ISO (Cross-)Calibration strategy.

The Working Group scheme was ideated as a platform to exchange knowledge and progress between the members of each of these Working Groups, across instrument boundaries and major themes of common interest.

1.1 Purpose of the Transients WG

The purpose of the Transients WG, as stated in the ISO (Cross-)Calibration Plan for Post-Operations, is to:

- Characterize transient effects in the 4 ISO instruments and determine the best correction method as a function of detector type, observing mode and characteristics of the source, estimating the effects on photometric accuracy.
- Develop S/W tools to detect and correct transient effects and make these tools available to the ISO users community as part of the Interactive Analysis (IA) S/W packages and, eventually, implement these tools in the Off-Line Processing (OLP).

1.2 Transients WG Webpage

The Transients WG WWW page is maintained by P. García-Lario at

`http://isowww.vilspa.esa.es:1909/~pgarcia/transients_html/index.html.`

This page contains information on the latest meetings held by the Working Group, including in most cases the viewgraphs there presented, as well as a bibliographic database of documents (from internal reports just for internal circulation to papers published in refereed journals) related with this calibration topic.

Chapter 2

Transient effects in IR detectors

The operation of InfraRed (IR) detectors in space is strongly complicated by memory effects, which may have a strong amplitude due to the low brightness of the sky at these wavelengths. For this reason these detectors exhibit very long-term transient currents under flux changes. The time allocated for the observation of an astronomical source is strictly restricted because of the large number of astronomical sources to be observed. Therefore, it is usually not possible to wait for current stabilization when the detector is exposed in space to sources of infrared emission, making the determination of the input fluxes a very difficult task.

From the transient problem point of view, the ISO satellite (Kessler et al. 1996) is a very interesting laboratory since several technologies (Ge:Be, Ge:Ga, In:Sb, CID In:Sb, Si:As, Si:Ga, Si:B) (Cesarsky et al. 1996; Clegg et al. 1996; de Graauw et al. 1996; Lemke et al. 1996) have been used to cover an extended spectral range from 2.5 to 250 μm. Four years after the end of the mission, transient effects are still under study in order to increase the final sensitivity of ISO. Without any correction, the errors can be as large as 50 % in some cases. However, under certain circumstances, the response after a flux change in some of the ISO detectors and observing modes is highly reproducible, which gives sense to look for models and to correct the data for these transient effects.

2.1 A description of the problem

Let n be the index of the sky position of the satellite and t the time at the end of each integration. Elementary measurements of the detector at the end of each integration time are readouts $J_n(t)$. Generally, each readout is computed from the curve which gives the evolution of the number of charges as a function of the integration time (the "ramps", containing non destructive measurements between resets). This operation may be not trivial because of non linearities of the electronics and glitches due to high energetic particles. In the case of PHT (see ISOPHOT Handbook - Laureijs et al. 2000) and LWS (Leeks et al. 1999), the ramps are adjusted with a low order polynomial. For CAM, only 2 points are measured due to telemetry limitations. Systematic errors coming from this step are not considered here.

Because of memory effects, each position n on the sky is observed during several readouts; this set of readouts gives the block n. Let us note t_n, the instant of flux changes and J_n^∞ the value of the readouts when the stabilization is achieved over the n-th block. This current J_n^∞ is proportional (Fouks & Schubert 1995) to the constant incoming flux observed during this n-th block. Corresponding readouts are denoted $J_n(t)$ for $t \in [t_n, t_{n+1}[$.

	detector name	type	wavelength (μm)	pixels
CAM	SW	CID In:Sb	2.5 – 5.5	32×32
	LW	Si:Ga	4. – 18.	32×32
PHT	S1 & S2	Si:Ga	15, (peak)	two 1
	P1	Si:Ga	15. (peak)	1
	P2	Si:B	25. (peak)	1
	P3	Ge:Ga	100. (peak)	1
	C 100	Ge:Ga	100. (peak)	3×3
	C 200	Ge:Ga (stressed)	180. (peak)	2×2
SWS	band 1	In:Sb	2.4 – 4.1	1×12
	band 2	Si:Ga	4.1 – 12	1×12
	band 3	Si:As	12. – 29.	1×12
	band 4	Ge:Be	29. – 45.2	1×12
	FP band 5	Si:Sb	11.4 – 26.	1×2
	FP band 6	Ge:Be	26. – 44.5	1×2
LWS	SW1	Ge:Be	43. – 50.	1
	SW2-SW5, LW1	Ge:Ga	50 to 110 (10)	five 1
	LW2-LW5	Ge:Ga (stressed)	110 to 190 (20)	four 1

Table 2.1: List of the IR detectors on-board ISO with indications of type, operating wavelengths (peak or range) and detector topology (individual pixel, linear or matrix array).

2.2 Physical and empirical models

Before the launch of ISO, ground based tests were extensively performed (CAM - Pérault et al. 1994 -, PHT - Groezinger et al. 1992; Schubert et al. 1994; Schubert 1995 - and SWS - Wensink et al. 1992). Unfortunately, as a result of these ground based tests it was not possible to develope an accurate model for transients in SWS and CAM prior to launch. Only for PHT-S a promising non linear model was proposed (Fouks & Schubert 1995). However, several problems were found produced by temperature variations due to the Cold Readout Electronic (CRE) and CRE CMOS transistors latch-ups (see ISOPHOT Handbook - Laureijs et al. 2000). As a consequence of this, the initial model was modified in order to include a temperature variation correction (Fooks & Schubert 1995; Schubert et al. 1994).

Later, during the ISO mission, several linear and non-linear models were suggested for the various ISO instruments and observing modes. It became evident that the models must be non-linear and non-symmetrical and must take into account the history of the illumination of the pixels.

Such analytical models have been developed for IR detectors by Vinokurov & Fouks (1991) from the non-linear equations (Vinokurov & Fouks 1991; Haegel et al. 1999) describing such detectors. One of these models, the so-called Fouks-Schubert model, was the one used for describing transients in PHT-S detectors during ground based tests (Fouks & Schubert 1995; Schubert 1995; Schubert et al. 1995; Schubert et al. 1994) as we have already mentioned. We indicate here the formula (Fouks & Schubert 1995; Coulais & Abergel 2000) when starting from an unstabilized current J_{n-1}^{end} at the end of block $n-1$:

$$J_n\left(t\right) = \beta J_n^{\infty} + \frac{\left(1-\beta\right) J_n^{\infty} \left(J_{n-1}^{end} - \beta J_{n-1}^{\infty}\right)}{\left(J_{n-1}^{end} - \beta J_{n-1}^{\infty}\right) + \left[\left(1-\beta\right) J_n^{\infty} - \left(J_{n-1}^{end} - \beta J_{n-1}^{\infty}\right)\right] exp\left(-J_n^{\infty} t/\lambda\right)} \tag{2.1}$$

where the time t is measured from an arbitrary instant after the flux change at time $t=0$, β is the instantaneous jump and λ is a constant. The unstabilized current J_{n-1}^{end} before the flux change reflects the history of the detector (stabilization in block $n-1$ is achieved when $J_{n-1}^{end} = J_{n-1}^{\infty}$); J_n^{∞} is the steady-state current under the constant incoming flux during block n. This simple non-linear analytical formula (Eq. 2.1), which takes into account the memory effects, is directly derived from a set of conventional 1-D physical equations. These equations describe the processes in the detector bulk, with the use of Fouks' boundary condition (Fouks, 1981) that describes the properties of the detector contacts. This boundary condition has been used in the form :

$$p\,(0,t) = p\,(0,0)\,exp\left[\frac{\Delta E\,(0,t)}{E_j}\right] \tag{2.2}$$

where $p\,(z,t)$ is the hole concentration at the plane z measured from the injecting contact placed at the plane $z = 0$, the time t is measured from an arbitrary instant, as in Eq. (2.1), $\Delta E\,(0,t)$ is the change of the near-contact field with time ($\Delta E(0,t) = E(0,t) - E(0,0)$), and E_j is the characteristic of the injection ability of the contact. Eq. (2.2) permits to describe the contact properties with a high exactness (Fouks & Schubert 1995) and, in addition, to take into consideration additional technological and engineering effects inherent to real detectors (Fouks, 1997).

The use of Eq. (2.2) instead of a detailed consideration of the processes which occur inside the near-contact space-charge region highly simplifies the description of transient currents. Nevertheless, in general the problem remains rather complex even after this simplification. However, in the case where E_j is much less than the steady-state field in the detector bulk, $E_0 = V_0/l$ (where V_0 is the steady-state voltage applied to the detector, l is the inter-contact distance), this description can be additionally strongly simplified, and Eq. (2.1) serves as a very exact description for transient currents (Vinokurov & Fouks 1991). The parameter E_j quantifies the quality of the contacts and depends on the flatness of the donor profile in the near-contact region and is linked to the time constant of the current relaxation. The higher the contact quality, the less is E_j, and the shorter the time constant. In real detectors at liquid helium temperatures E_j is of the order of 10^2-10^3 V/m. For Si:Ga detectors E_0 is considerably high, typically 10^5-10^6 V/m, which provides a very high exactness to Eq. (2.1). In Ge:Ga detectors E_0, however, E_0 is of the order of E_j, thus making this formula not so exact.

The other important point lies in the fact that Eq. (2.1) is applicable only in the case where the illumination is uniform on the pixel surface. In this case high photoelectric non-stationary cross-talkings between adjacent pixels, that are inherent to such detectors (Fouks & Schubert 1995), compensate each other, which makes the electric field uniform along the planes z and the used 1-D equations true. Under non-uniform illumination the set of 1-D equations cannot be used, and Eq. (2.1) looses its exactness (Vinokurov & Fouks 1988; Vinokurov et al. 1992).

In the case of Ge:Ga detectors and at the present time, outside ISO teams, the two main groups studying Ge:Ga detector transients are Nancy Haegel's team (Haegel et al. 1999) and Boris Fouks' team (Fouks 1992). Haegel's team has developed numerical codes in order to solve the set of non-linear differential equations constrained by some boundaries conditions. After improving their code in order to be able to compute transients for thicker bulks and for low levels, they are working now on the problem of transients under non-uniform illumination. Fouks' team solved their general model, in first turn, by analytical methods. This highly simplifies the solutions, alleviates the comprehension of the physics of the observed phenomena, and permits not only to consider the behavior of an ideal detector, but also to include into consideration a lot of additional essential phenomena which appeared as a consequence of the use of real technology and design peculiarities of the detectors. However, following Fouks classification (Vinokurov & Fouks 1991; Fouks 1992) based on the ratio E_0/E_j, and as we have already mentioned, for Ge:Ga detectors we are unfortunately always in an unfavourable domain and the expected exactness of such simplified analytical models, even if the detector is perfect, is only about 10-20

%. Fouks' team has also made computative descriptions for some transient curves observed in Ge:Ga detectors (Fouks 1992). However, up to now none of these two approaches have been applied on real data to correct the Ge:Ga transients.

2.3 Applicability of models as a function of the detector material in ISO detectors

2.3.1 Si:Ga detectors on board ISO

Several Si:Ga detectors were on-board ISO (Table 2.1) : the LW 32×32 matrix array of the CAM (Cesarsky et al. 1994, 1996), camera, three detectors of the PHT (Lemke et al. 1996) photometer (S1, S2 and P) and one 1×12 linear array of the SWS (de Graauw et al. 1996) short wavelength spectrometer (band 2).

For uniform illuminated Si:Ga detectors, as we have already mentioned, very good results have been obtained with the Fouks model as a first order model, the accuracy improving from ∼10 % with previous models (Abergel et al. 2000) to ∼1 % with this one (Coulais & Abergel 2000). After this model is applied other effects, such as small oscillations, long term drift, cross-talk between pixels, or the change of detector parameters at the sides of the matrix detectors, become the main problems to be resolved.

A good transient correction using the Fouks-Schubert model needs of well pre-processed raw data. Especially the subtraction of the dark level must be as precise as possible. For CAM-LW (Biviano et al. 1998) and SWS (Kester 1999), the dark correction has to include temporal variations.

2.3.2 Ge:Ga detectors on board ISO

Several Ge:Ga detectors were set up for the ISO satellite (Table 2.1) : one detector and two small matrix arrays for PHT (Lemke et al. 1996; Wolf 1994) (P3, C-100 3×3 pixels, stressed C-200 2×2 pixels), and several stressed (4) and un-stressed (5) monolithic detectors for LWS (Clegg et al. 1996, Church et al. 1993; Wolf 1994). All of these detectors are affected by transient effects which can bias the final photometry typically from 10 to 40 %. Some of them present a hook response (quick overshoot) for high upward steps of flux. These transients appear, in principle, easier to modelize than the Si:Ga ones because they are at a first order exponential (Church et al. 1993; Clegg et al. 1996) and have no inflection point. Thus, the use of non-linear models seems to be less necessary in order to take into account the memory effect. However, the correction cannot be as precise as the one obtained for Si:Ga detectors using non-linear models.

The present status on transients for the Ge:Ga detectors is less favorable than for Si:Ga detectors and can be characterised in the following way :

- each Ge:Ga detector seems to require a peculiar model,
- several fitting methods are available in the PIA software used for interactive analysis of the PHT data (Gabriel & Acosta-Pulido 1999), but no peculiar model has definitively been assigned to each of the Ge:Ga detectors used by PHT;
- a empirical model based on the Fouks-Schubert model has been developed for several bands of LWS, with a clear improvement on the shape of the spectral lines (Caux 1999). However, in all cases, non-linear models were needed to reproduce properly the memory effects.

In summary, several conclusions can be extracted :

- no universal model like Fouks model for Si:Ga has been pointed out,
- the linear models based on fitting 2 or 3 exponentials did not work on a wide dynamical range for these detectors (Church er al. 1992; Church et al. 1996),
- empirical non-linear models give interesting but not definitive results, at the price of huge work,
- the use of an extended calibration database is in any case essential to build realistic models of the transient response.

Chapter 3

Transient effects in PHT data

3.1 Impact on PHT detectors

The calibration of ISOPHOT observations is hampered in many cases by the transient response of the detectors. Here we outline the behaviour observed in-flight for the different ISOPHOT detectors. We also present some of the procedures which are currently used to correct transient effects and their implementation in PIA and/or in the pipeline.

3.1.1 Introduction

ISOPHOT is one of the four scientific instruments on board the ISO satellite. It consists of three subsystems: (i) an aperture photopolarimeter, with three different single pixel detectors (P1, P2 and P3), (ii) a grating spectrophotometer, containing two 64 pixel arrays (SS and SL), and (iii) two far-IR cameras of 9 (C100) and 4 pixels (C200), respectively. P1 and SS/SL use Si:Ga photoconductors as detector elements, P2 uses Si:B, whereas P3 and C100 use unstressed and C200 stressed Ge:Ga detectors, respectively. A more detailed description of ISOPHOT observing capabilities and performance can be found in Lemke et al. (1993 and 1996).

One challenge in the calibration of the ISOPHOT instrument is the transients in the signals of the detectors. Transient effects are a typical behaviour of extrinsic photoconductors, as used in ISOPHOT, if they are operated at low temperatures and are exposed to low background illumination. A generally observed effect is a slow response after a change in the illumination. One of the main reasons for this behaviour is the use of implanted contacts, needed to achieve ohmic contact between the metallic wire and the photoconductor (see for example Haegel, Latasa & White, 1993).

Following ground based experiments, PHT-P2 (Si:B) was found to be affected in a very limited way by transients, while the most important effects were observed in the Si:Ga detectors used by PHT-P1 and PHT-S (SS/SL) and in the Ge:Ga detectors used by PHT-P3 and the C100 and C200 arrays.

Typical drift curves are presented in Figure 3.1 In case of a flux drop, a signal decay and in case of increasing flux steps a signal rise (Fig. 3.1) is observed. The doped silicon detectors (SS, SL, P1, and P2) exhibit a hook response during the first 40 seconds after large positive flux steps (Figure 3.1b). The signal shows a behaviour similar to a strongly damped oscillation around the asymptotic level. For even higher flux steps the signal behaviour can be restricted to an overshoot followed by a slow decay.

The characteristic stabilisation time scales depend on (1) the detector material, (2) the flux change, (3) the illumination level, and (4) the temperature of the detector. They vary from a few seconds up to several minutes.

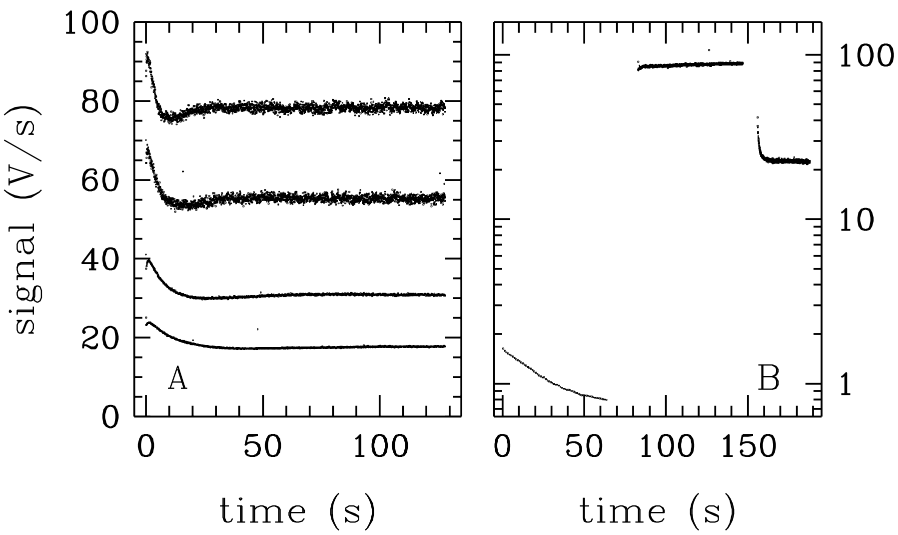

Figure 3.1: *Examples of P1 detector transients. Left panel (A): multi-filter observation of the star HR 6705, filter sequence P_16 (64 s integration), P_3.6 (64 s) followed by the P_3.6 (32 s) FCS measurement. Both the P_16 as well as the P_3.6 FCS measurement show a downward drift, with a longer stabilization time for thr fainter P_16 signal. Right panel (B): 4 transient curves after a flux step overplotted in the same graph for comparison, the highest curve corresponding to the largest positive flux step. In all cases the signal prior to each step was the same and had a strength of about 35 V/s. For these flux steps a signal overshoot is detected followed by a strongly damped oscillation.*

Typical timescales for stabilisation after a given flux step for the PHT-SS/SL detectors are presented in Table 3.1. These timescales can be taken as approximate values for detector P2 and lower limits for P1. The stabilisation time is defined as the time after a flux step to reach 90% of the signal at t = ∞ (S_∞).

Note, that a signal of 0.5 mV/s is very close to the dark signal and - in practice - cannot be determined accurately. The relative stabilisation time is faster for positive flux steps - cf. Table 3.1 values below the diagonal versus those above the diagonal. Flux steps at low flux levels will take more time to stabilise. However, in such cases the S/N and the detector stability (see Section 3.2.9) might be more important.

The doped germanium detectors P3 and C100 tend to stabilise faster than the doped silicon detectors. C200 shows the shortest transient time scales. Typical time scales are 100 s for P3 and C100 and 40 s for C200, respectively.

For chopped measurements the same drift behaviour description applies. Due to the chopper modulation, the signal evolution on each chopper plateau can be regarded as a drift curve after a flux step. Consequently, the difference signal between the on- and off-target chopper plateaux is not only a function of flux step, but also a function of chopper frequency. Without applying drift corrections use of the difference signal seriously underestimates the actual flux of the target. It has been observed that the signal differences between neighbouring chopper plateaux remain stable, even in case of a measurement containing a general drift (see Section 3.2.9), provided that the flux difference between the chopper plateaux is less than 50% of the total signal. An example of a chopped measurement with P2 is presented in Fig. 3.2.

Table 3.1: *Stabilisation times for a given flux step in seconds. The first row lists the initial signal, the first column the final signal in V/s.*

	$5\ 10^{-4}$	0.001	0.01	0.1	1	10
$5\ 10^{-4}$	...	6800	11500	11880	11900	11900
0.001	4070	...	5570	5900	5960	5960
0.01	1500	1220	...	560	592	595
0.1	240	210	122	...	55	59
1	32	30	21	12	...	5
10	4	4	3	2	1	...

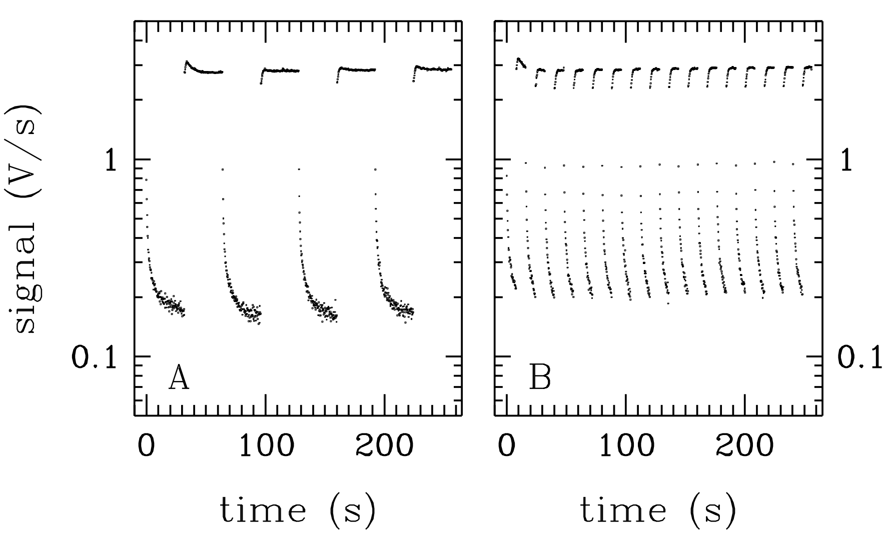

Figure 3.2: *Examples of P2 detector transients induced by the chopper modulation on a very high source-background contrast. Left panel (A): slow (32 s per chopper plateau) chopped measurement on a high source-background contrast. Right panel (B) same source-background contrast as (A) but with a higher chopper frequency (8 s per plateau). Note the strong overshoot in the first higher plateau; a straight signal average per chopper plateau would underestimate the background subtracted source signal in both cases.*

3.2 Efforts developed to correct PHT data for transient effects

Full transient correction methods are, in the case of ISOPHOT, restricted to PIA in most cases, where several corrections are available. The main reason for this is that, because the quality of the fit must be checked, these methods are usually highly interactive.

Currently, three different possibilities are offered within PIA:

- Drift recognition: the stabilized part of the measurement is identified, starting from the last measured signal
- The physical model developed by Fouks and Schubert mentioned in Section 2.2
- An empirical solution for far-IR detectors (Ge:Ga), based on exponential functions

Superimposed on the signal transients there is a long term drift effect that needs to be quantifed by the calibration: the responsivity of the detectors systematically changes with time due to hits by high energy particles. This will be addressed in some more detail in Sect. 3.2.9.

In most cases, fortunately, ways around have been found to deal with ISOPHOT transients and with the above mentioned need of a high interactivity, and clever methods have been developed and implemented in the automated pipeline which can correct the transient effects to a large extent in a blind way.

In the following we will present a summary of the efforts developed during the last years to correct ISOPHOT data for transient effects as well as a few examples showing the results obtained. Depending on the AOT and observing mode, different transient correction methods are recommended. Finally, the current implementation status of each of these methods is summarized, with indications about whether they are available in PIA and/or in the pipeline.

3.2.1 Transient effects in staring PHT-P and PHT-C observations: Drift recognition

The first indication of transient effects is any increase or decrease of the signal observed in some measurements. However, transient effects can have such long time scales that no apparent trend is seen during the observation. An automatic procedure to recognize the stable part in the data was introduced in PIA. It is based on a trend analysis of the signal values. It discards signals from the beginning of the measurement until a stable region is found, or, alternatively, a minimum number of data points are left (typically 7 signals or the last 8 s). The result of this analysis is an assessment whether a measurement is stable, partially stable or unstable. Depending on the result a certain part of the data is selected to derive the final value. Currently, this procedure is used in the derivation of signals in the automatic pipeline processing of staring PHT-P and PHT-C measurements improving significantly the quality of the photometry.

A detailed description of how the drift recognition algorithm has been implemented in the pipeline can be found in Section 7.3.5 of the ISOPHOT Handbook (Laureijs et al. 2000). This is based on the non-parametric Mann statistical test (Hartung 1991).

3.2.2 Applicability of Fouks-Schubert method to PHT-S and PHT-P observations

Schubert et al. (1995) showed, using data obtained during the ISOPHOT pre-flight calibration tests, that the non-linear transient response of the detector array SS/SL (Si-based) could be described by a simple analytical function. This function was derived based on the physical model developed by Fouks and Schubert (1995). The parameters E and β were determined finding very long stabilization times for low fluxes (~20 min at a flux of 1 Jy). Typical values for β and E were 0.6 and 2.5, respectively. In particular, the first 15 pixels in the SS (2.5-3 μm) array showed very slow responses compared to the rest.

However, even although (1) a good agreement was achieved between transients and Fouks model during ground based tests and (2) transient shapes did not change significantly during flight, use of the Fouks-Schubert model on in-flight data was unsuccessful.

Staring observations cannot be well reproduced using the Fouks-Schubert model because this model predicts always a monotonic behaviour of the response, while we find very often peculiar drift curves with a characteristic hook shape, especially at short wavelength pixels. The differences found with respect to the ground calibration can be likely attributed to the different operational conditions.

Several facts could explain the change of behaviour: detectors in space were switched-on prior to any observation and switched-off afterwards, opposite to the more continuous ground calibration; high energy radiation particle hits may also affect the transient behaviour.

With respect to this, it is possible that high energetic particles which hit the detector generated electron-hole pairs resulting in visible glitches and in accumulation of invisible positive (hole) and negative (electron) charges captured in the bulk. These charges can modify the parameters and operation of the detector (Schubert et al. 1994). The used electrical curing could not completely restore the parameters and the detector operation.

Note that CAM-LW had a different design (Agnése et al. 1989, Cesarsky et al. 1994): the upper side was set to ~25 V, the lower side, connected through indium bumps to CRE, was the reference (0 V) and the reflecting plane added around the contacts at lower side was set to ~5 V. Undesirable charges in the detector were, in this case, likely evacuated through this channel. Furthermore, in order to avoid changes of the parameters, the CAM-LW detector was never electrically switched off (ISOCAM Handbook - Siebenmorgen et al. 2000)

Therefore, for staring modes, a different approach was undertaken in order to be able to calibrate the data without having to do a prediction of the stabilized photocurrent. This is the so-called 'dynamic calibration' method which will be described in the following Section.

On the other hand, chopped measurements for which the flux history is well known, could be well modelled using a combination of both the signal jump and the temporal behaviour for a fixed flux level (see Figure 3.3). The pre-flight values of the parameters β and E were checked using special observations, finding a very good agreement. The implementation of this correction is available in PIA versions later than 6.4.

In principle, detectors P1 and P2 could be treated in a similar way as SS/SL, since they are manufactured of similar material. However, in this case the detector specific constants of P1 and P2 filters have not been fully determined and, again, the Fouks-Schubert model cannot be used since it cannot reproduce the often appearing hook responses in the signals of these detectors.

3.2.3 Transient corrections in PHT-S chopped measurements

Chopped observations with PHT-S were extensively performed on mostly faint sources. This means that the response of PHT-S detectors after each flux step is very slow when exposed to low illumination levels. Due to these slow detector transients, an important fraction (theoretically up to 40%) of the difference signal between the chopper on-source and off-source signals is lost. This causes a large uncertainty in the photometric calibration when no corrections are made and assuming a fixed responsivity for the PHT-S detectors.

A method to correct for this signal loss is by applying the Fouk-Schubert method above mentioned, which we know it is based on a physical detector model. However, this procedure works

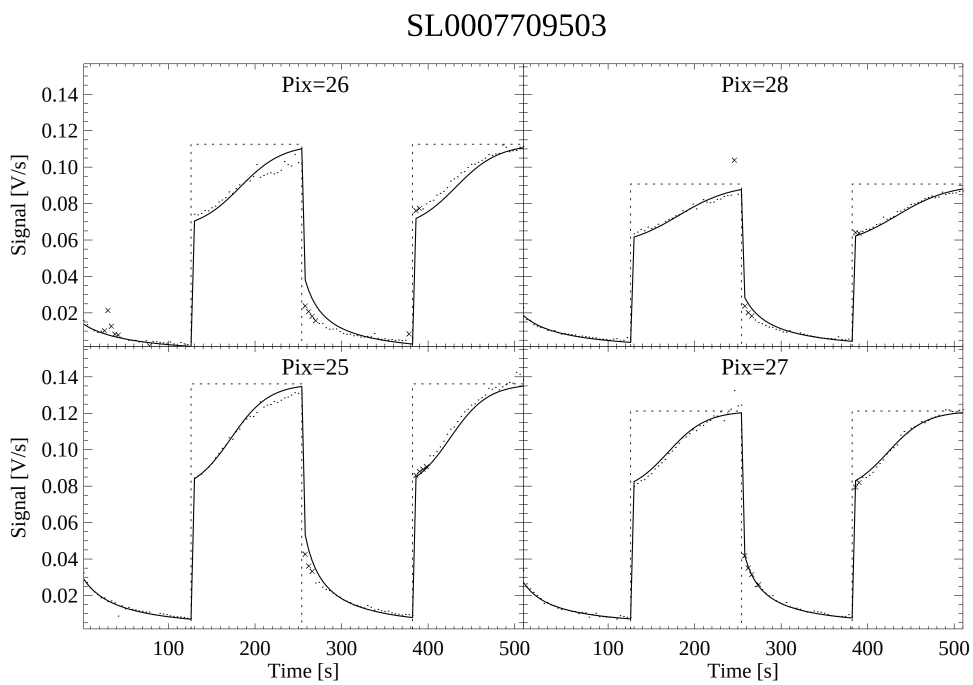

Figure 3.3: *Example of a chopped measurement (alternating between off and on-source observation) for several pixels of detector SS. The Fouks-Schubert model fitted to the data (dotted line) is represented by the solid line. The dashed boxes represent the predicted final signal.*

properly for the true signal flux range, only where the flux step is not so high that hook effects appear. In addition, a relatively high signal-to-noise ratio and sufficiently long chopper plateaux are required for the fitting procedure. Unfortunately, in most chopped observations the signal-to-noise ratio is low: often the source is only barely detected upon a low background level.

Thus, although the possibility exists in PIA (see Section 3.4) of applying the Fouks-Schubert correction to faint sources observed with PHT-S in chopped mode and enough signal-to-noise, an alternative approach was used to calibrate these observations in the automated pipeline.

The method is based on a direct comparison between the difference signal of the source and the difference signal of a calibration standard with similar brightness. It does not require any model fitting, which introduces less systematic uncertainties from model assumptions in the calibration process.

With this purpose, a number of faint calibration stars with $m_K = 1.65$ to $m_K = 7.54$ were measured. Note that there is a clear bias on the shape of the spectral energy distribution of the standards: the stellar spectra are always fainter at the longer wavelengths. The calibration measurements are listed in Table 3.2.

Data reduction

The data reduction of calibration measurements was done using PIA version 7 routines with the following processing steps:

- ERD corrections: Two thresholds deglitching.
- ERD → SRD: Ramps were split into 3 and 5 pieces for those measurements with t_{reset} = 16 s and 32 s, respectively.
- SRD corrections: deglitching
- SRD → SCP: Signal difference is computed separately from medians of all values corresponding to *on* and *off*-source chopper positions. The final result is the signal difference *on-off* per pixel.

Table 3.2: *List of calibration observations used in the calibration of PHT-S chopped observations*

Star Name	m_K	Sp.Type	TDT#	Chopp.Mode	t_{res}[s]	t_{chop}[s]	t_{exp}[s]
HR6464	1.65	M0III	SL0163601102	Tria	4	16	1024
HR5986	2.73	F8IV-V	SL0166400502	Tria	8	32	1024
HR6817	3.77	K1III	SL0167800801	Rect	16	64	1024
HR6817	3.77	K1III	SL0167800902	Tria	16	64	1024
HR6847	4.79	G2V	SL0169300401	Rect	32	128	2048
HR6847	4.79	G2V	SL0169300502	Tria	32	128	2048
HD132142	5.79	K1V	SL0163600901	Rect	32	128	2048
HD132142	5.79	K1V	SL0163601002	Tria	32	128	2048
HD172323	6.59	F9V	SL0168501601	Rect	32	128	2048
HD184400	7.54	F5	SL0184604401	Rect	32	128	4096

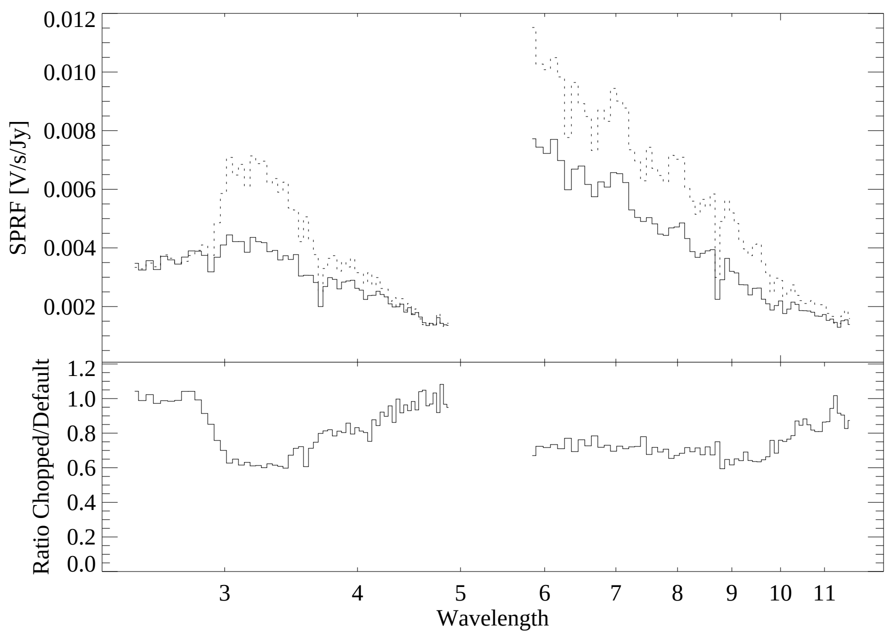

Figure 3.4: *Comparison of spectral response functions as derived from staring (dotted line) and chopped observations (solid line).*

Spectral response function

A spectral response function (hereafter SPRF) is determined from the ratio between the signal difference (*on* $\rightarrow$ *off*) and the model flux for each calibration star. The model fluxes are taken from M. Cohen and P. Hammersley inputs. A mean value for the SPRF is then derived using inputs from all calibration standard measurements. A comparison between the SPRF derived this way and the SPRF obtained from staring calibration observations shows differences up to 30-40% in the regions 3-3.5 μm and 5.9-10 μm (see Figure 3.4).

The individual SPRFs, however, vary systematically with the brightness of the calibration stars. The variation can be as large as 20% for certain pixels, especially those in the middle of the two arrays (SS/SL). For this reason we decided to introduce a first order correction to the mean SPRF which is only a function of the difference signal. This correction is based on the fact that the difference signal corresponds to first approximation to the brightness of the source plus background. The background in the ISOPHOT-S wavelength range is dominated by the Zodiacal Light which is detectable only at the longest wavelengths. The brightness level of the background is so low that the time constant of the transient of the background signal is much longer than the integration time per plateau.

The ratio between the SPRFs derived from each individual measurement and the average SPRF was computed. We looked for a linear correlation between these ratios and the signal difference between on and off positions (in log scale), as described in the following expression:

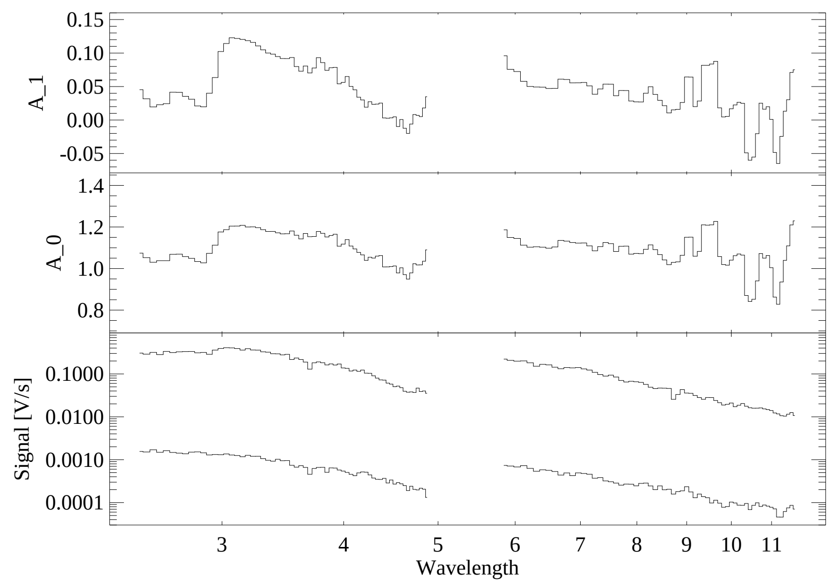

Figure 3.5: *The first order correction to the mean chopped SPRF for all ISOPHOT-S pixels. The coefficients A_0 and A_1 (see text) are plotted in the middle and top panels, respectively. We also plot the validity range of signals from where the correction was derived in the bottom panel*

$$f^j_{corr} = A^j_0 + A^j_1 \; log(S^j_{on} - S^j_{off}); \quad SPRF^j_c =< SPRF >^j_{mean} f^j_{corr}; \;\; j = 1, 128 \qquad (3.1)$$

To improve the fit any point deviating by more than 5σ was rejected. The derived coefficients are plotted in Figure 3.5.

As a self-consistency check all calibration star measurements were calibrated using the two approaches described above and compared to the theoretical models. The results obtained are presented in Figure 3.6. It can be seen that the spectra calibrated with the mean SPRF are within 20% of the prediction. Addition of the first order corrections improves the consistency to better than 10%. The faintest star HD 184400 is an exception, which can be attributed to a non-detection of the stellar flux towards the end of the long wavelength part of the array.

3.2.4 Dynamic calibration of PHT-S staring measurements

Introduction

Because of the problems encountered applying the Fouks-Schubert correction to PHT-S and P1 data, an alternative approach was suggested by Linda Cornwall (RAL) and worked out by Garzón and Hammersley (both IAC) in 1997. The method, known as *dynamic calibration*,

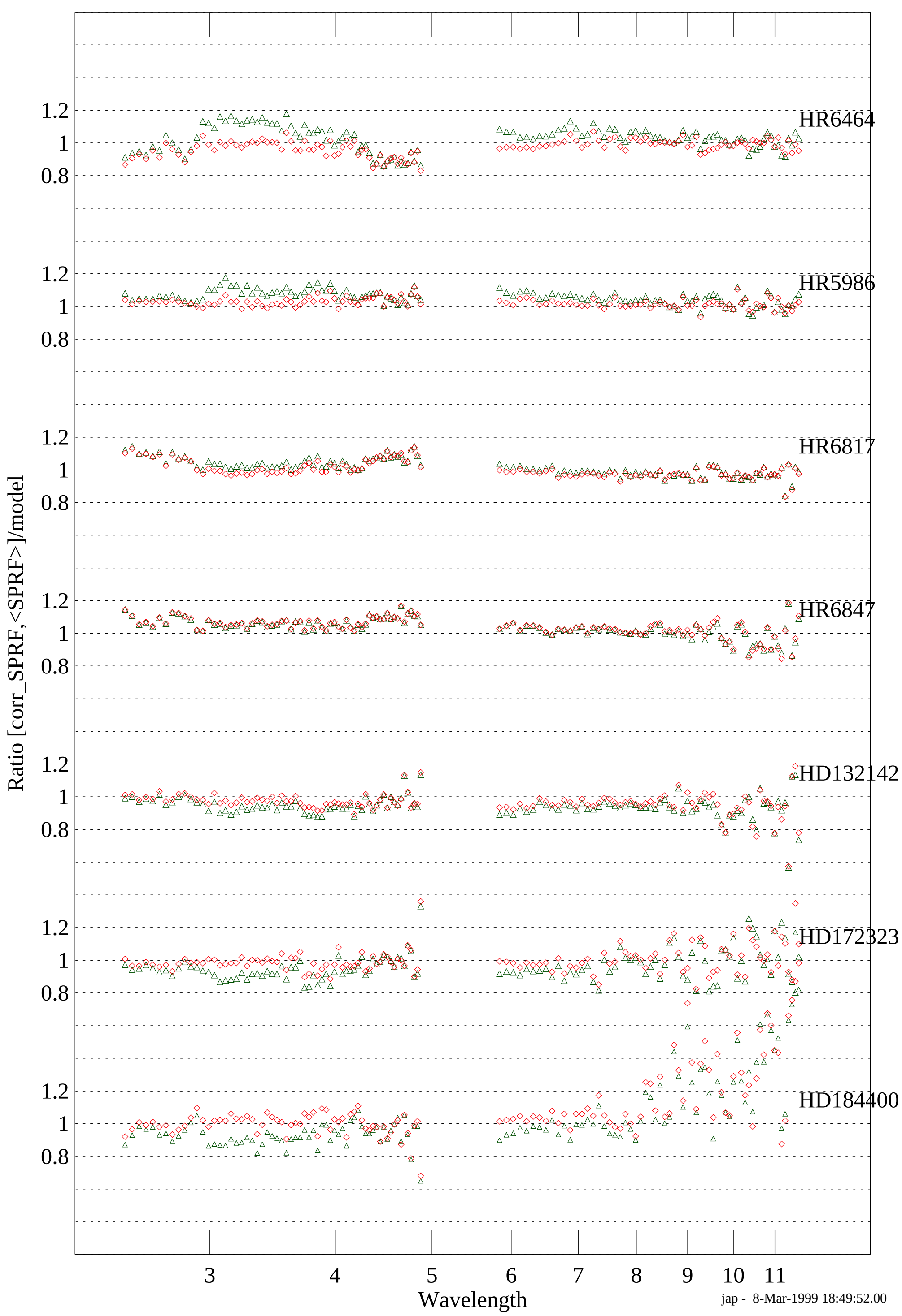

Figure 3.6: *Ratio between the calibration standars spectra and the models. The SPRF derived as explained in the text is used to calibrate the measurements in two ways: using the mean SPRF (triangles) and including the first order correction (diamonds).*

proposed to the PIA development team, is based on the following assumptions: (1) the temporal response of an individual pixel depends primarily on the illumination level and (2) for a given illumination level, the temporal response is reproducible as long as the flux history is similar.

The requirement of a similar flux history is to a large extent fulfilled in ISOPHOT-S observations obtained with the AOT PHT40 in staring mode (this is not the case of PHT-P1 observations or PHT-S observations in chopping mode for which this dynamic calibration method is not applicable).

PHT-S staring observations always yield the same flux pattern: the observation starts first with a 32 s dark measurement which is followed by the sky measurement. Thus, an ISOPHOT-S staring observation can be dinamically calibrated by comparing the time evolution of the sky signals with that of a calibration star of similar signal level and measurement time. The flux of an ISOPHOT-S pixel is given by the flux of the calibration star for that pixel multiplied by the signal ratio between target and calibration star. The selection of the calibration star is done independently for each pixel. Tests have shown that the drift behaviour of a given pixel remains similar within a flux range of a factor ~ 1.6 (0.5 magnitudes), although the behaviour changes faster for high fluxes.

The method, as implemented in PIA v7.3 by J. Acosta-Pulido (ESA/IAC), applied to PHT-S staring measurements brings down the errors associated to this observing mode (sometimes as high as 30%) to just a few percent.

Calibration measurements

The main idea behind the dynamic spectral response calibration is that a standard star spectrum of similar brightness as the target spectrum suffers the same transient effects. By taking into account the same temporal evolution of the signals for both standard and target spectrum, the transient effects cancel out by dividing the target spectrum by the standard spectrum, without having to derive "infinite values" with a sophisticated transient correction. Since target and standar spectrum can be quite different in shape, a library of standard stars covering a wide range in flux level is necessary to calibrate each PHT-S pixel individually in this way. Thus, series of measurements were performed on calibration stars, covering a range of magnitudes from $m_K = -3.08$ to $m_K = 7.54$. The full list of calibration stars is given in Table 3.3. The model spectra are presented in Figures 3.7 and 3.8.

Dependence on detector temperature

Additional measurements were perfomed on calibration stars using the AOT PHT40, during the Perfomance Verification (PV) Phase of ISO. Unfortunately, these measurements cannot be included in the dynamic calibration database because the drift behaviour was different than those of similar fluxes (see Figure 3.9). The reason was found to be the different temperature at which ISOPHOT-S detectors operate during that special period (T ≤ 2.6 K) and the routine phase (T $\simeq 2.9 \pm 0.1$ K).

Special cases: faint sources

The exposure time becomes naturally long at low illumination levels in order to get sufficient signal to noise ratio. Moreover, the response of the detector is extremely slow in those cases. Some observers have perfomed measurements of very faint targets, and their exposure time is longer than the calibration measurements. In order to extend the drift behaviour to the longest measurements obtained by ISOPHOT-S some of these measurements were included in the database (listed in Table 3.4). The measurements which correspond to similar flux levels were co-added at the signal level, producing average drift curves. This way the time evolution

Table 3.3: *Log of calibration measurements. All observations were performed in staring mode. Notes: 1: Model computed by M. Cohen; 2: Model computed by P. Hammersley; 3: Inconsistency with contiguous stars (included in the database, but discarded by default; 4: Affected by strong memory effects from a precedent observation of a bright source (not included in the database); 5: Too short exposure for such faint source (not included in the database).*

Source Name	m_K	Sp.Type	TDT#	t_{expo}	Comments
HR5340-off			59401301	128	
HR5340	-3.08	K2III	59401302	256	1
HR8775-off			73600901	128	
HR8775	-2.33	M2II	73600902	256	1
HR337-off			59403801	128	
HR337	-1.94	M0III	59403802	256	1, 3
HR2491-off			70705408	256	
HR2491	-1.39	A1V	70705409	256	1
HR1231-off			61502501	128	
HR1231	-0.96	M1IIIb	61502502	256	1
HR1654-off			64302701	256	
HR1654	-0.18	K5III	64302802	256	1
HR7001-off			50301801	256	
HR7001	0.00	A0V	50301802	256	1
HR7980-off			73401401	256	
HR7980	0.22	K5IIIa	73401402	256	1
HR6132-off			60100601	128	
HR6132	0.62	G8III	60100602	256	2
HR7310-off			69300601	128	
HR7310	0.74	G9III	69300602	256	1
HR7924-off			72001001	256	
HR7924	0.85	A2Ia	72001002	256	2, 3
HR6688-off			39800401	256	
HR6688	1.02	K2III	39800402	256	1
HR6464-off			67101001	256	
HR6464	1.65	M0III	67101002	256	1
HR7742-off			56601901	128	
HR7742	2.29	K5III	56601902	256	1
HR5986-off			52401701	256	
HR5986	2.73	F8IV-V	52401702	256	2
HR7469-off			72000901	512	
HR7469	3.52	F4V	72000902	512	2
HR7341-off			53102201	256	
HR7341	3.72	K1III	53102202	256	2
HR6817-off			74801401	512	
HR6817	3.77	K1III	74801402	512	2
HR6847-off			39102301	512	
HR6847	4.79	G2V	39102302	512	1
HR5886-off			69300101	512	
HR5886	5.09	A2IV	69300102	512	2
SAO 83309-off			60801101	512	
SAO 83309	5.44	K5V	60801102	512	2
HR8487-off			76202601	1024	
HR8487	5.51	A0III	76202602	1024	2
HD211476-off			76202501	1024	
HD211476	5.55	G2V	76202502	1024	2
HD132142-off			60100701	512	
HD132142	5.79	K1V	60100702	512	2, 4
HD158485-off			51704201	256	
HD158485	6.14	A4V	51704202	256	2, 5
HD172323-off			40601001	512	
HD172323	6.59	F9V	40601002	512	2
HD184400-off			74101801	1024	
HD184400	7.54	F5	74101802	1024	2

Table 3.4: *Special measurements included in the dynamic calibration database. Notes: 1: Only the SL array; 2: Uncertain calibration (it is discarded by default in the database).*

Spectrum ID	Observer/Proposal	TDT#	t_{expo} (s)	Notes
Ave star_1	RWEHRSE/MD STRAT	34402204	2048	
Ave star_1	RWEHRSE/MD STRAT	36001403	2048	
Ave star_2	TTSUJI/PROP 004	38202009	4096	
Ave star_2	TTSUJI/PROP 004	38700709	4096	
Ave star_2	TTSUJI/PROP 004	40501903	4096	
Ave star_2	TTSUJI/PROP 004	40900101	4096	
ZLbackground		20 meas.	4096	1, 2

for each pixel is preserved and the signal to noise ratio improved. Then we have flux calibrated the average spectra using the dynamic method here described and the best matching standard calibrators from Table 3.3.

Data processing

All calibration data were acquired using AOT P40. The data were processed up to SRD level using mostly standard PIA procedures, details follow:

- ERD corrections: Two thresholds deglitching.
- ERD → SRD: linear ramp fitting
- SRD corrections:

  - Signal deglitching with min-max sigma clipping and restoration of affected data points.

  - Subtraction of orbital dependent dark current

Signal temporal evolution

The time evolution of the signals for all pixels and all calibration measurements is fitted with Chebyshev polynomials of different degrees (the Fortran program is listed in Appendix E, it uses the routine E02ADF from the NAG library). Chebyshev polynomials are a good aproximation to the minimum degree polynomial which deviates less from a given function. The minimum number of terms to be used from the Chebyshev expansion is determined accordingly to the following criterium: the RMS of the deviation between the polynomial expansion and the measured signals should be less or equal to the data noise. The noise is determined from the scattering of the differences between consecutive signals to avoid as much as possible the scattering due to the transient effect. An ASCII text file was produced for each calibration measurement, which contains a row per pixel. A record in this file contains the following information:

- Measurement name according to PIA convention
- Pixel number
- Sig_{ref}[16,32,64,128,256] - The calibrator signals at 16, 32, ..., 256 s
- t_{ini}; t_{end} - The limits of the Chebyshev expansion

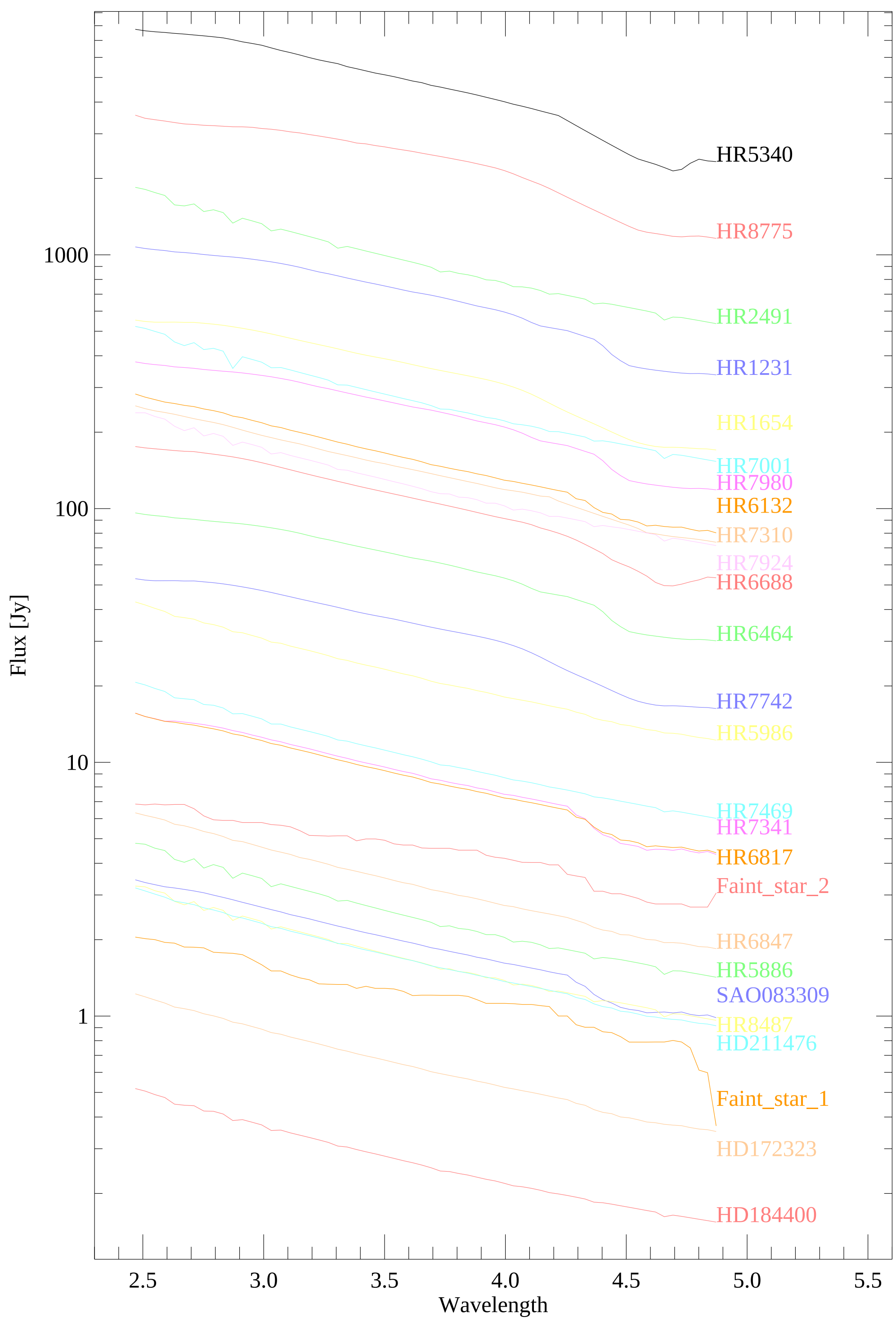

Figure 3.7: *Model spectra for all calibration stars. Only the short wavelength part is shown.*

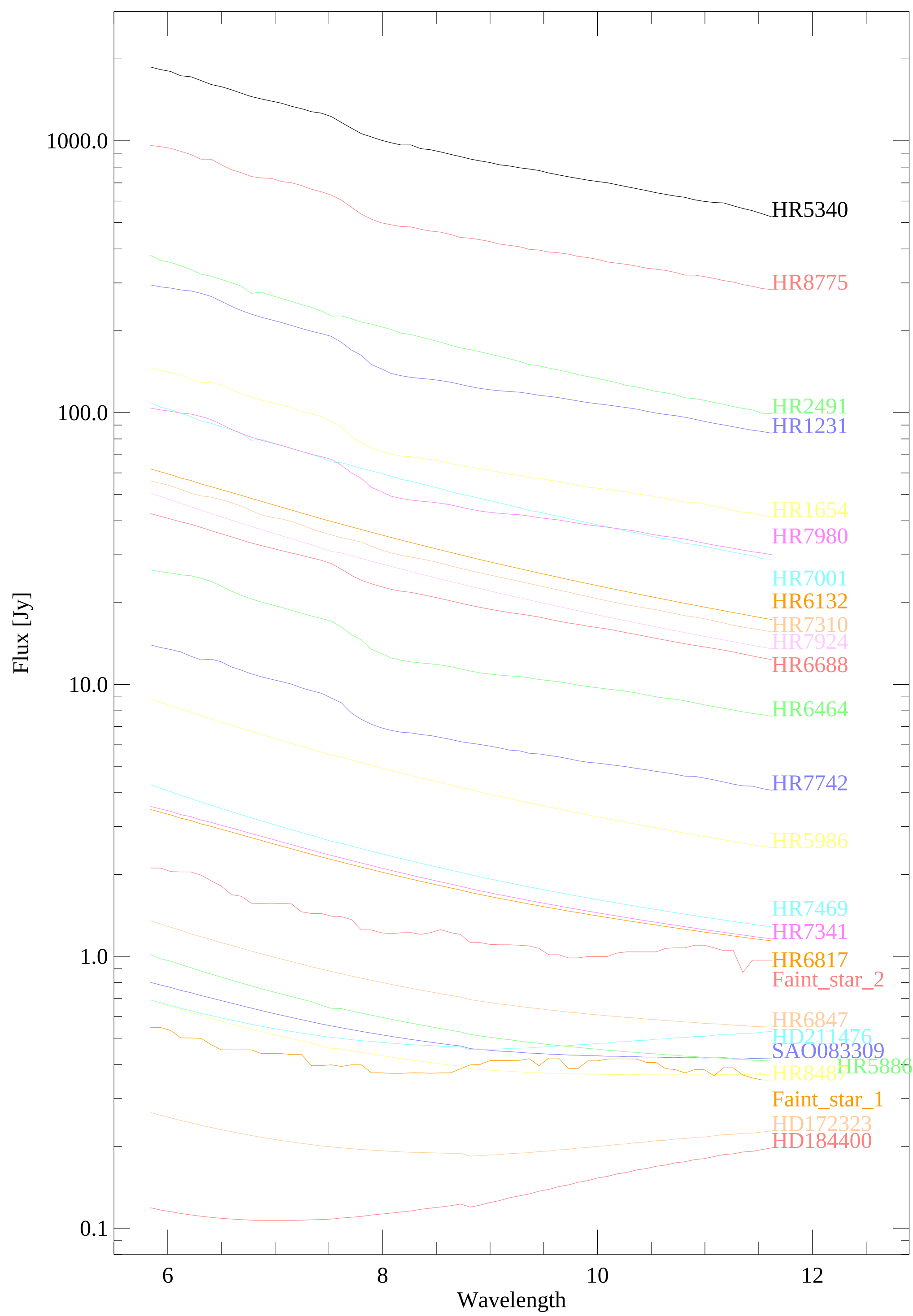

Figure 3.8: *Same as Fig. 3.7, but showing the long wavelength part of the PHT-S spectra.*

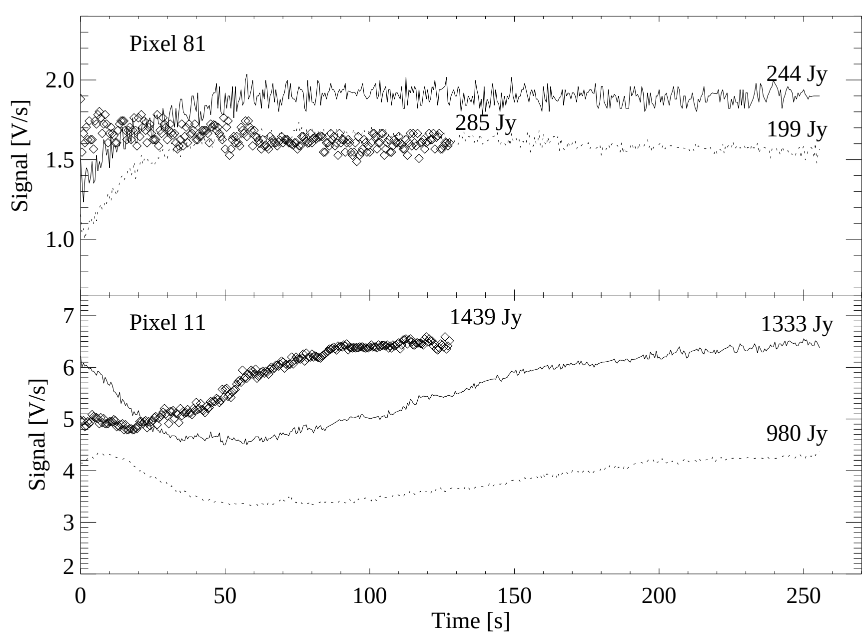

Figure 3.9: *Dependency of the drift behaviour with temperature. We present here the time evolution of the signal for three different flux levels and for two pixels (pixels 11 and 81 for the short and long wavelength arrays, respectively). Diamonds represent a measurement where the detector temperature was $\sim$ 2.55 K, whereas the solid and dotted lines represent two measurements at $\sim$ 3.01 K.*

- N_{terms} - The number of terms in the Chebyshev expansion
- $Coefs_{Cheby}$ - Chebyshev polynomial coeffiecients

The values of Sig_{ref} are used to construct a look-up table, which is used to quickly select the best calibrators matching to a given target and for each pixel.

Flux assignment

We assume that the time evolution of the response for a given pixel is mainly determined by the illumination level. The signals of each calibration star are taken before background subtraction, but after dark current subtraction. The dark current is regarded here as an offset which does not influence the response of the detector. Therefore the total flux (source plus background) has to be modelled for each calibration source. The stellar models provided by M. Cohen and P. Hammersley were used for the flux of the calibration stars. The background could be estimated from the dedicated measurements (an offset position was measured for each calibration star), however in most cases they cannot be used for several reasons: the S/N ratio is very poor in the long wavelength part and the background is not detected at the short wavelength array, moreover the drift behaviour of the background measurement may change with respect to that of the on-source due to the different illumination. Instead, we used a Zodiacal Light model to determine the celestial background. At the wavelength range of ISOPHOT-S the background is dominated by the Zodiacal Light, which we have modelled by the composition of an emission component (a blackbody of T=267 K) plus a reflection one (a blackbody of T=6000 K). The scaling of the composite model is done by least square fit to COBE/DIRBE weekly averaged measurements at bands 2.2, 3.5 4.9 and 12 μm.

The background model is computed in surface brightness units which has to be converted to the equivalent flux for point sources. Therefore a factor converting the surface brightness values (in MJy/sr) into point source units (in Jy/beam for a given pixel) has to be applied. These factors were computed by integrating the measured beam profile up to distances of 60" from the aperture center.

The flux calibration for a given target is done in this method by scaling the ratio between the signal time sequences from the target and the calibrator with the calibrator modelled flux (source + background).

3.2.5 Empirical solution for ISOPHOT far-IR detectors P3 and PHT-C: staring observations

The basic transient behaviour of detectors P3, C100 and C200 (all based on Ge:Ga) after a flux change can be described as follows:

1.- There is an initial jump of constant relative height with respect to the final signal difference. This has also been observed in chopped measurements where the flux modulation is fast. There is theoretical support for this feature coming from numerical computations (Fig. 5 in Haegel et al. 1996).

2.- A short term ($\leq$10 s) response follows, which shows a characteristic "hook response" (see Figs. 3.10 and 3.11). This part looks different for the individual detectors: for P3 and C100 it appears like overshooting in case of flux increase and undershooting in case of flux decreases, whereas for C200 it is in general a very fast overshooting.

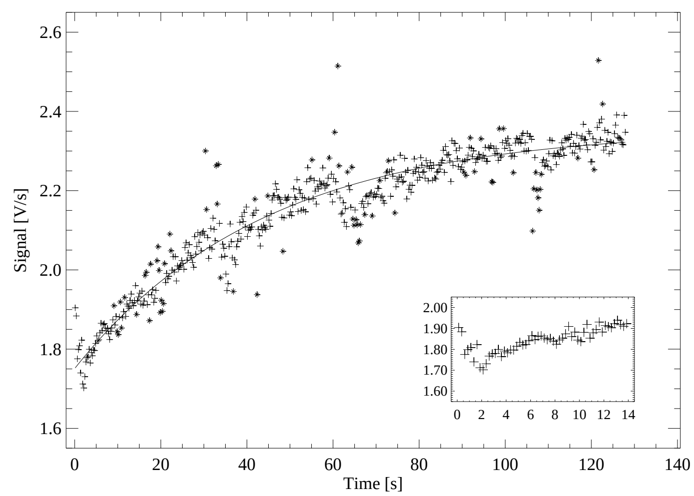

Figure 3.10: *Typical transient behaviour of detector P3 at intermediate flux level (∼11 Jy at 100μm). The measured signals are represented by plus sign symbols. Detected glitches are marked by crosses. The exponential model is represented by the continuous line through the data points. The initial signal sequence is shown in the inset, where the hook response is clearly recognized.*

3.- A long term response follows, which can be well modelled by an exponential function in most cases (see Figs. 3.10 to 3.13).

4.- The long term response exhibits a time constant which decreases for high fluxes, whereas it increases dramatically for low fluxes.

Based on these observational properties above mentioned a solution based on a single exponential function was proposed, which can be written as the following expression:

$$S(t) = S_{\infty} + (S_{ini} - S_{\infty})exp(-t/\tau); \tau = \frac{E}{S_{\infty}^{\alpha}} \tag{3.2}$$

The first analysis shows that τ is inversely proportional to the final signal, S_{∞}, in log-log scale (see Fig. 3.14). Therefore τ can be written as an inverse power law function of S_{∞}. The parameter α describes the behaviour of the transient effects with the illumination and E is a normalization constant. E and α are parameters which have to be determined for each detector/pixel. In the case of the Fouks-Schubert function α is equal to unity. If the proposed function is a good description of the transient behaviour of the considered detectors, those parameters can be fixed. The stabilized signal is obtained by fitting the above function to the measured signals and leaving S_{ini} and S_{∞} as free fit parameters.

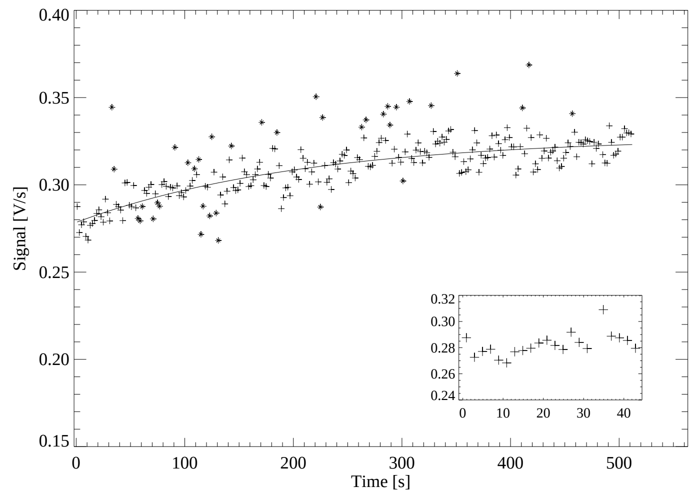

Figure 3.11: *Typical transient behaviour of detector P3 at low flux level (∼2 Jy at 100μm). The meaning of the symbols is as in Fig. 3.10*

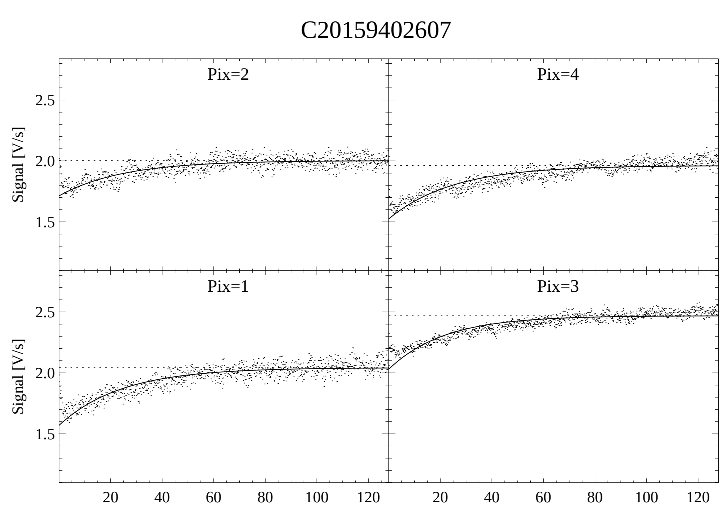

Figure 3.12: *Typical transient behaviour of the four C200 pixels at high flux level (∼60 Jy at 150μm). The dots represent the measured signals, the solid line the fit and the dashed horizontal line the predicted final signal level.*

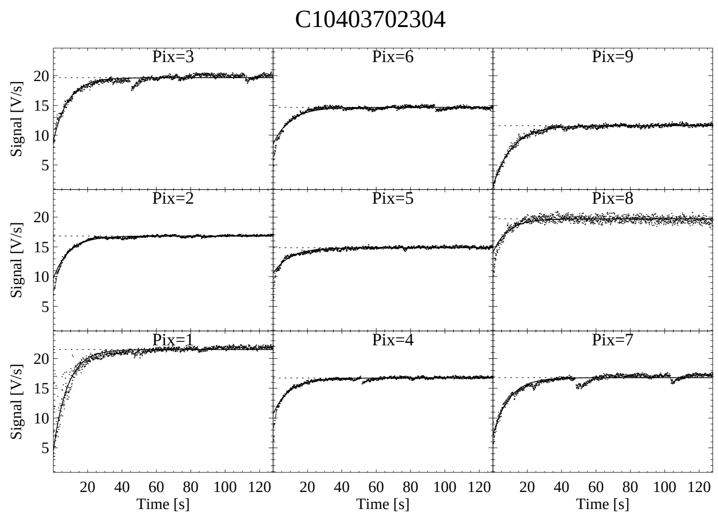

Figure 3.13: *Typical transient behaviour of the nine C100 pixels at high flux level (∼75 Jy at 80μm). The meaning of the symbols is as in Fig. 3.12*

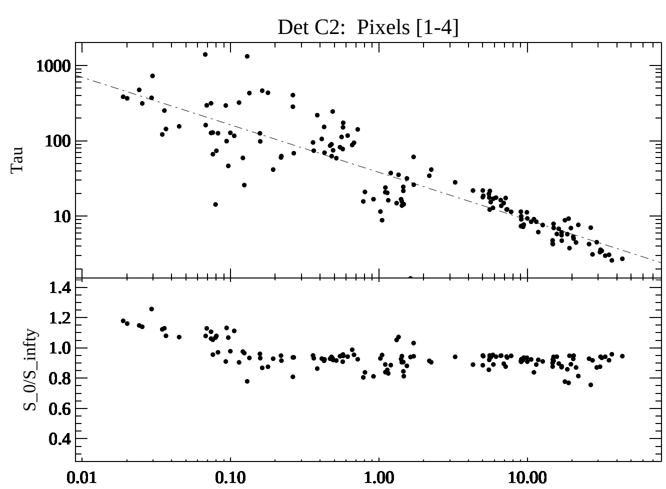

Figure 3.14: *Time constant determination for detector C200 (including all pixels). The ratio of initial to final signal obtained from the model fit is presented in the bottom panel.*

Determination of time constants

The parameters E and α for the detectors P3, C100 and C200 were determined in-orbit using a large set of long measurements. The measurements were selected if a clear transient behaviour was present, and they were long enough that at the end the photocurrent is close to stabilization. Nevertheless, our data set may suffer some selection bias: transient behaviour with very long time constants ($>$ 1000 s) will not be detected because of the limited observing time; the flux history may influence the transient as well as the switch-on of the detector every time an observation starts. In the process of determining E and α each measurement was fitted by leaving all parameters free in the above expression and rejecting those fits where the residual RMS per degree of freedom was larger than 3.

We present in Fig. 3.14 an example of the best fitting parameters. Clear correlations between τ and S_∞ can be established. From a least square fit we determined the values of E and α and the results are presented in Table 3.5, together with the correlation coefficient r. It was found that for P3 and C200 the correlation is very good and is worse for C100.

We perfomed tests using an independent set of measurements other than those used for determining the time constants. The resulting χ^2 distributions are very narrow and peak around 1. The worst case is the detector C100, for which the χ^2 distribution for all pixels (except pixel 8) is wide and values around 2-3 are frequent. The low frequency noise which affects detectors C100 and P3 when measuring faint targets is likely limiting the goodness of the fit.

We present in Fig. 3.15 an example of the application of the model for a measurement with detector C100: using the full measurement time of 512 s an error of 6% between the direct measurement of the signal and the model prediction is found. A comparison of the estimates of the final signal using only the first 32 s gives the following results: the value obtained from the drift recognition (Section 3.2.1) is too low by 30%, whereas the value obtained from the empirical model is lower by only 12%. This example demonstrates that the use of the drift modelling significantly improves the photometric accuracy of relatively short measurements.

We can also estimate, according to the values derived and shown in Table 3.5 the fraction of the final signal which is affected by the slow transient component, i.e. the signal difference between the value reached at the initial jump and the final value. The magnitude of this component combined with the time constant determines the accuracy of any measurement after a certain time. For example, a long time constant is not so relevant, if the fraction of the slow component is small compared to the total signal. The magnitude of the slow component can be estimated from the initial jump after a flux change and the knowledge of the final stable current. This has to be derived from chopped measurements where the flux changes are like a step-function. Raster observations cannot be used, because the flux varies gradually as the telescope slews to a different sky position. Results for detectors P3, C100 and C200 are presented in Table 3.5, where β represents the fraction of the total signal difference which is achieved immediately after the flux change. It has been found theoretically that the magnitude of the slow component increases with the photoconductive gain, G (Haegel et al. 1996). G depends on the material, the electric field and the dimensions of the detector. Detectors P3 and C100 are manufactured

Table 3.5: *Time constants for the empirical model*

Detector	E	α	r	β
P3	87±8	0.79±0.05	−0.79	∼0.34
C100	36±3	0.48±0.04	−0.63	∼0.30
C200	38±2	0.63±0.03	−0.89	∼0.85

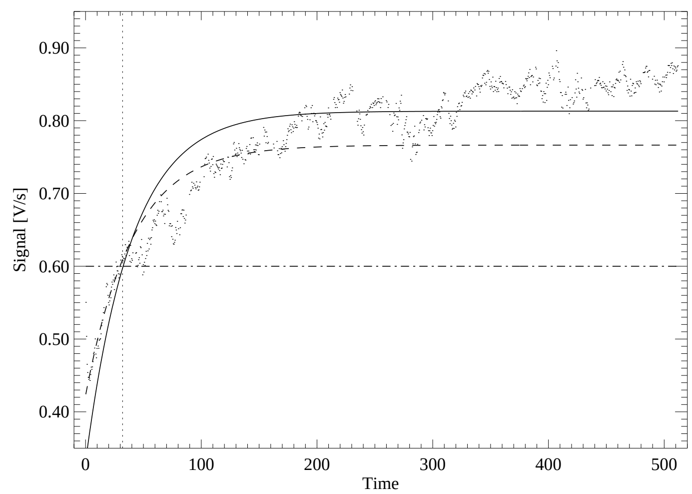

Figure 3.15: *Measurement of an intermediate brightness (∼ 8 Jy at 100 μm) source using detector C100 (central pixel). The measured signals are shown by dots. The solid line represents the empirical model described in the text using data up to 512 s. The final signal was also predicted using only the first 32 s (marked by the vertical dotted line) in two ways: by the drift recognition method (Section 3.2.1), shown as the dashed dotted line and by the exponential model (Section 3.2.4), shown as the dashed line.*

of the same material but they have different bias voltages and dimensions, yielding $G[C100] > G[P3]$; which is consistent with a larger fraction of the slow component for C100.

3.2.6 Transient effects in chopped PHT-P and PHT-C observations

In the case of chopped PHT-P and PHT-C observations, non-stabilized signals cause significant losses on the true difference signal. The present signal derivation in OLP relies on the analysis of signals from pairs of consecutive readouts rather than signals per ramp. This gives better statistics of the signals per chopper plateau, since in many chopped measurements each chopper plateau covers only a few (typically 4) ramps. To increase further the robustness in determining the difference signal, the repeated pattern of off-source and on-source chopper plateaux yields a *generic pattern* in a chopped measurement which consists of only 1 off- and 1 on-source plateau. The generic pattern is generated using an outlier resistant averaging. The shape of the generic pattern determines the correction factors with regard to stabilized staring measurements and depends on the transient behaviour of a given detector - for example, in case of detector P3 the signal difference is determined from the maximum of the on-signals and the minimun of the off-signals of the pattern, and in case of P1 and P2 the median signals of the on- and off-plateaux are used.

This analysis of chopped measurements applied to a sample of calibration standards yields an empirical signal correction function ζ which corrects a given (linearised) difference signal S_{src} :

$$S'_{src} = \zeta(S_{src}, det, t_{plat}) \quad [V/s], \tag{3.3}$$

where S'_{src} is signal corrected for losses due to the chopper modulation, det is the detector used, and t_{plat} is the chopper plateau time (in s). The dependency on det and t_{plat} is required to relate the chopper modulation frequency with the detector specific transient timescales.

Data processing

As a consequence of the problems above mentioned, the *conventional* processing method used for staring observations had to be changed drastically. Instead, a separate SPD level processing is used which makes use of these so-called *generic patterns*.

In this case, the chopped FCS measurements are treated in the same way as the chopped sky measurements, namely for both types of measurements a generic pattern is constructed.

Using a symmetry assumption, the corrected signal level of FCS1 is determined from the measured signal levels of FCS1 and FCS2 and applying the same signal loss correction as for the sky measurements. Following the signal and vignetting correction, DERIVE_SPD processing proceeds as for staring mode observations from reset interval correction to flux calibration, which uses the corrected FCS1 signal of the chopped FCS measurement.

After reading the ERD the following processing steps are performed for DERIVE_SPD:

1. ramp linearisation,
2. generic pattern creation,
3. reset interval correction,
4. dark signal subtraction,
5. signal linearisation,
6. determination of the difference signal $s_{s+b} - s_b$ from pattern,
7. determination of the difference signal corrected chopped signal losses,
8. flux calibration.

All these steps are explained in detail in Section 7.5 of the ISOPHOT Handbook (Laureijs et al. 2000)

3.2.7 Transient effects in PHT32 chopped raster maps

During the ISO mission, the ISOPHOT instrument collected more than 1100 observations in an oversampled mapping mode (AOT PHT32) in the wavelength range of 45 to 240 microns. The observations comprise mapping of small and large extended regions, but also faint point sources. In this case the mapping approach was adopted in order to minimize confusion noise.

PHT32 uses the chopper in the sawtooth mode to obtain the oversampled maps. Besides the signal losses induced by the chopping, detector transients of bright sources can introduce ghost images in neighbouring areas. This happens when a bright source was observed at the end of a sawtooth sweep. When the chopper mirror was directed back to the starting point of the sweep, the transient caused an increased signal which was recorded at the beginning of the next chopper sweep. The signal decays with the relevant time scale thereby mimicing a point source detection. Consequently, the ghost is always displaced from the bright source by 180" (=amplitude of the chopper sweep) in Y-direction.

PHT32 observations are at the time of writing this WG Final Report still not scientifically validated because of the strong signal transients due to flux changes generated by the relatively fast chopper movement which produced never-stabilized signals. The effect is a decrease in the source flux measured (up to a factor of 3, depending on the flux contrast between source and background), problems with the determination of PSFs for point vs extended sources and the presence of ghosts (90" away in the y-axis direction).

Although the transient behaviour observed cannot be modelled (over- and under-shooting effects are usually observed), an algorithm has been developed at MPI-Kernphysik (Heidelberg) by Richard Tuffs with the support of the ISO Data Centre at VILSPA which can correct the transients by by making use of the redundancy given in the PHT32 mode. The method applies an iterative drift correction assuming a 2 exponential drift curve, deriving the initial drift constants from calibration targets.

This program has recently been integrated in the ISOPHOT Interactive Analysis (PIA) so that most aspects of the processing can be addressed in a coherent and user friendly environment.

Although the algorithm, which is highly interactive and requires a considerable level of expertise from the user is still being tested, promising results have been obtained, some of which are shown in Section 3.3.

So far, and since the algorithm cannot be released with a large amount of initial support, hands-on workshops on PHT32 processing have been organized at VILSPA and IPAC in February/March 2001 to help those interested in data reduction of PHT32 data.

It is expected that the Workshops Proceedings will serve as a processing reference as well as a repository of (typical) science cases produced by the workshop attendants.

3.2.8 Transients in Ge:Ga PHT C-100 detectors: an empirical non-linear approach

A preliminary study (Sée 1999) has also been devoted to PHT C-100 transients. After testing different models (linear and non-linear, empirical or physical from Fouks' team (Fouks 1992), we can conclude that only an empirical non-linear model with a non-symmetrical behavior can simply reproduce the observations :

- downward incoming flux step results in an instantaneous decrease of $J_n(t)$ down to J_n^∞
- upward incoming flux step results, after an instantaneous jump β in an exponential increase of $J_n(t)$ up to J_n^∞.

Moreover, the memory effect from the block $n-1$ into the n-th one is taken into account (in an approximated form) and, as seen in the data, the memory effect is reseted when a downward step occurs.

Direct model then reads :

$$\text{for } t \in [t_n, t_{n+1}[\quad J_n(t) = \begin{cases} J_n^\infty & \text{if } J_n^\infty < J_{n-1}^\infty \\ J_n^\infty - (1-\beta)(J_n^\infty - J_{n-1}^\infty)\exp(-J_n^\infty(t-t_n)/\lambda) & \text{if } J_n^\infty > J_{n-1}^\infty \end{cases} \tag{3.4}$$

(with same notation than Eq. (2.1) which can be rewritten in a unique expression :

$$J_n(t) = J_n^\infty - (1-\beta)\varphi(J_n^\infty - J_{n-1}^\infty)\exp(-J_n^\infty(t-t_n)/\lambda), \quad t \in [t_n, t_{n+1}[\tag{3.5}$$

with $\varphi(u) = 0$ if $u \leq 0$ and $\varphi(u) = u$ if $u > 0$.

A block by block inversion method can then be used to correct for these transient effects in the above proposed framework. Two kinds of information are available :

1. the sought incoming flux is positive and

2. "by construction" a piecewise constant signal.

The idea developed here is to account for these informations in order to robustify inversion. This kind of *a priori* knowledge can be captured mathematically and exploited in a constrained framework shortly described above. Given the direct model of Eq. (3.5), the LS criterion (see Appendix B) reads :

$$Q_{\mathrm{LS}}(J^{\infty}) = \sum_{n=0}^{N-1}\sum_{p=0}^{P-1}\Big[J_n(p) - \Big(J_n^{\infty} - (1-\beta)\varphi(J_n^{\infty} - J_{n-1}^{\infty})\exp(-J_n^{\infty}(p-p_n)/\tilde{\lambda})\Big)\Big]^2 \tag{3.6}$$

with $\tilde{\lambda} = \lambda F_s$ (F_s is the sampling frequency). Index n runs over the block indices and p runs over the readouts indices. Due to the specificity of the memory effect, each term of the first sum only depends on two values of the stabilized values, so Q_{LS} can be rewritten :

$$Q_{\mathrm{LS}}(J^{\infty}) = \sum_{n=0}^{N-1} Q_n(J_n^{\infty}\ ,\ J_{n-1}^{\infty}). \tag{3.7}$$

As mentioned above, the property of the direct model does not allow us to ensure global minimization of (3.7) over $\mathbb{R}_+^N$. But, taking advantage of the specificity of the criterion, global minimization is possible over a finite subset of $\mathbb{R}_+^N$: an arbitrary fine regular grid of K possible values of the stabilized value : $G_J = \{J_{\max}k/K\}_{k=0,\ldots,K-1}$.
A dynamic programming algorithm has been implemented by F. Belleux within the PIA framework at IAS in order to achieve minimization over G_J. The idea is simple : compute the values of $Q_N(J_{N-1}^{\infty}, J_N^{\infty})$ for the K^2 possibles values of $J_{N-1}^{\infty}, J_N^{\infty}$. The minimizer with respect to J_N^{∞} is then available as a function of J_{N-1}^{∞}. The following steps consist in shifting indices by -1 and repeat the same operation with Q_{N-1}, Q_{N-2}, down to Q_0. The last step gives the minimizer with respect to J_{-1}^{∞}. Then a forward tracking step recursively gives the minimizer with respect to J_{-1}^{∞}, J_0^{∞}, … J_N^{∞}. The procedures clearly reach the true minimum of criterion (3.6), over the defined grid G_J. Optimum can the be refined using a gradient procedure, not described here.

Computation results : simulated data

The first step of the proposed computation study relies on simulated data according to model of Eq. (3.5). *True* stabilized value J_n^{∞}, simulated data $J_n(p)$ and estimated stabilized values $\hat{J}_n^{\infty}$ are shown in Fig. 3.16-(a). It can be clearly seen that the proposed method properly inverse the system and correct the transients : the reconstruction error between $\hat{J}_n^{\infty}$ and J_n^{∞} is less than 1%.

Computation results : real data

According to Fig. 3.16-(b), the proposed method seems to process real data as well as the simulated data shown in Fig. 3.16-(a). However, in Fig. 3.16-(b) we can see how the presence of glitches tends to slightly overestimate the stabilized value, as expected form a quadratic criterion in presence of positive *impulsive* noise. In the proposed framework, future work is still needed on glitch modelization by means of Poissonian noise.

3.2.9 Detector responsitivity drifts

Besides the signal transients induced by illumination changes, there is a long term drift effect, which appears even under constant illumination and with the detector signal adjusted to that level.

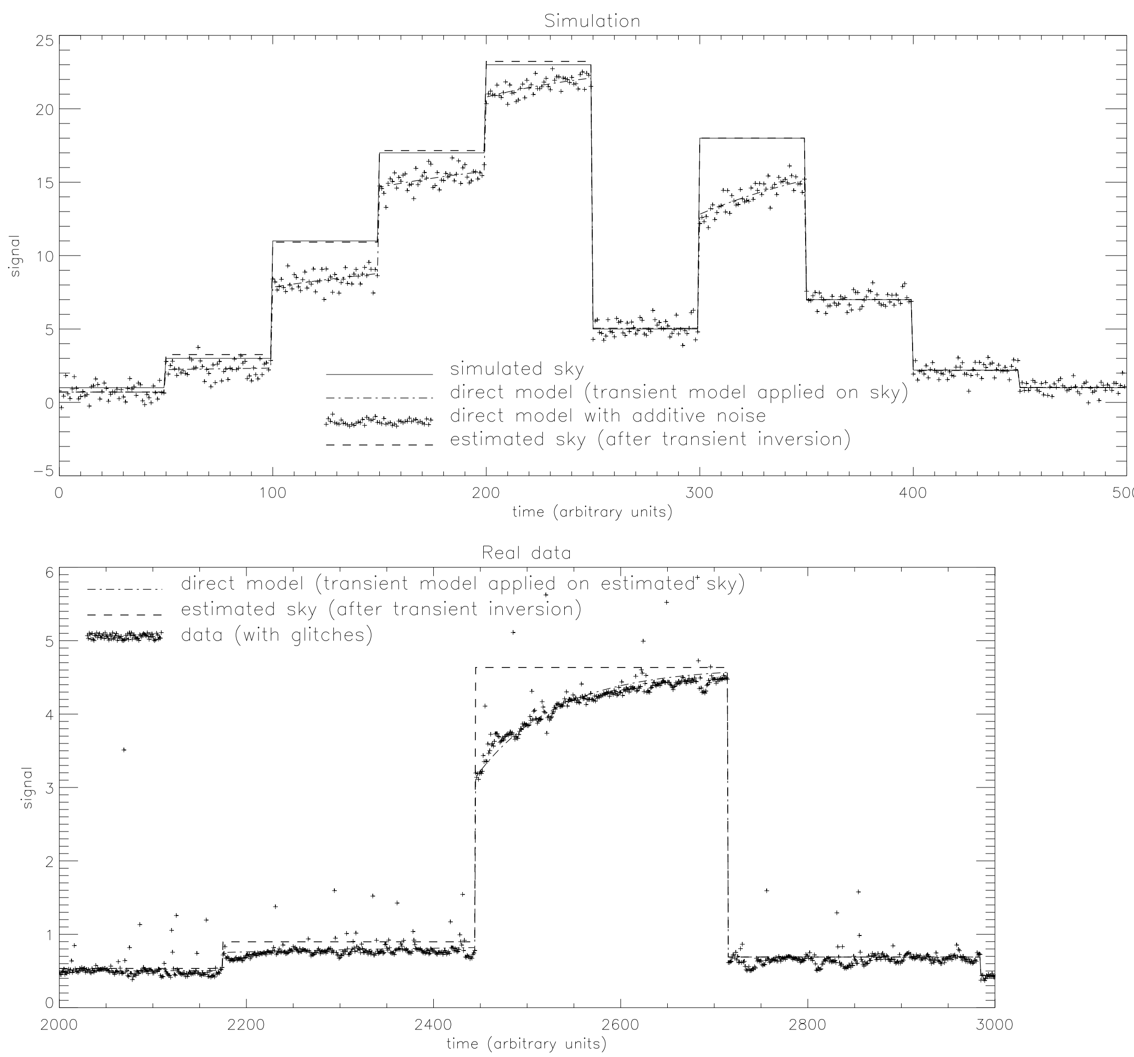

Figure 3.16: *Data processing according to the proposed approach. Fig. (a) illustrates simulated data processing while (b) results from real data processing in the presence of glitches, which give a limited overestimated value for the step. For real data, the data interblocks -when the satellite pointing direction is changing- are removed before processing. This is a simplification. In the future, these interblocks may be included in the processing to improve the accuracy of the correction.*

The responsivity of a detector can vary or drift on time scales ranging from less than one hour up to the entire science window of 16 hours. In the case of ISOPHOT, responsivity drifts were mainly observed for the doped germanium detectors (P3, C100 and C200) and are a result of both the illumination history of the detector as well as the rate of ionising radiation falling on the detector (see Lemke et al. 1993, and Patrashin et al. 1995). On the high parts of the ISO orbit these are mainly cosmic ray glitches, whereas closer to the radiation belts stronger variations due to the space weather conditions (see Castañeda & Klaas 2000) can occur. In order to restore the nominal responsivity, all detectors were cured after passing the radiation belts, at the beginning of each ISO science revolution. An additional re-curing was introduced at the middle of the revolution for the far-IR Ge-based detectors. Nevertheless, each ISOPHOT science observation contains at least one measurement with the internal calibrator, which can be used as a reference to determine the actual value of the responsivity.

The responsivity of ISOPHOT generally varied within long timescales as compared to common observing times. A statistical study of its variation along an ISO revolution was performed using a large set of observations, in which the values of actual responsivities were derived by the automatic OLP. The responsivity variation along the orbit position for each detector/pixel was fitted by a smooth curve (linear or parabolic fit at maximum). These curves were used to correct the default responsivity which is used in PIA and OLP. The mean variation of the responsivity for each detector is presented in Table 3.6, where R_i, R_m and R_e represent the responsivity at the beginning, the middle and the end of the science window of the ISO revolution.

Especially long integrations made with the same detector were affected by this effect. Examples are multi-filter photometry with PHT22 and multi-aperture photometry with P3 in PHT04. For large (raster) maps available in AOTs PHT03, PHT22, PHT32, and in the sparse map modes PHT17/18/19 and PHT37/38/39, the responsivity drift can be assessed from the two FCS measurements collected at the beginning and end of each map. We found that responsivity changes depend on the in-band power received by the detector (see Fig. 3.17): For high powers (larger than 5 V/s for P3 and C100, and 10 V/s for C200) the responsivity stays roughly constant, or it can even decrease, like a recuring effect, up to a factor 1.5 of the initial responsivity. Such drifts are very difficult to correct for. For low powers the responsivity increases drastically, with a mean rate of 40% hr^{-1} for C100, , 25% hr^{-1} for P3 and moderately with a mean rate of $\sim$ 2% hr^{-1} for C200. The rates for P3 and C100 are large compared to what is statistically observed along a revolution (see Table 3.6). There are several reasons which may explain such a discrepancy, among others we remark: the responsivity varies differently depending on the incoming infrared flux. On the other hand, it is not clear whether the responsivity variation is different for detector measurement or stand-by mode.

For polarisation observations the polarisers are cycled with a cycle time of 128 s per polariser to assess the long term stability of the detector during the observation.

Table 3.6: *Mean responsivity variation along an ISO revolution*

	No recuring	No Recuring	
Detector	$(R_e - R_i)/R_i$	$(R_m - R_i)/R_i$	$(R_e - R_m)/R_m$
P1	87≤0.05	...	
P2	36∼0.3	...	
P3	∼1.86	0.5	0.5
C100	1.9	0.33	0.75
C200	0.2	0.1	0.1

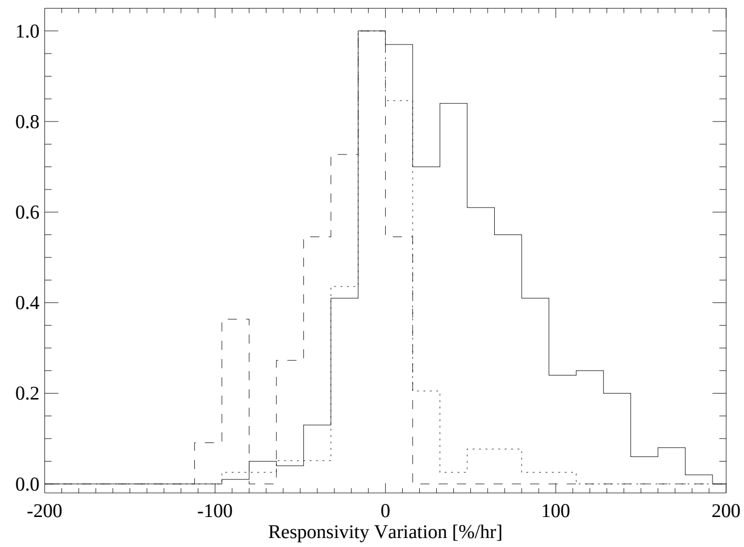

Figure 3.17: *Histogram showing the temporal variation of the responsivity for the central pixel of detector C100 and three different in-band power ranges. The continuous line represents the variation observed for low in-band power values, the dotted line for intermediate power values and the dashed line for high power values.*

Finally, the observed responsivity drifts for the doped silicon detectors P1, P2 and PHT-SS/SL were always less than 20% over the entire science window.

3.2.10 Observing strategies developed during operations

The study of transients led to the development of a PHT AOT logic intended to minimise disturbing effects by detector transients which was followed as much as possible during operations:

1. in multi-filter observations the measurements for a given detector were sorted according to increasing power on the detector

2. in multi-aperture photometry PHT04 the measurements were arranged according to increasing aperture size.

3. the absolute photometry AOTs PHT05 and PHT25 comprised relatively long (64 to 128 s) staring measurements in order to ensure a stable signal at the end of each measurement.

4. each PHT-S observation (PHT40) started with a dark signal measurement to assess the presence of possible transients still present from a previous observation of a bright target.

5. telescope nodding was made available to achieve repeated quasi-staring observations between target and one or more background positions. Nodding was suitable for photometry of relatively bright targets for which the high frequency of the chopper would have caused serious transient effects. The nodding mode was in essence PHT03/PHT22/PHT40 raster mode for which the step in spacecraft Z-direction was set to 0".

3.3 Results achieved

3.3.1 Drift recognition *vs* empirical models in staring PHT-P and PHT-C observations

We have already shown in Figure 3.15 an example of the application of the drift recognition model to a measurement taken with detector C100 in comparison with the result obtained using an empirical solution based on a single exponential function fitting to the same observation. This example clearly shows how the use of the drift recognition model as implemented in PIA and in the pipeline for staring PHT-P and PHT-C observations gives quite satisfactory results for relatively short measurements. Tests show that the use of drift modelling upon the first 16 s or 32 s significantly improves the estimate of the final signal. This is especially relevant to the relatively short measurements of the internal calibrator for a given science observation, which are used as references in the photometric calibration. Nevertheless, a detailed analysis of the transient curve, especially for C100, reveals the presence of more than one time constant.

Thus, an empirical correction based on a solution consisting of a linear combination of two exponential functions was also tried with satisfactory results when modelling the slow transient component in a large number of measurements. The difficulty is to determine the relative importance of the two components. A linear combination of three exponential functions has been proposed already by other authors (Church et al. 1996; Fujiwara et al. 1995).

Actually. in many cases, no much attention needs to be paid to the initial seconds after a flux change, where the hook response is observed, since it is not relevant for the in general long observation times. However, it may be important when treating high frequency chopped measurements. Sclar (1984) has proposed a description of the transient behaviour which reproduces the hook shape and may be applicable to the ISOPHOT detectors.

3.3.2 Calibration of PHT-S chopped observations

In order to test the absolute flux calibration method proposed for PHT-S chopped observations in Section 3.2.3, based on a direct comparison between the difference signal of the source and the background with that of a calibration standard of similar brightness, comparisons were made with observations taken through the LW2 filter of ISOCAM of a large sample of normal galaxies observed under a GT proposal by Helou et al. (see Fig. 3.18). The agreement found between the two independent calibrations is withing 20%.

We also checked the consistency of this method with the Fouks-Schubert model. Firstly, we corrected a triangular chopped measurement for chopped signal losses using Fouks-Schubert method as implemented in PIA. Secondly, we derived a corresponding SPRF by applying the Fouks-Schubert transient correction to the chopped measurements of the calibration stars (see Table 3.2). The PHT-S spectrum calibrated according to this scheme is presented in Fig. 3.19.

Also presented in Fig. 3.19 are the PHT-S spectra of the same source calibrated using the default SPRF and using the method presented in Section 3.2.3. The default SPRF is taken from the PHT-S Cal-G file SPECAL (OLP version 7), which was derived from staring observations of calibration standards. It is important to notice that this default SPRF is likely affected by transient effects.

It can be seen in Fig. 3.19 that the new calibration method produces a PHT-S spectrum consistent with the one derived using the Fouks-Schubert transient correction method while the agreement with the spectrum derived with the default SPRF is poor.

Measurements of two calibration stars (HR 6817 and HR 6847) which were used to establish the Relative Spectral Response Function for chopped PHT-S calibration were also checked in

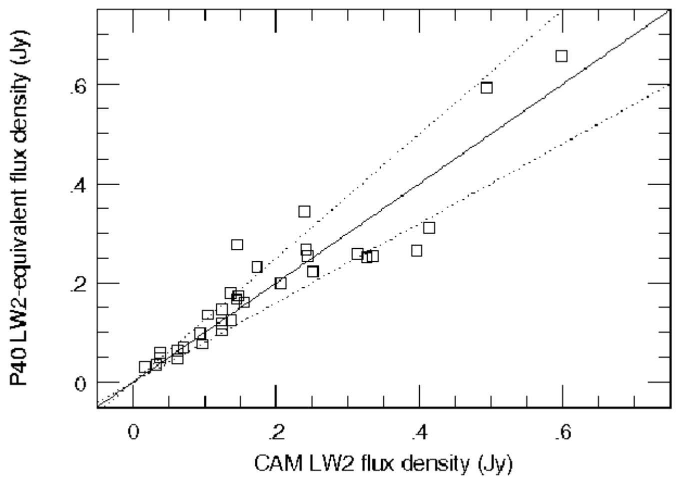

Figure 3.18: *Comparison of ISOCAM LW2 filter and chopped ISOPHOT-S measurements calibrated with the method described in Section 3.2.3. The solid line is the identity and the dotted lines indicate ±20% deviation from the identity. This graph is a courtesy from Dr N. Lu (IPAC).*

order to determine whether the input model SEDs were reproduced. Both calibration stars were measured both in rectangular and triangular chopped modes obtaining in all cases an excellent agreement with the models. The details can be found in the "Report on the PHT Scientific Validation for OLP Version 9.0" by Ulrich Klaas et al. available at:

`http://www.iso.vilspa.esa.es/users/expl_lib/PHT/phtolp90_scivalrep_v1.ps.gz`

3.3.3 Dynamic calibration of PHT-S staring measurements

We present in Figs. 3.20 and 3.21 the spectra of the calibration stars used in this method (see Table 3.3) normalized to the model spectra, as calibrated using the static method as in the old OLP implementation (a single Spectral Response Function applied to all cases). It is clearly noticed that large deviations (larger than 20%) from the model and many distorsions in the spectral shape appear. We have perfomed a cross-checking by calibrating each of the calibration stars with the two best matching stars in the database, but excluding itself (see Figs. 22-23). It can be clearly seen that in most cases the deviation from the models is confined to the range of ±20% and in many cases do not exceed 10%. We have also plotted in Figs. 3.24 and 3.25 the ratio between the measured signal and the calibrators involved, this ratio should be close to unity in order to have a reliable calibration. There are few cases in which the spectral shape is distorted, specially at the region below 3 μm; in most cases this is due to the lack of a good matching calibrator.

The application of the dynamic calibration method to the correction of transients in PHT-S staring observations brings down the errors associated to this observing mode (sometimes as high as 30%) to just a few percent.

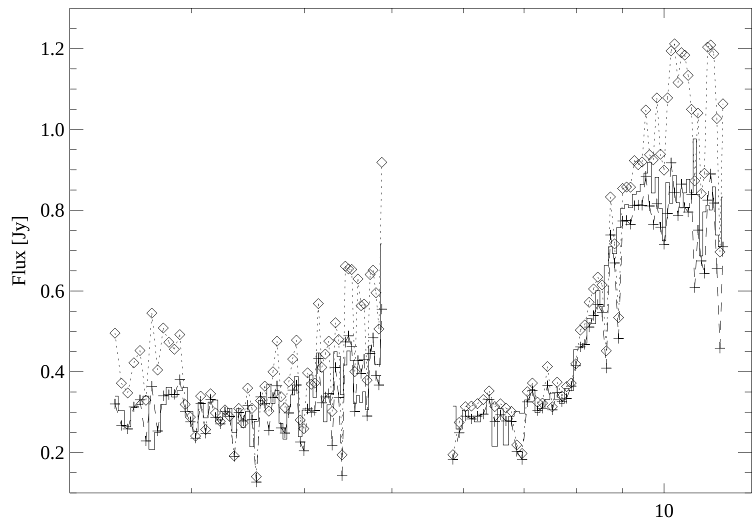

Figure 3.19: *Comparison between the calibration method of chopped PHT-S observations proposed in Section 3.2.3 and the FouksSchubert transient correction method. The meaning of the symbols is as follows: the new calibration is represented by the continuous line (histogram type); transient corrected data and calibrated by the transient-free SPRF and the default SPRF are represented by crosses (joined by a dashed line) and diamonds (joined by a dotted line), respectively.*

PHT-S measurements of some of the calibration stars (HR7001 = Vega, HR2491 = Sirius, HR 5340, HR 7469, HR 7924 and HR 8487) that were used to establish the dynamic relative spectral response function surfaces of Cal-G file PSDYNAMIC were checked in order to determine whether the input model SEDs were reproduced. The results obtained show that the method represents a significant improvement with respect to the static default response function applied in OLP v8.4, up to 10% level of agreement or better at a wide range of flux levels.

3.3.4 Transient effects in PHT32 chopped raster maps

As we have already mentioned, a PHT32 processing prototype including full transient modelling has been developed at MPI-Kernphysik (Heidelberg) by Richard Tuffs with the collaboration of the ISO Data Centre at VILSPA.

The program has recently been integrated in the ISOPHOT Interactive Analysis (PIA) and the results obtained are quite satisfactory (see Figures 3.26 and 3.27)

The algorithm used, however, is highly interactive and requires a considerable level of expertise from the user.

3.3.5 Transients in Ge:Ga PHT C-100 detectors

Simulations show that the empirical non-linear model proposed in Section 3.2.8 properly inverse the system and correct the transients and the reconstruction error is less than 1%. In the case of real data analysis the method seems to work as well as for the simulated data but the presence of glitches tends to slightly overestimate the stabilized value.

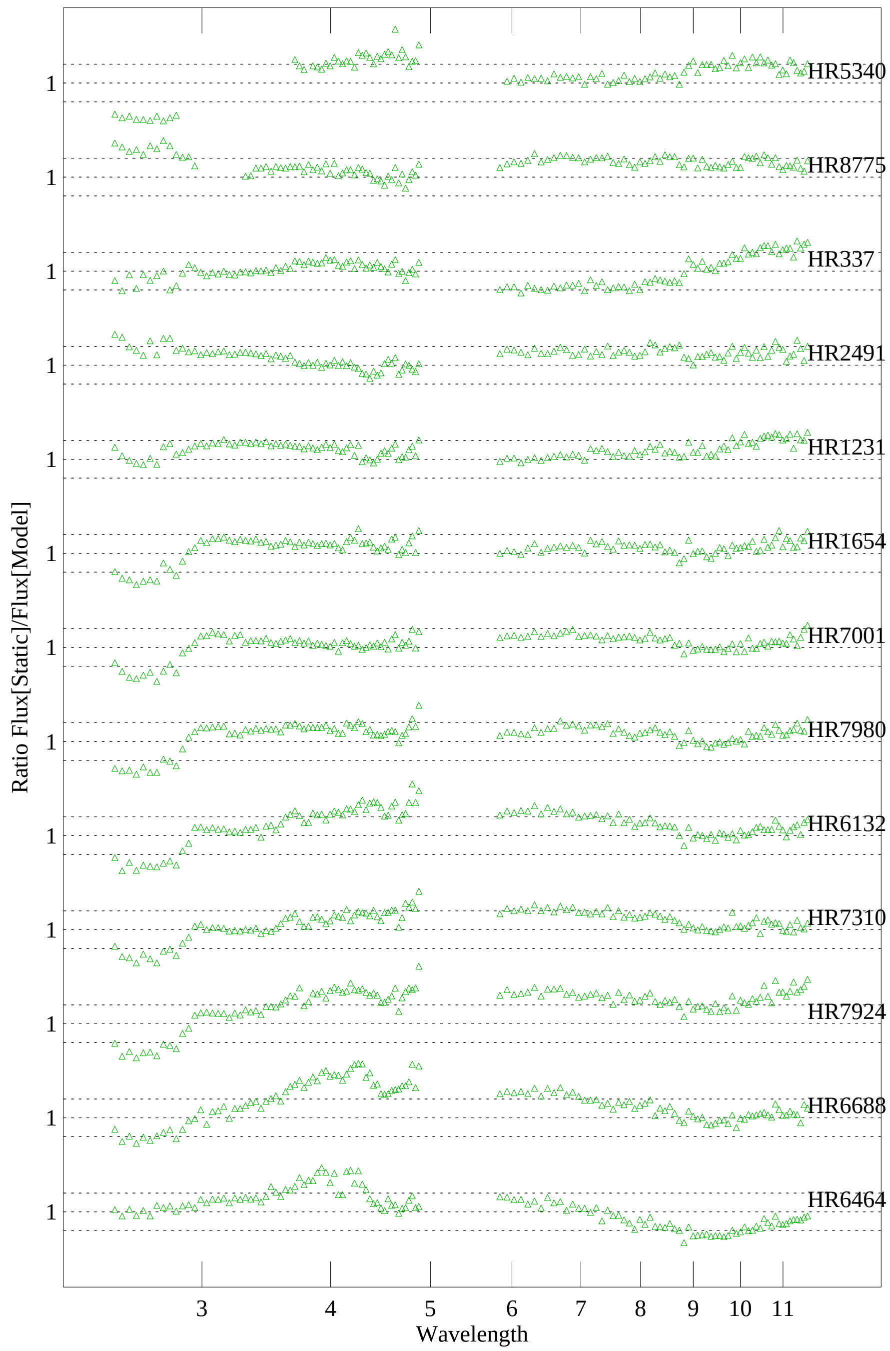

Figure 3.20: *Ratio of the statically calibrated spectrum versus model for all stars listed in Table 3.3. The horizontal lines above and below 1 represents a deviation of 20%*

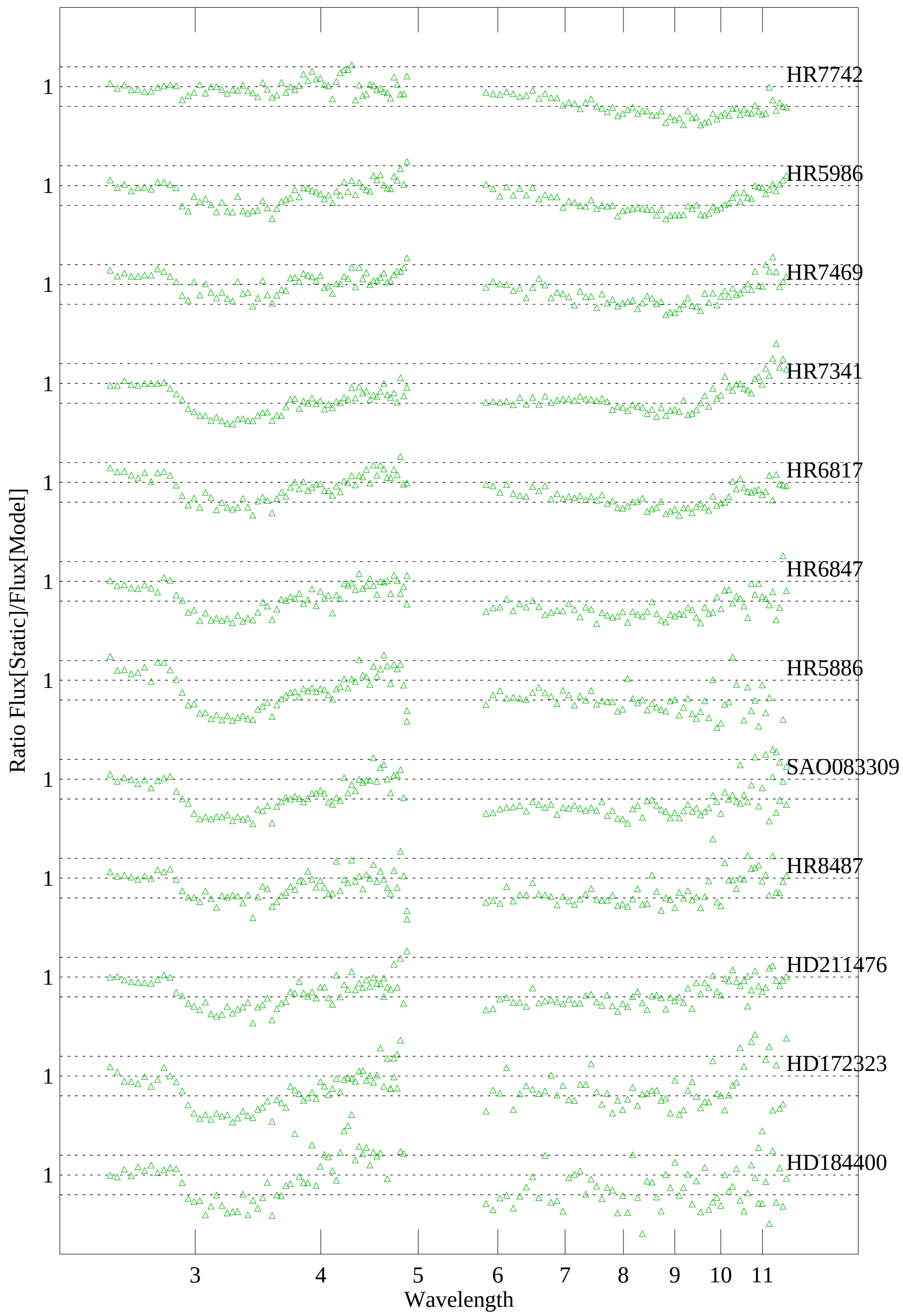

Figure 3.21: *Continuation of Fig. 3.20*

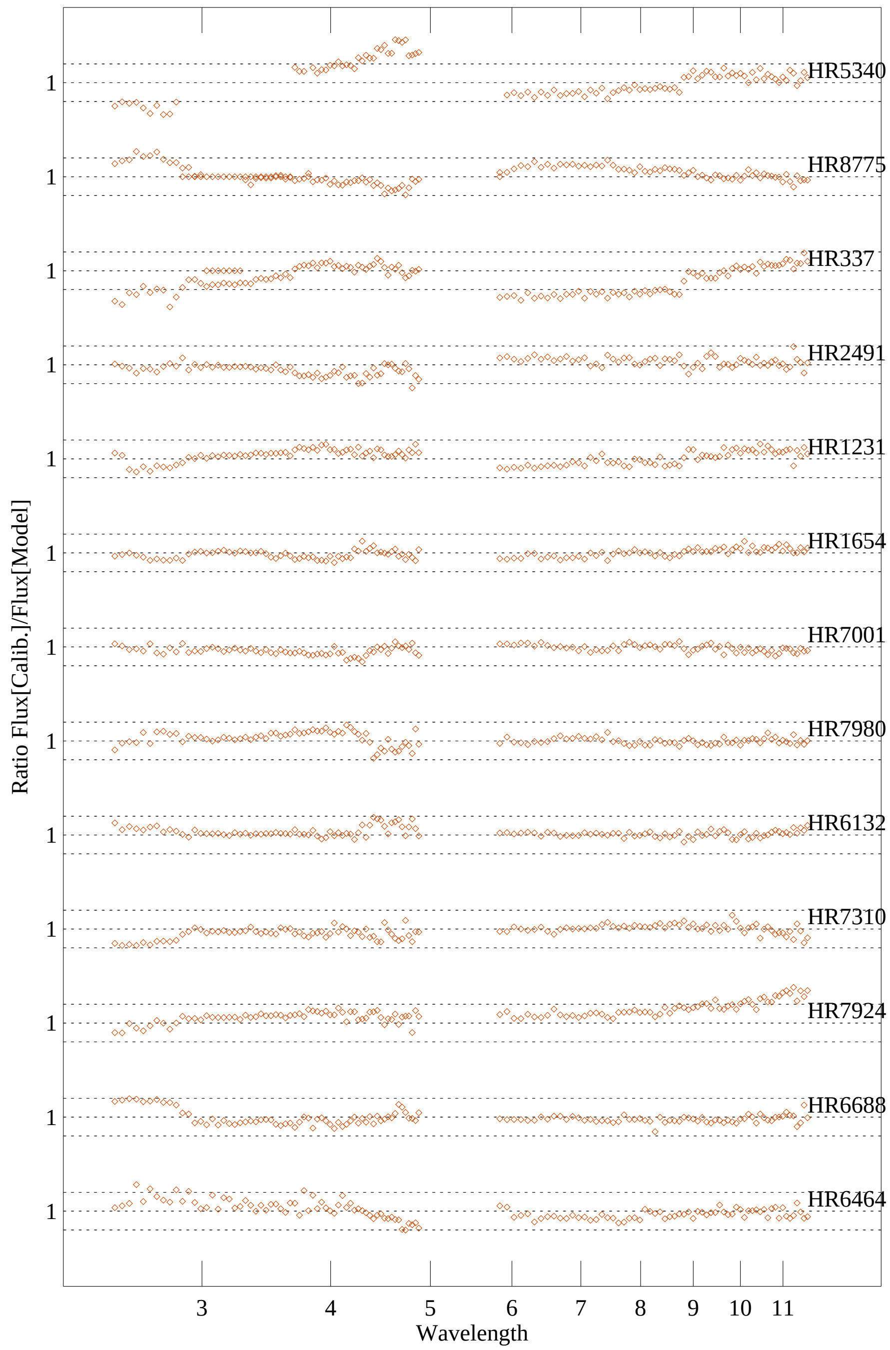

Figure 3.22: *Ratio of the dynamically calibrated spectra versus model for all stars listed in Table 3.3. This is a cross-checking, each star is calibrated using the two closest entries in the database excluding itself. The horizontal lines above and below 1 represents a deviation of 20%.*

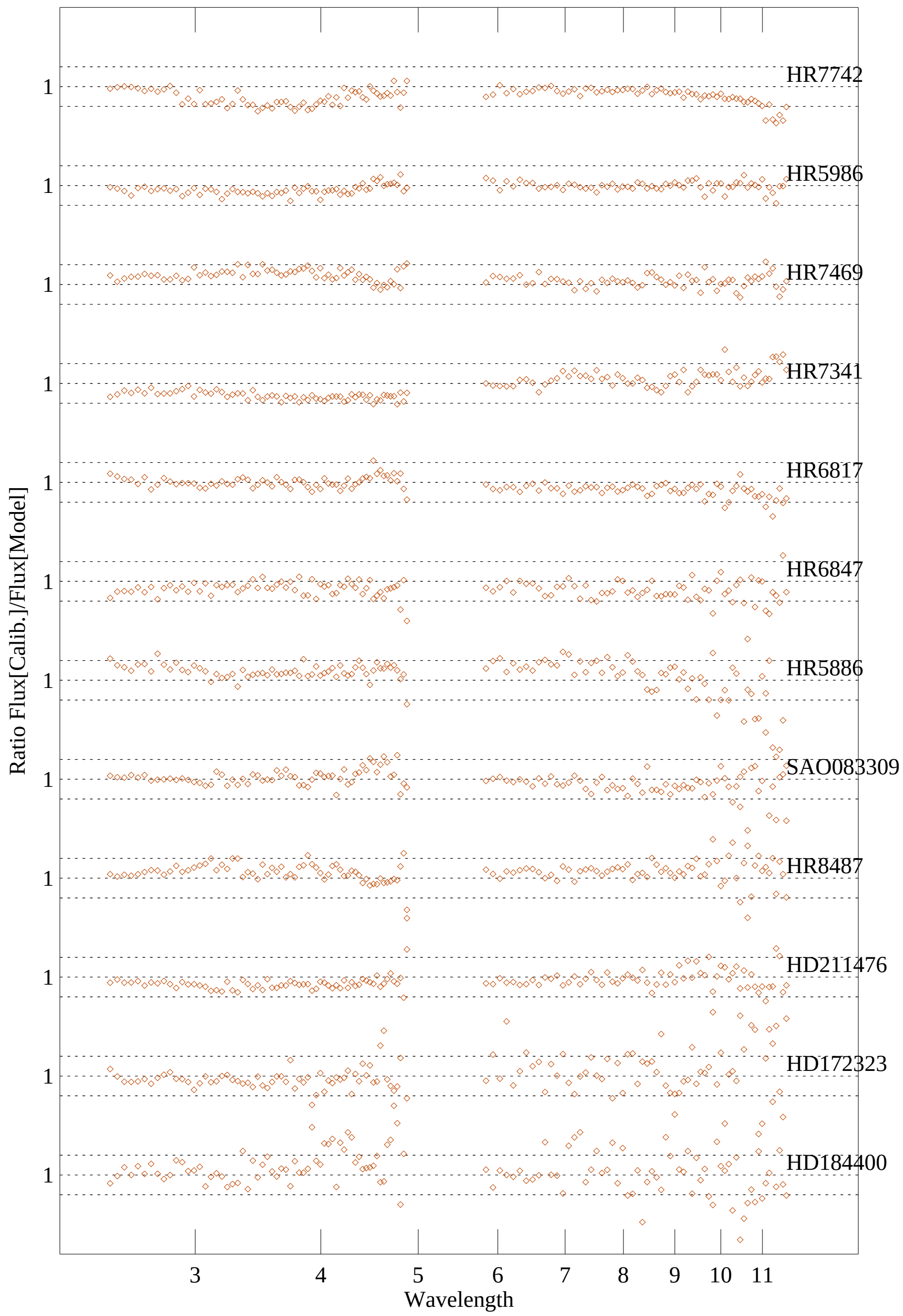

Figure 3.23: *Continuation of Fig. 3.22*

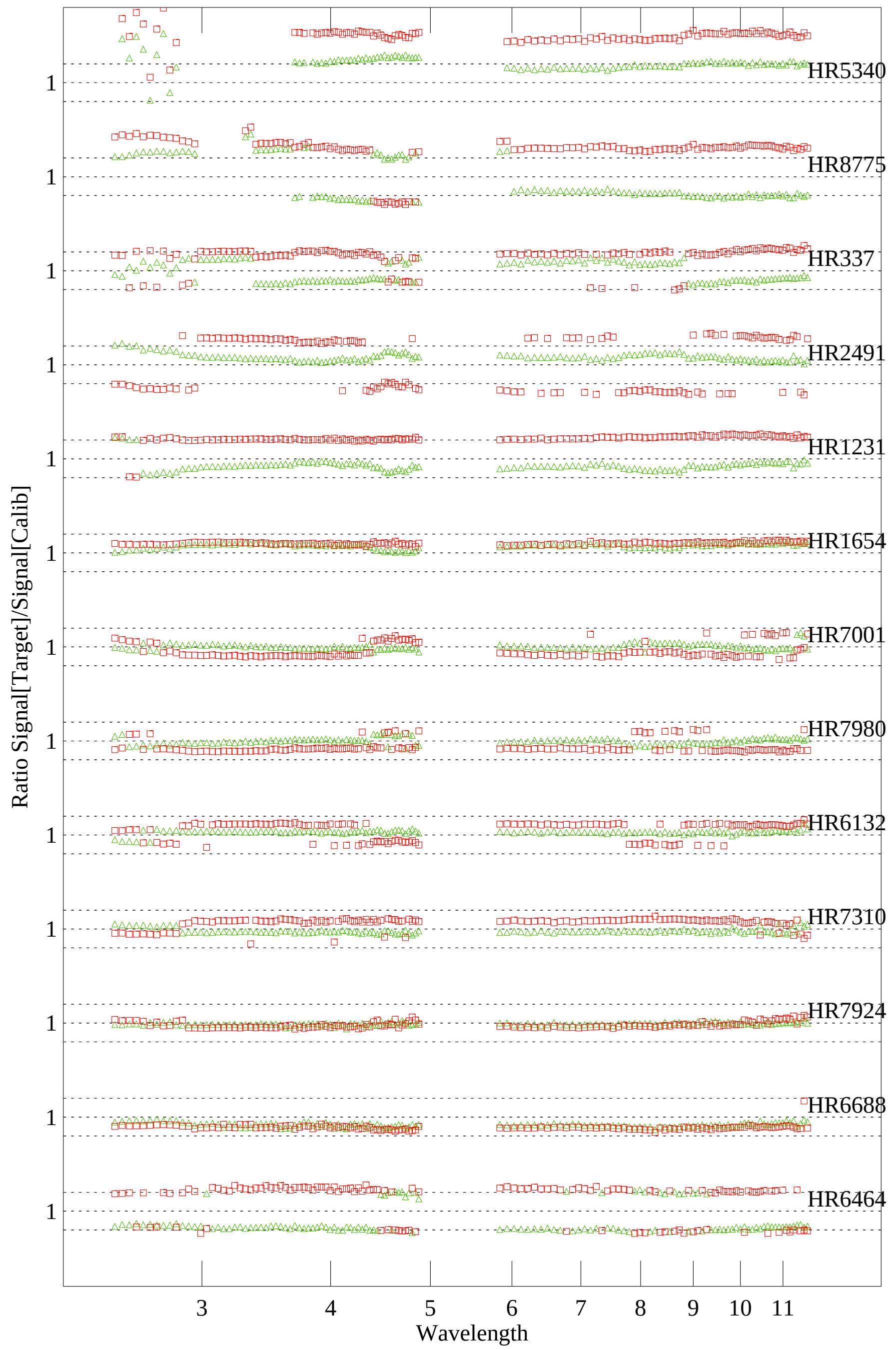

Figure 3.24: *Ratio of the uncalibrated signals versus the reference spectra for all stars presented in Fig. 3.22. The horizontal lines above and below 1 represent a difference of factor 2. The two calibrators are represented by two types of symbols and colours.*

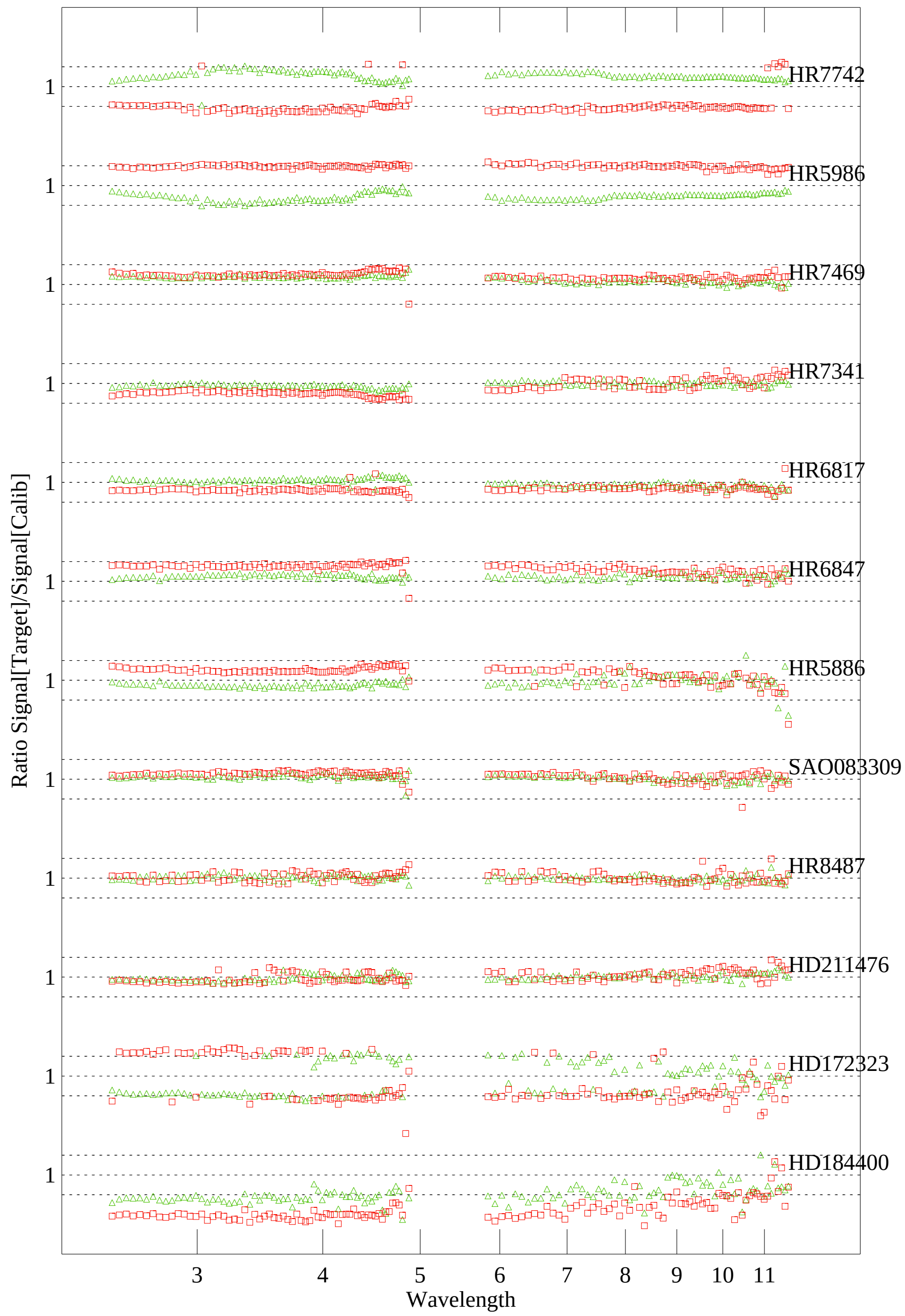

Figure 3.25: *Same as Fig. 3.24 for the stars shown in Fig.3.23*

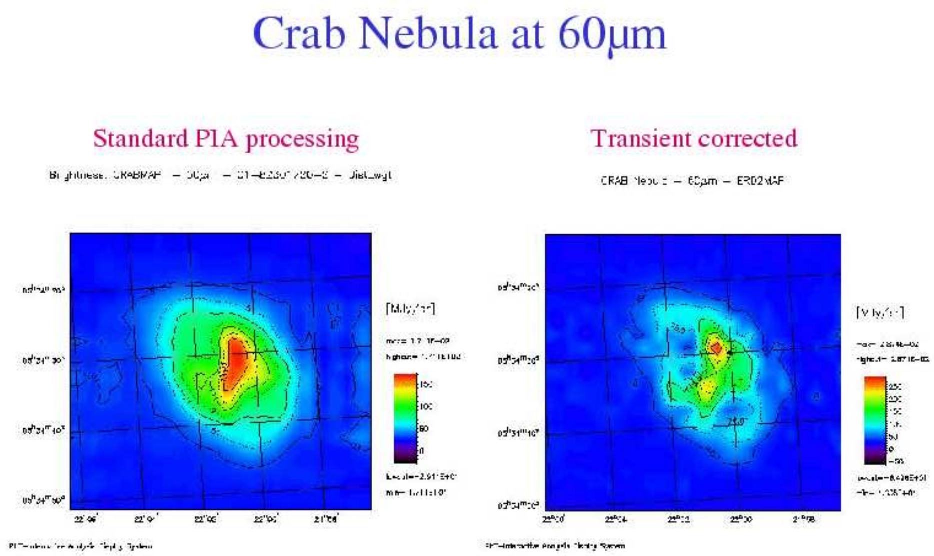

Figure 3.26: *PHT32 map of the Crab Nebula at 60 µm with standard processing (left) and after application of the new transient correction (right) - Richard Tuffs*

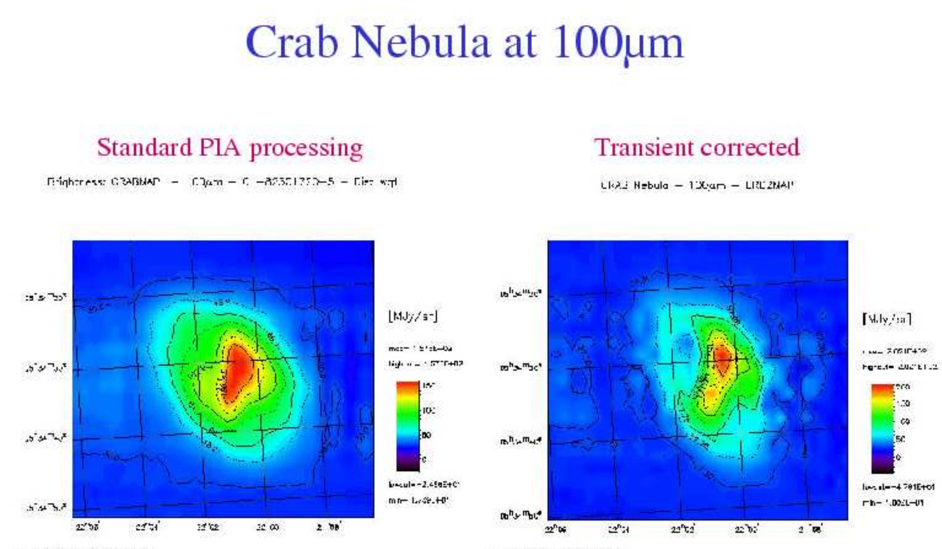

Figure 3.27: *PHT32 map of the Crab Nebula at 100 µm with standard processing (left) and after application of the new transient correction (right) - Richard Tuffs*

In addition, there are still problems with the method because of the known limited accuracy in the FCS, the limited accuracy in the determination of the (β,λ) maps for the 3×3 detectors (using median value at this moment) and the non-stationary noise of the detector, whose impact on the method is still under study.

In parallel, comparison of ISO maps taken with C100 detectors are being made against IRAS maps of the same fields which show that the consistency in relative flux level is within 5%.

3.4 Implementation in PIA/PHT pipeline

3.4.1 Transient corrections in PIA

As we have already mentioned, several transient corrections are available within PIA. In most cases, they are highly interactive methods which require a visual inspection of the quality of the fit made.

They include drift recognition using the non-parametric Mann statistical test especially for P1 and P2 filters, empirical solutions based on exponential functions for the Ge:Ga type detectors (P3, C100 and C200); or the Fouks-Schubert correction, that can be applied to P1 and P2 filters (Si-based) as well as to PHT-S measurements in the absence of hook responses.

In general, the approach in all cases is to fit the observed signals and to predict the final stabilized value. The fitting procedure begins with the estimate of suitable starting parameters corresponding to the current data and the model to be used. The minimization of χ^2 is done in two steps: a first parameter determination is done using a downhill simplex method (AMOEBA), and these parameters are used as starting values for a second fit using a gradient expansion algorithm.

A Graphical User Interface has been developed which includes the possibility of: (a) choosing among different functions with their corresponding parameter initialization depending on the detector, (b) fixing or releasing parameters in the fit, setting specific values or limits and (c) setting selection criteria, tolerance degree of the fit and weighting method to be applied. All the start parameters can be tested and fine tuned before all detector pixels are processed. After the bulk processing, PIA also provides the possibility to examine interactively the fit results and re-evaluate non-satisfactory fits. A flag system has been developed which checks whether a number of criteria (e.g. convergence of the minimization, χ^2 is below a certain threshold, free parameters within range) are fulfilled. This makes the analysis of large data sets very efficient, while permitting fast and deep data correction.

Concerning PHT-S chopped measurements, although the possibility exists under PIA of applying the Fouks-Schubert method to correct for transients but, as we have already mentioned, in many cases the signal-to-noise ratio is low and the method cannot be applied. In this case, the method proposed in Section 3.2.3 is more adequate and it is also implemented in PIA.

Finally, and concerning PHT-S staring observations, the necessary tools to perform the dynamic calibration presented in Section 3.2.4 were also developed and integrated in PIA v7.3. The dynamic calibration requires SRD level input data which have been dark current subtracted and deglitched, From that point, the steps that should be followed to get a flux calibrated spectrum using PIA are:

- Selection of calibration sources:

  - *Automatic mode:* a given number (by default is 2) of the best matching calibrators is found, based on the signals measured at 16, 32, 64, 128 and 256 s. A higher weight is given to signals obtained later in the measurement. The selection is done independently for each pixel.

- *Expert mode:* the number of calibrators and a preselection of them can be done, however a certain knowledge of the calibrator and target to be calibrated is needed a priori.

- Take the ratio of target signals to the modelled signals (Chebyshev expansion) of the calibration stars at the same measurement time. Then, the mean and median values are computed, which yields the flux scaling factors. The best calibration is obtained when the ratio along time is constant and close to unity. Discarded points (glitches, first measured signal, etc) from the target are not included. The fraction of the measurement which is used to compute the ratio can be selected interactively. The statistical error of the calibrated flux (from a single calibrator) is obtained as the scattering of the signal ratios.

- The calibration factors obtained for a given pixel can be combined in several ways:

  - *No weight:* All factors the same weight.

  - *According to signal ratio:* largest weight is assigned to the one corresponding to a signal ratio closer to unity.

  - *According to signal ratio uncertainty:* largest weight is assigned to those calibrators whose signal ratio have a smaller uncertainty.

In order to illustrate the importance of an adequate selection of the reference stars when applying this calibration method to PHT-S staring measurements we show here as an example a cross-calibration analysis made by Thomas Müller (ISO Data Center) on the asteroid Hygiea. The problem resides in the fact that some of the reference stars listed in Table 3.3 used in this method are late type stars for which the currently available models do not reproduce well the SiO (7.5-10.5 μm) and CO (4-6 μm) absorption features causing artificial emission features in the dynamically calibrated science spectra. The effect can be seen in Figure 3.28, where we show the SWS spectrum of the asteroid Hygiea, not affected by this problem, around the spectral region corresponding to the SiO feature, divided by the assumed thermo-physical model (provided by Thomas Müller), compared with the PHT-S staring spectrum of the same source calibrated using this *dynamic calibration method* (1) using all the reference stars in Table 3.3 without any restriction and (2) excluding the late-type stars from this list. As we can see the dynamic calibration works extremely well, assuming that the SWS spectrum is esentially correct, only in this second case. Otherwise, artificial spectral features are produced in the spectrum at the wavelength region corresponding to the SiO feature up to the $\sim$10% level. The effect is reduced to a residual 3-5% level in the case of the application of this method in the automated pipeline, since for the automatic approach in the OLP, the transient behaviour with time for the different flux (signal) regimes is characterized by surfaces stored in the new Cal-G file PSDYNAMIC constructed from the library of standard stars which smooth the effect of potential problems in the available models for individual stars on the output spectra.

Note also that this undesired effect will only visible in the calibrated spectra derived from the pipeline if the observed flux level agrees with the flux level of these late type reference stars at the wavelength range corresponding to the CO or SiO bands (10-100 Jy at 4-6 μm, 5-30 Jy at 7.5-10.5 μm).

3.4.2 Transient corrections in OLP

Drift recognition using the non-parametric Mann statistical test is the transient correction method implemented in the pipeline for observations taken in the P1 and P2 filters, while

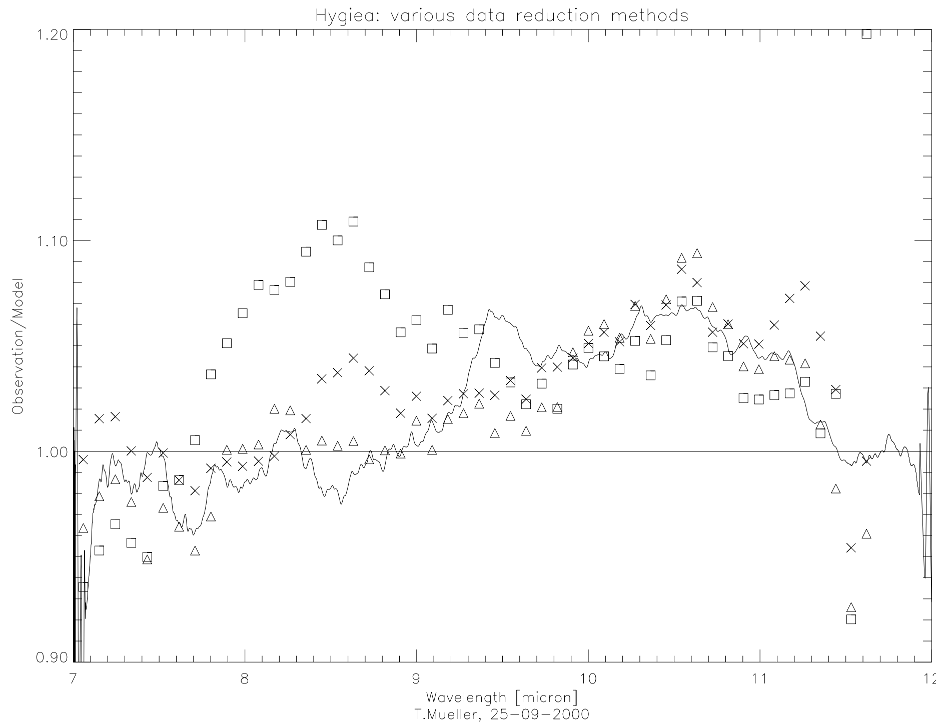

Figure 3.28: *The SWS spectrum of Hygiea (solid line), divided by a thermo-physical model of this asteroid provided by Thomas Müller is compared with PHT-S measurements of the same asteroid, also divided by the same thermo-physical model calibrated using the so-called dynamic calibration method (1) using all the reference stars in Table 3.3 without any restriction (squares), (2) excluding 4 late type standard stars in the reference list (triangles) and (3) with the method, as it has been implemented in the pipeline since OLP v9.0 (crosses)*

empirical solutions based on the fitting of exponential functions are used for those taken with Ge:Ga type detectors (P3, C100 and C200) in staring mode.

For reasons that have already been mentioned the Fouks-Schubert correction method cannot be implemented blindly in the pipeline and it is restricted to PIA where it can be applied interactively to observations taken with the P1 and P2 filters (Si-based detectors) as well as to both chopped and staring PHT-S measurements in the absence of hook responses and/or when the signal-to-noise ratio is enough to perform a reasonable fit.

PHT-S chopped observations are corrected for transients in the pipeline using the method described in Section 3.2.3 based on a direct comparison between the difference signal of the source and the background with that of a calibration standard of similar brightness. An example of the quality of the results obtained after this correction is applied to ISOPHOT data is shown in Section 3.3.2.

With respect to PHT-S staring observations, the dynamic calibration method is prefered and this is is used as part of the OLP processing since version 9.0. The calibration using this method is performed by comparing the signal time evolution of the target star with a that of a set of standard stars at similar flux levels. Usually, the accuracy of the results obtained after this correction is applied is better than 10% and the spectral shape is well preserved. In OLP v9.0 the method has been automated by creating surfaces (stored in the Cal-G file PSDYNAMIC) constructed from the library of standard stars listed in Table 3.3 which are just the result of the interpolation of all different calibration observations, and describe the temporal behaviour of each PHT-S detector pixel under different illumination conditions.

As a result of this interpolation, undesired effects produced by inaccurate stellar models (in the case of reference stars with late spectral types) are softened with respect to the results obtained using the same meethod as implemented in PIA. This is illustrated in Fig. 3.28, where the PHT-S staring observation of Hygiea calibrated using OLP version 9.0 is shown (crosses) together with the result obtained using PIA with and without including the problematic stars, and also in comparison with the SWS spectrum. As we can see, a residual effect attributed to this incorrect modeling of the SiO band in the late type standard stars used as reference for the determination of the calibration surfaces is still seen in the OLP version 9.0 PHT-S spectrum at the 3-5% level (to be compared with the 10% errors obtained when all stars are considered and the method is applied using PIA and the almost absent effect - and perfect agreement with the SWS spectrum - when the calibration is done by excluding these calibration stars from the reference list).

In the case of chopped PHT-P and PHT-C observations, where non-stabilized signals cause significant losses on the true difference signal, OLP makes use of the *generic pattern* method described in Section 3.2.6.

Finally, as we have already mentioned, no transient correction was implemented in the pipeline for PHT32 chopped raster maps because of the high interactivity needed in the processing to correct these maps for transient effects using PIA.

Chapter 4

Transient effects in SWS data

4.1 Impact on SWS detectors

Memory effects affect SWS data in bands 2 (Si:Ga) and 4 (Ge:Be) and in the Fabry-Pérot bands (Si:Sb and Ge:Be) (Wensink et al. 1992; Kester 1999). The bands 1 (In:Sb) and 3 (Si:As, BIBIB) are completely free of these obnoxious effects (Kester 1999).

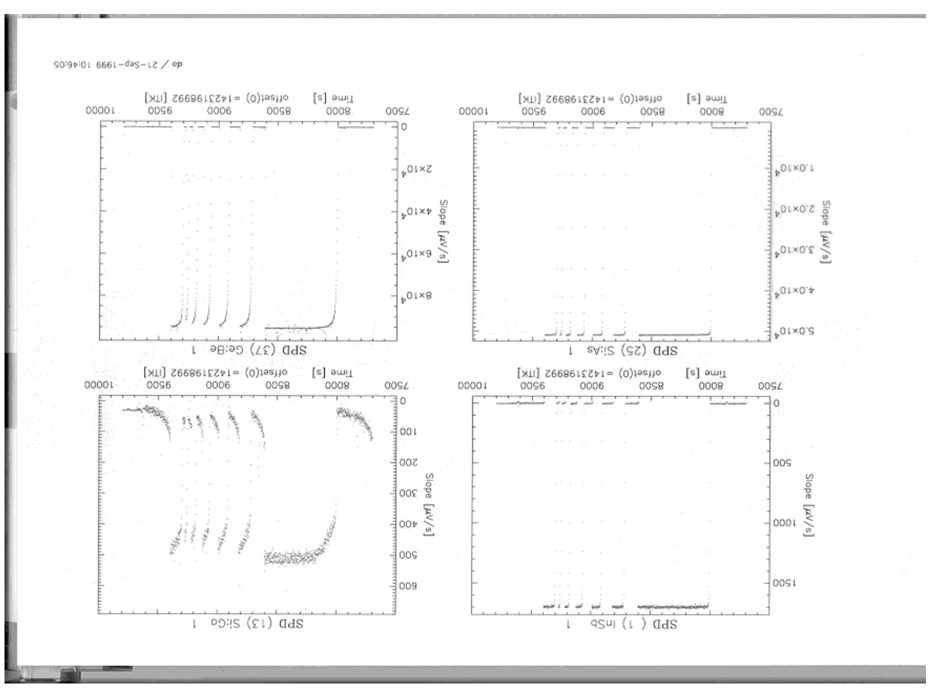

Figure 4.1: *Example of the various transient behaviours observed for the different SWS bands as a function of the detector material (Band 1: InSb; Band 2: Si:Ga; Band 3: Si:As; Band 4: Ge:Be) - Do Kester*

The signature of memory effects is that the up- and down-scans are different in flux level. The down-scan normally succeeds the up-scan in the AOT and appears to be already 'accustomed' to the flux level.

4.2 Efforts developed to correct SWS data for transient effects

4.2.1 Memory effects in band 2 data

An adapted version of the Fouks-Schubert model has been developed by Do Kester (Kester 1999) and succesfully implemented in version 10 of the SWS pipeline to correct band 2 data for transient effects as well as in the SWS Interactive Analysis (SIA) software package. The method brings the errors (sometimes up to 20%) down to the few percent level. Soon it will also be implemented in OSIA v3.0.

The Fouks-Schubert model is written for semi-stationary fluxes, where the *semi-* part reflects the fact that the detectors do not have to be in an equilibrium state when the next flux step takes place. For both CAM and PHOT these assumptions are quite valid. For a spectrometer like SWS the flux changes continuously. But with some audacity we could see every reset interval, or even better every step of the grating scanner as a new constant flux level. The detectors are (almost) never in an equilibrium state but that is taken into account in the formulae.

Transient model

The original Fouks-Schubert formulae can be rewritten, using some elementary algebra (see appendix A for derivation), into a form which is more suitable for SWS.

$$I_k = \beta F_k + \alpha_k \tag{4.1}$$

$$\alpha_k = \frac{(1-\beta)\alpha_{k-1}F_k}{\alpha_{k-1} - (\alpha_{k-1} - (1-\beta)F_k)\exp(-\Lambda\Delta t\beta F_k)} \tag{4.2}$$

Here I_k is the current through the detector at time k, F_k is the incoming flux, β is a constant, to be estimated from the data, and α_k comprises the memory effects. We see that α_k depends on its previous value: α_{k-1}, on the present flux, F_k, on the constant β and on another constant Λ. Δt is the duration of the time step from $k-1$ to k. With a bit of reflection on these formulae we see that the current is related to the flux via a constant gain β and a *changing* dark current α. It is a fortuitous coincidence that we used this gain and dark model already in the pipeline. Actually it is better to identify the product of βF_k with the incoming flux as it even better reflects our present model of current = flux + dark; at least that is our model at the stage of dark current subtraction. The absorption of this constant factor in the subsequent calculations is trivial.

When the incoming flux is zero, i.e. when measuring with a closed shutter (in SWS terminology a 'dark current measurement'), the above expression for α breaks down. It yields 0/0. Using l'Hôpital's rule we find a new expression for α when $F_k = 0$:

$$\alpha_k = \frac{(1-\beta)\alpha_{k-1}}{(1-\beta) + \alpha_{k-1}\Lambda\beta\Delta t} \tag{4.3}$$

This latter expression decays to zero. And it decays in a more or less hyperbolic sense, just like it is observed in the Si:Ga detectors. Actually α is always positive. The incoming flux and the constant β are also positive (or zero for dark current flux), so the current (in this model) is positive definite. In true life we measure also (dark) values which are negative for some detectors. We must conclude that the model is not yet complete: the zero level in the data cannot be mapped directly on the zero of the model. This is not so disturbing as the zero in the data can be changed somewhat arbitrarily by changing for instance the value of MIDBIT (ISO SWS Handbook - Leech et al. 2000). We observe e.g. that the zero level is changing when the gain setting changes and also when the length of the reset interval changes. All these stepwise changes are *artificial* in the above sense.

Thus, we have expanded the model by adding a model zero level[1]

$$I_k = \beta F_k + \alpha_k + Z. \tag{4.4}$$

Determining the zero-level function (ZLF) proved to be quite complicated, as especially the behaviour at low fluxes is really sensitive to the zero level. After lots of experimenting, we settled on piecewise linear functions between dark currents of the same gain setting. In this way, Fouks-Schubert model at low fluxes behaves very similar to the standard dark current subtraction used in all previous pipeline versions which was deemed correct at low fluxes. The zero level can vary a little over time. We do not know exactly what effect is modeled with this. It might be another (part of the) memory effect which is not captured by the Fouks-Schubert model, maybe some long term drift. Anyway, it seems necessary.

Parameter estimation

Now we have a (forward) function which relates the measured current to the incoming flux in a complicated, non-linear fashion. We only have to invert the relationship. Fortunately the constant β proves to be quite large (≈ 0.8) so we can do the inversion iteratively

$$F_k = (I_k - \alpha_k - Z)/\beta \tag{4.5}$$

where α_k is calculated with the values of F_k from the previous iteration. For most observations the flux stabilizes after half a dozen iterations.

In total we have $3 + N_Z$ parameters: β, Λ, α_0 plus the parameters needed in the ZLF, α_0 being the value of α before the observation started. The first two parameters are material constants, i.e. they might be fixed over the mission and if that is the case they would have to be estimated only once. The others are related to the flux history in some sense. As this history is unknown these parameters have to be estimated for each observation separately. Note however that the ZLF is chosen to be linear. Consequently for each choice of β, Λ and α_0 the ZLF-parameters can be estimated directly, simplifying the non-linear seach for the other parameters. Anyway, all parameters have to be estimated at least once.

To estimate the parameters we use the redundancy in each observation: up-down and 12 detectors covering more or less the same spectral area. We set up an iterative scheme.

1. Calculate the spectrum, S_λ, from all detectors.

$$S_\lambda = \mathcal{R}(g(Y_k - D_k)), \tag{4.6}$$

where $\mathcal{R}$ is a rebin function, Y_k is the SWS data in band 2 and D_k is the dark current. As the different detectors have (slightly) different sensitivities, we could profitably use per

[1]The other 3 instruments of ISO consider the virtual zero level as the dark current and α as the memory effect. Our discussion here is about 'relaxed' states; so dark current is the output of the detector when it has been looking for infinite time at a closed shutter. Although this is confusing sometimes, the only actual difference in the final result is a constant factor $1/\beta$ only.

detector a gain factor, g. The values for g are taken from SWS calibration file 43 which lists the flatfield constants of all AOT bands. The actual values of g are unimportant as they only serve to tighten the spectrum. Later they are divided out again. For the dark we start with the standard pipeline dark. Rebinning should be done such that there is sufficient (but not too much) overlap between the detectors. There are several subtleties with orders and apertures which make this exercise not as straightforward as it might seem. The spectra have to be made for all apertures, including calibration sources, separately and wavelengths have to be calculated in order equal 1. This is necessary to avoid overlap of parts of the spectra that for this procedure have nothing to do with each other.

2. Extract 'incoming fluxes' from the spectrum. At every time step and for every detector in the observation we 'know' what wavelength we are observing. To get the incoming flux at that time-step we read the value of the spectrum at the appropriate wavelength and use that value as flux F_k. Here we divide out the gain factor g to get the incoming flux valid for each detector.

3. Find the parameters for which the model equations 4.4 and 4.2 best fit the data.

$$\chi^2 = \sum_k w_k (I_k - Y_k)^2 \tag{4.7}$$

must be minimized. The w_k are weights of the individual data points. They are derived from the standard deviations of the slopes which represent the measured currents (see ISO SWS Handbook - Leech et al. 2000). The weights at the dark current samples are increased by a factor 10 to make sure that the model fits them well. These are the only samples where we know exactly what the incoming flux is: no flux is entering. For similar, contrary reasons at samples where we have no run-flag or where we are looking at one of the calibrator sources, the weights are *decreased* by a factor 10. The χ^2 minimization procedure is done for each detector separately. We use a version of simplex down-hill algorithm of Nelder-Mead (Press et al. 1992) to find the minimum.

4. Calculate the dark. At the minimum of χ^2, i.e. with the optimal parameters we calculate the dark current, D_k as a function of time.

$$D_k = \alpha_k + Z_k \tag{4.8}$$

And with this dark we recalculate the spectrum: go back to step 1.

This scheme is iterated until the change in χ^2 summed over all detectors is negligible (<0.001).

Error calculation.

When we have arrived at the minimum value for χ^2 the standard deviations and covariance matrix for all parameters is calculated, using a Gaussian approximation at $\chi^2_{\rm min}$. Typical errors that we find in a good observation are a few permille in β, a few percent in Λ and of the order of 1 μV/s in the other parameters (α_0 and the ZLF). However, we are not so much interested in the formal errors in the parameters but much more in the effects they have on the calculated dark current. We used a Monte Carlo scheme where the dark current is calculated 25 times, each time with another randomized set of parameters, drawn from a multidimensional Gaussian distribution representing the full covariance matrix. At each sample the standard deviation of these 25 dark currents is taken as the formal error.

Detector constants.

The parameters can be estimated properly when an SPD is used with sufficient dynamic range between 100 and 5000 μV/s. For fluxes much larger than 5000 μV/s, other memory effects than the ones we are modeling are becoming important. On the other hand when the flux range is too small ($< 100\mu$V/s) not enough memory effects are present to allow proper extraction of parameters. In that case it is possible by keeping the parameters β and Λ fixed and fitting the others to nonetheless get proper transients, which will not be much different from the dark current the pipeline would yield.

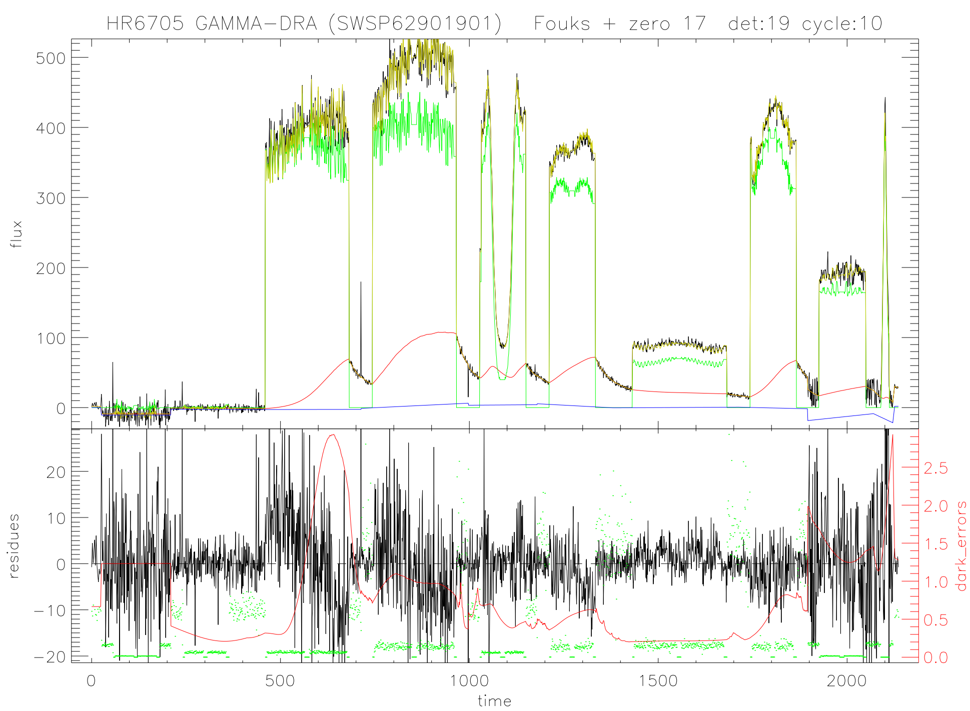

Figure 4.2: The memory model for detector #19 for γDra. In the upper panel: black is the data, green is an estimated input flux, red is the contribution of the memory model, blue is the virtual zero level and yellow is the sum of the input flux (green) and the memory model (red). It can be compared directly to the actual data (black). In the lower panel: black is the residuals, the difference between black and yellow, above. Green is the weights of the data points to be read on the red scale (on the right) and red is the uncertainty in the memory model also on the red scale.

In figure 4.2 is shown as an example how the memory model changes over time for one detector during an observation of the calibration star γDra. In the upper panel the measured data is plotted in black, the incoming flux in green (symmetric in up-down), the transients, α_k, in red and the zero level in blue. Note that the measured data go below zero and that consequently the model zero level is also below zero. In yellow the mock data (incoming flux + dark) is plotted. They are compared to the true data to calculate χ^2. The memory model has some real impact whenever the flux is more than a few 100 μV/s e.g. between time 500 and 1000. On the other hand when the flux is below 100 μV/s e.g. around time 1500, a straight line between the surrounding dark currents is equally good. In the lower panel the residues are plotted in black, the weights of the points in green (scale on the right). There are some systematic effects, but most of the high noise at high flux has to do with the fact that the measured spectrum is fluctuating (or fringing) fiercely which cannot be properly followed during the rebinning. In red in the lower panel (to be read on the red scale) is a Monte-Carlo estimate of the error in the memory model.

Time dependence.

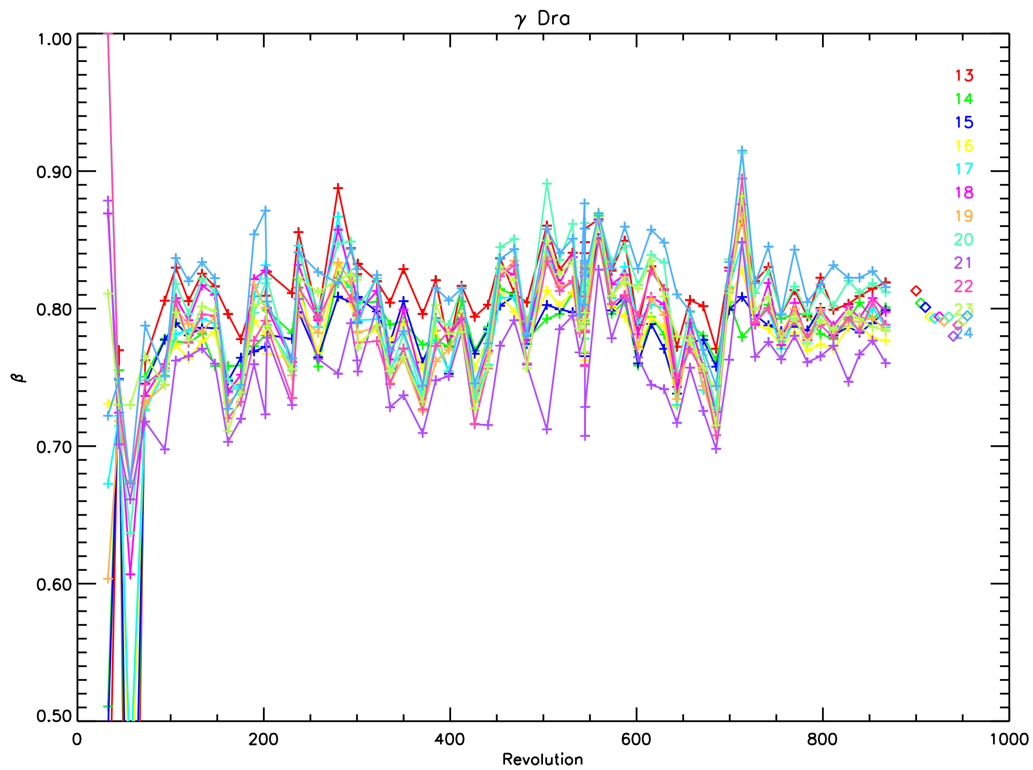

Figure 4.3: The constant β is displayed versus revolution number for the various SWS detectors involved in band 2 measurements. Revolution number is equivalent to days since launch.

We have exercised the scheme on 65 observations of γDra, as we said one of our calibration sources, taken at regular intervals during the mission. The flux of γDra is about 600 μV/s, exactly in the proper dynamic range. We determined the parameters, especially β and Λ, to see whether there is some time dependence for them. We found none, see figures 4.3 and 4.4. The values jump somewhat up and down, but further experiments showed that the memory effects do not depend strongly on the exact values of β and Λ. There seems to be some leeway to be made up by the other parameters which are history dependent anyway. It also was found that β and Λ are somewhat correlated in the sense that a higher value for β can be compensated by a lower value for Λ. Another conclusion from these figures is that the values of β and Λ are not systematically different for the different detectors, β is 0.80 $\pm$ 0.02 and Λ is 65 $\pm$5 V^{-1}. Note that β is dimensionless but Λ is expressed in inverse Volts.

Flux dependence

After eliminating the time dependence in both constants we checked whether there might be some flux dependence. For all AOT1 observations we selected those with a median flux in apertures 2 and 3 larger than 100 μV/s. As already stated before, we need some flux to establish the values

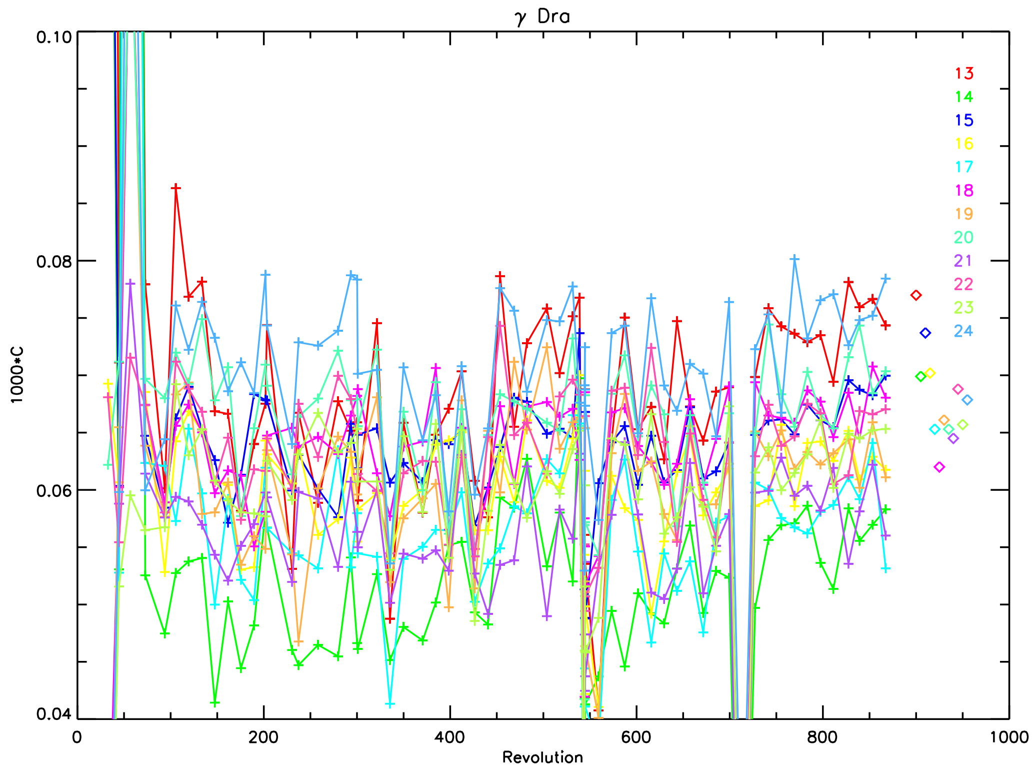

Figure 4.4: The constant C (=1000Λ) is displayed versus revolution number for the various SWS detectors involved in band 2 measurements.

for the constants. A few hundred observations were selected with a median flux ranging from 100 μV/s to $10^5\mu$V/s.

For β we do not find any significant dependency on the flux level. In figure 4.5 the histogram of the β-values derived at different flux levels is displayed. All detectors are taken into account. In black the histogram of all β-values is plotted, the other colors are the values at increasing flux levels. In the inset the median of β is displayed versus the average flux level. The colors in the inset correspond to those in the histograms. The horizontal line in the inset is the overall median for β. From this picture we conclude that there is no dependency of β on the flux level.

For Λ we come to a somewhat different conclusion. In figure 4.6 we show in a similar way as in figure 4.5 the histogram of the Λ-value. Here we see that the value for Λ decreases with increasing flux levels. Although the trend is quite clear, the error bars remain large. Moreover this kind of behaviour has no place in the present Fouks-Schubert model. That is why we ignore the trend for the time being. Maybe in a later extension of the model it will find a natural place.

Temperature dependence.

In the paper of Fouks and Schubert (1995) there is an extension for the model described above which deals with temperature variations in the detector material. SWS had a temperature sensor on the band 2 detector array. So we decided to investigate whether temperature changes had any influence on the transients. But first we had to rewrite the original formula somewhat to accommodate the specific SWS requirements. We derived the following expression to replace equation 4.2 (see appendix A for the derivation).

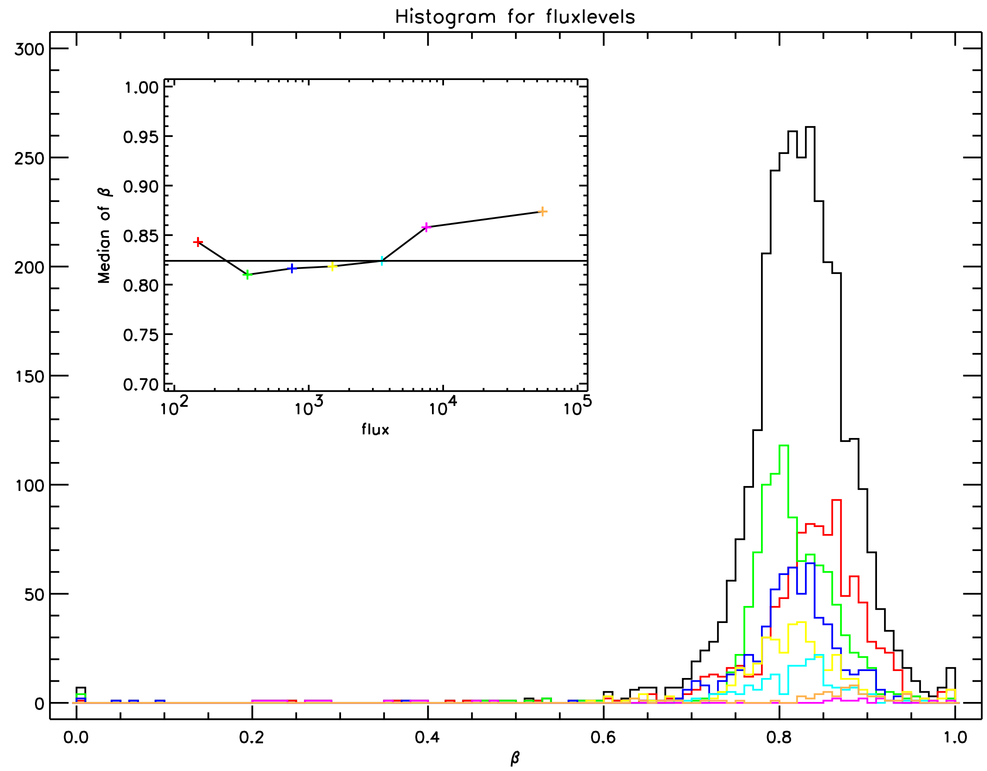

Figure 4.5: Histogram of the value of β for different flux levels. In the inset the median of β for the different flux levels is displayed.

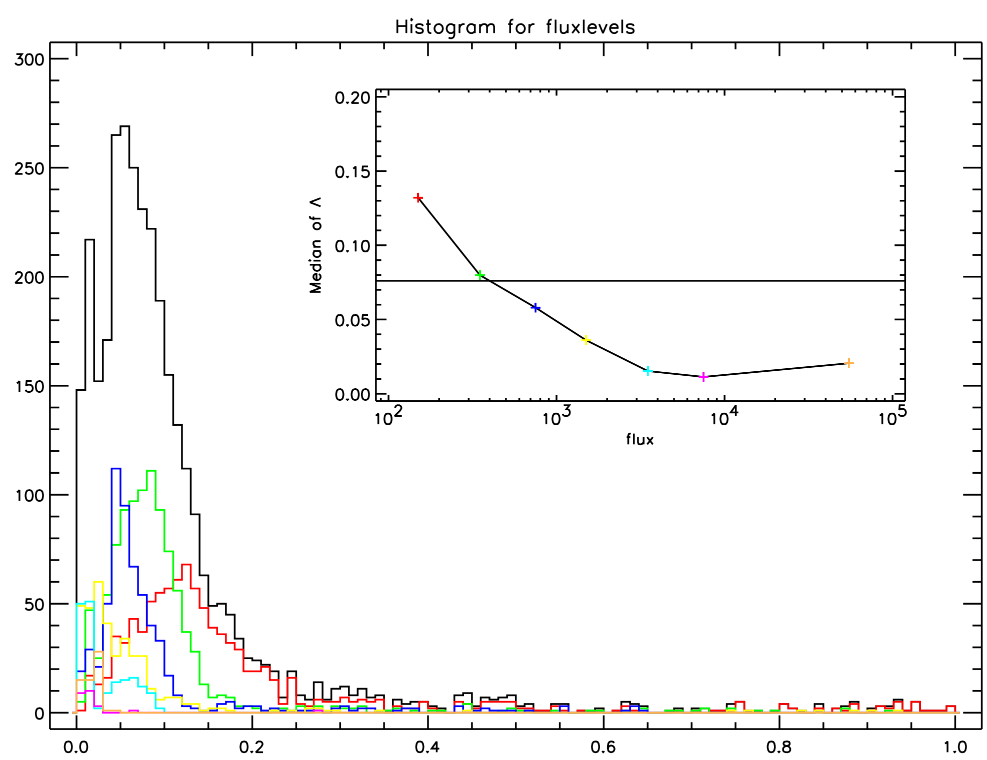

Figure 4.6: Histogram of the value of Λ for different flux levels. In the inset the median of Λ for the different flux levels is displayed.

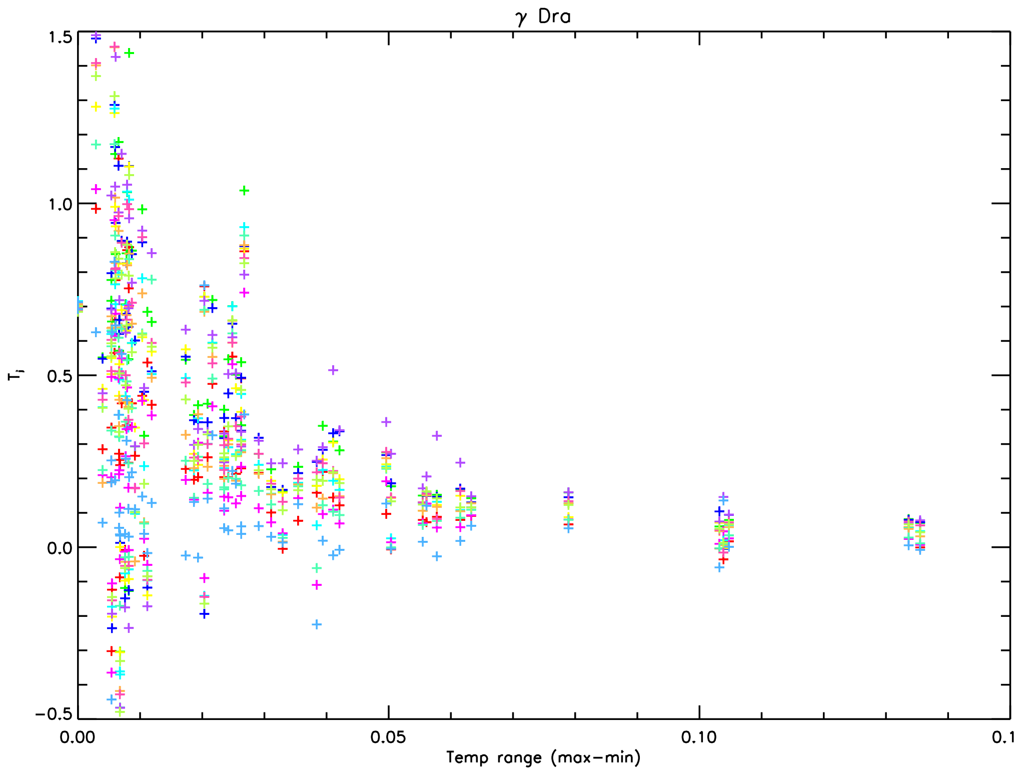

Figure 4.7: The *inverse* of T_j (wrongly labeled as T_j itself) is shown versus the range in temperature found in each of the γDra observations.

$$a_n = \frac{(1-\beta)\alpha_{n-1}F_n}{\alpha_{n-1} - (\alpha_{n-1} - (1-\beta)F_n \exp[-\Delta T_n/T_j]) \exp(-\beta\Lambda\Delta t F_n)} \tag{4.9}$$

The only change is an extra factor $\exp[-\Delta T_n/T_j]$ in the denominator, where T_j is a new constant to be determined. We derived this constant using the 60 observations of γDra. The result is shown in figure 4.7, where the *inverse* of T_j (wrongly labeled) is shown as a function of the range in temperatures found in the particular observation. In observations where the temperature is very constant there is not much information to be derived for T_j. Indeed we find that the values are fanning out toward the left hand of figure 4.7. For the few observation where there is some real variation in temperature (still not very much: 0.1K), we see that the constant goes to zero. The exponential term reduces to 1, eliminating its effect. So we conclude that we either have no effect at all or we cannot derive it from our γDra observations.

Values for β and Λ.

The values of β and Λ we finally adapted for the pipeline are the same for all detectors and very near the optimal values for γDra. We have taken a somewhat higher value for β because the value of 0.80 is on the lower edge for all other observations. And for Λ we took a slightly lower value, to better accommodate the higher fluxes. So we ended up with β =0.82 and $\Lambda = 63$ V^{-1}. Using these values we implemented a pipeline procedure called DYNADARK to replace for band 2 only, the procedures ANTIMEM and DARK.

4.2.2 Memory effects in band 4 data

Up to now, no efficient model has been found for band 4 data. Fouks-Schubert method simply does not work in this type of detectors, as we have already mentioned. Efforts are, however, still on-going trying to find an alternative method.

4.2.3 Memory effects in the Fabry-Pérot bands

The consequences of transients on the Fabry-Pérot bands (FP in Table 2.1) appear at the present time limited.

4.2.4 The 'Pulse-shape' correction

In some cases, when the memory effect correction is applied to SWS band 2 data, small detector jumps are detected that can hardly be noticed at SPD level (see below).

The so-called SWS 'pulse shapes' are small detector voltage jumps visible at SPD level which affect the calibration of SWS spectra leading to flux shifts of up to 10 Jy in the worst cases.

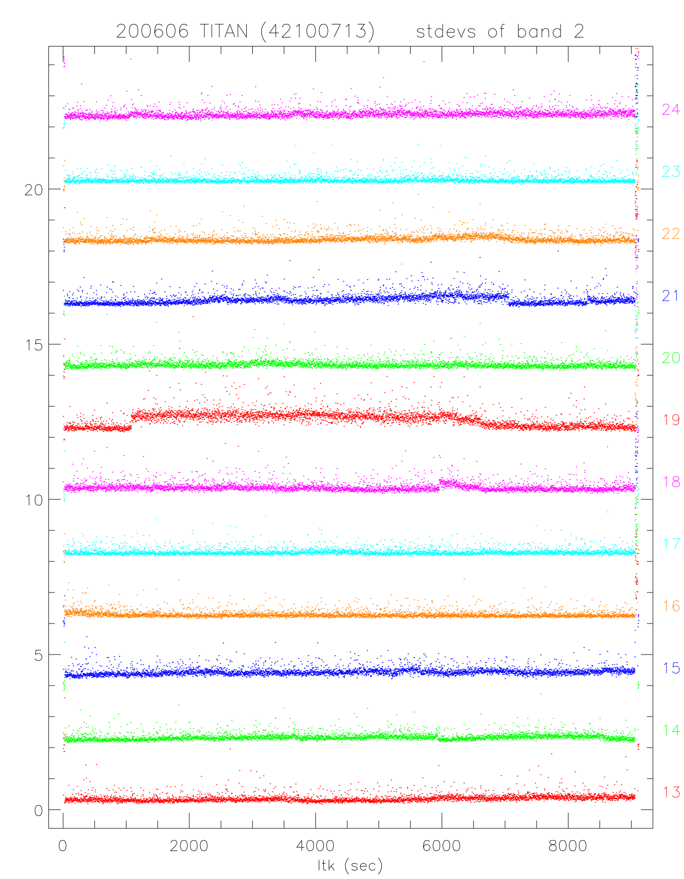

Figure 4.8: *Example of pulse shapes detected in the SWS spectrum of Titan at SPD level.*

They occur in only one detector at a time and can be generally described as a sudden decrease or increase of the signal, which then remains constant or has a long recovering time (>> 10 s) after the jump. These jumps are normally seen at low signal levels and there are typically a few of them per hour randomly distributed in time (see Figure 4.8).

There are indications of a relation between the signal jumps and a residual after reset pulse effect. A tool has been developed by Fred Lahuis and implemented in OLP version 9.5 which corrects for these voltage jumps by adjusting a baseline to the affected portion of data which remove almost completely the effect on the calibrated spectra. As a byproduct, the tool also corrects for glitches since they have a similar effect on the signal. This way most of the detector jumps are removed with very high efficiency (although not all and not always up to the 100% level).

For a more detailed description of the problem the document *"Pulse-shape Correction"* by Fred Lahuis is available at:

`http://sws.ster.kuleuven.ac.be/documents/PULSE_SHAPES/pulse-shape.ps`

4.3 Results achieved

4.3.1 Adapted Fouks-Schubert method applied to band 2 data

We would like to know what the effects are of the memory model on the quality of the data, what are the flux levels for which the model produces valid results, how much better are these results with respect to the old DARK-subtraction and whether are there flux levels where it might produce worse results.

Here we want to report on three tests of the model as implemented in DYNADARK. First we want to compare two observations of K3-50 taken at different speeds, one 4 times faster than the other. As transients take their effect in the time domain, these two observations are very different, but after correction for memory effects they should become virtually the same. The second test is on the border ratios between AOT-bands 1E - 2A, 2A - 2B, 2B - 2C and 2C - 3A for different flux levels. They should generally be equal to 1. The last test tries to establish the effectiveness of DYNADARK compared with the old DARK.

Application to K3−50

For the compact HII region K3-50 we have two full spectrum observations, an AOT1 speed 2 and a four times as long AOT1 speed 4. As memory effects live in the time domain, and not in the spectral domain, the measured signal is quite different. In the past, standard pipeline processing did not address memory effects. So the resulting spectra were quite different. Figure 4.9 displays the spectrum derived from version 8.4 of the pipeline for detector 24 only, the up and the down scan of both AOTs. The AOT1 speed 2 is generally below the speed 4 points. Also the up and the down scans are not on the same level, more so in the speed 2 than in the speed 4. The speed 4 has had more time to relax to the final signal levels. In figure 4.10 the memory model has been applied. Now both AOTs give the same final spectrum. The up and the down legs also overlap much better.

The other processing steps, after application of the memory model, were exactly the same as in the standard pipeline version 8.4. This is not as it should be in version 10 of the pipeline (not yet released at the moment of writing this report). It can be seen that the total flux goes down when applying the memory model. This is because new flux calibration tables need to be derived yet for OLP version 10. Small effects of this can be seen at the band edges. They do not line up completely.

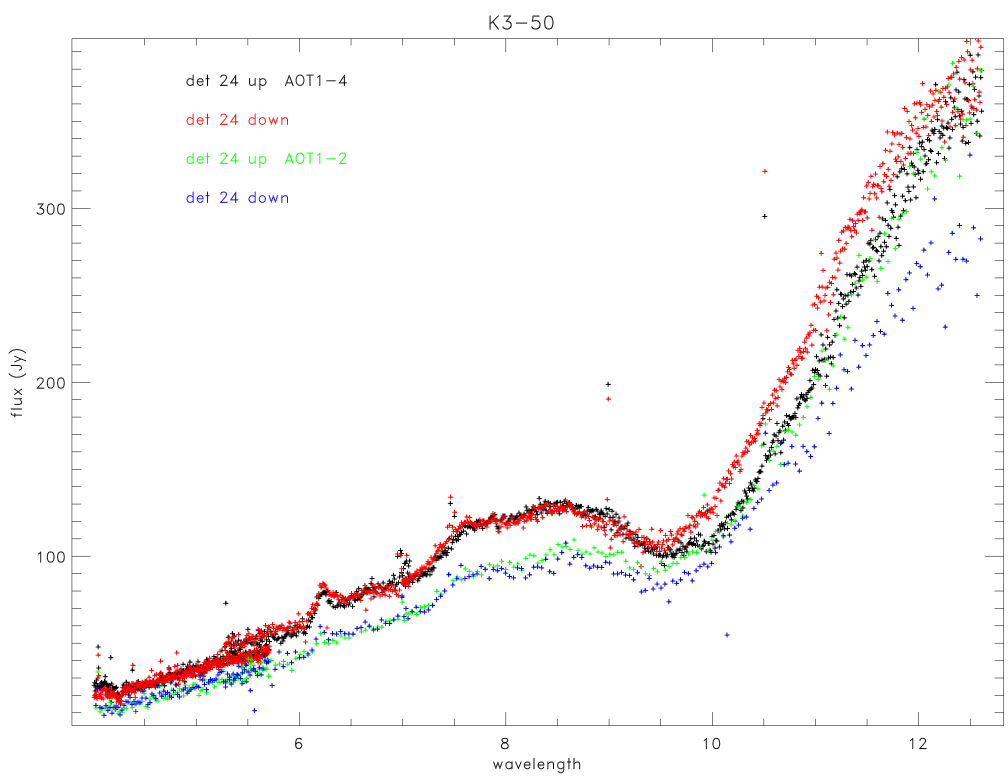

Figure 4.9: The K3-50 spectrum as processed with the standard pipeline version 8.4. Only detector #24 is displayed. The up and down scans are different and the measurements with different speeds give different results.

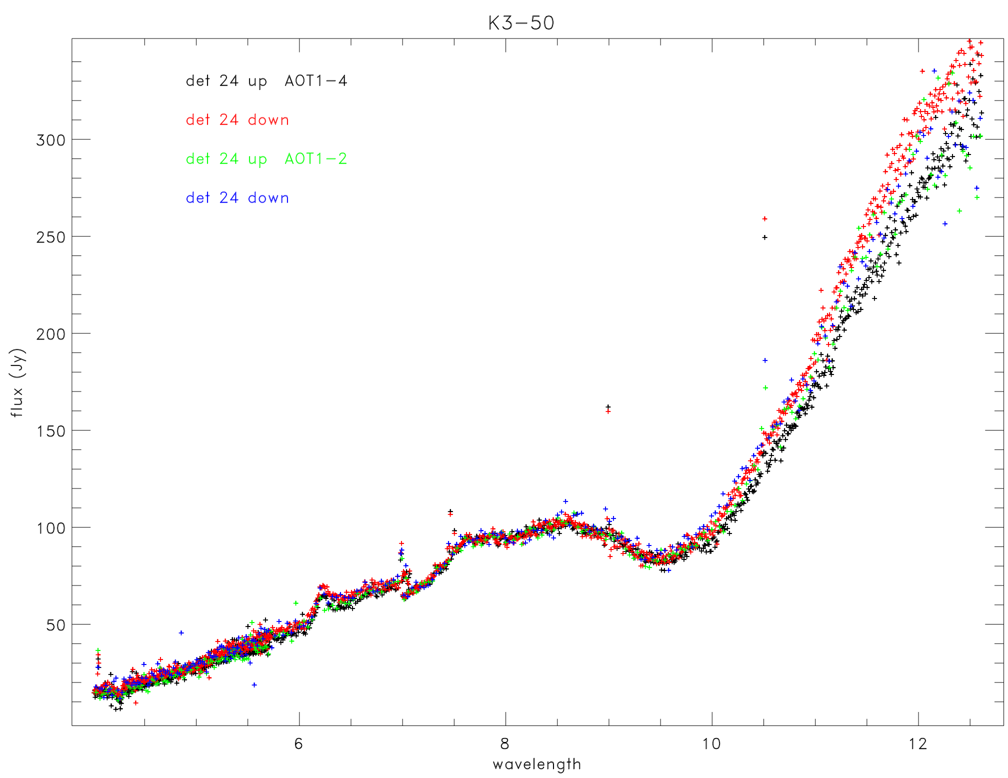

Figure 4.10: The K3-50 spectrum as processed using the memory model. Only detector #24 is displayed. The AOT1 speed 2 and the AOT1 speed 4 overlap. Note that the formal end of band 2 is at 12 μm. Band 3 starts there.

Note also the discrepancy in the black crosses after 10 μm. This is one of the so-called detector jumps mentioned in Section 4.2.4 (Kester 2000). It can hardly be noticed in the SPD as it is masked by the flux of the source itself. But here we can clearly see it. The memory model is so good that these other effects stick out like a sore finger.

Band-Border ratios.

The SWS instrument divides its full wavelength range (2.4 - 45 μm) into several so-called AOT bands. These AOT bands are defined by the detector array in use, by the aperture and by the grating order. They cover the full range piecewise. At the borders, two adjacent AOT bands briefly overlap. At the overlap, the same flux is seen in both AOT bands. Consequently, we should also measure the same amount of flux in the overlap region.

The Si:Ga detectors of band 2 are used in 3 AOT bands, 2A, 2B and 2C. There are 4 overlap regions: 1E-2A, 2A-2B, 2B-2C and 2C-3A. For all AOT1s which cover the complete spectrum, we measured the flux in the overlap region in both AOT bands and composed a band border (BB) ratio: (BB1 - BB2) / average. Ideally the BB ratios should be zero. In figures 4.11, 4.12, 4.13 and 4.14 the band border ratios are displayed versus the flux in the border region. The observations used in these plots were fully calibrated, using DYNADARK. In red in each of these figures the ratio is plotted, averaged over logarithmic bins, plus error bars.

There is a remarkable trend in all 4 figures at the low flux end. All ratios dip to -2 for low fluxes. There seems to be a bias in the *second* border, i.e. the high wavelength AOT band. We are not certain what is causing this trend. In other similar figures of other band border ratios which are not shown here, the trend can be to +2. But there is always this trend at low flux levels. It could have something to do with the way all measurements are taken. The up-down observing strategy is such that the scan starts and ends at the low wavelength border while it reverses scan direction at the high wavelength border. The starting point and the end point are (more) near to a dark current measurement than the midpoint. Whether and how this can cause this trend is unclear. Maybe at low fluxes it is *always* the case that one AOT band reaches zero before the other band. One last remark about the trend: It has nothing to do with DYNADARK, it is also present in similar plots made with DARK, although due to the wider noise it is somewhat harder to see.

At the medium and high flux levels the band border ratios we see that the results are within 10 %. Sometimes e.g. in figure 4.11 there seems to be increasing trend, pointing to some remaining non-linearity in some of the detectors.

Effectiveness.

To evaluate the effectiveness of DYNADARK we would like to have observations where we know beforehand what we are seeing, so we can determine how good the memory correction performs. Obviously almost all observations of true spectra do not fit this bill, we do not know what the spectrum should look like. However, there are a number of observations where the observer was only interested in the long wavelength (LW) section of the spectrum or in the Fabry-Pérot mode, and forgot to do some serendipitous survey in the short wavelength (SW) section. In these observations the SW scanner was actually standing still and the light falling on the detector was whatever was coming through at the particular grating setting. Essentially SWS was acting as a photometer. In these observations, although we still do not know what the flux level was exactly, we at least know that it should be *constant*.

We found over 100 of these observations, mostly AOT7's and some AOT2's. They contain one or more grating settings each lasting typically 100 to 200 seconds. There might be several settings on the same grating position separated by dark measurements.

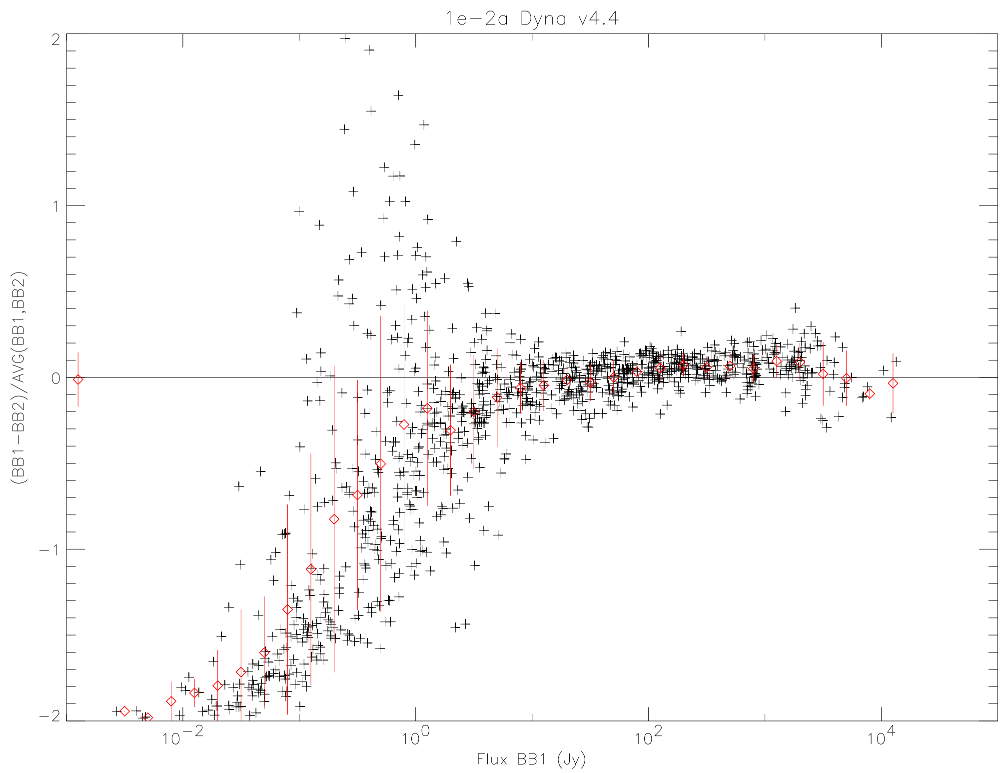

Figure 4.11: Band border ratio for 1E-2A.

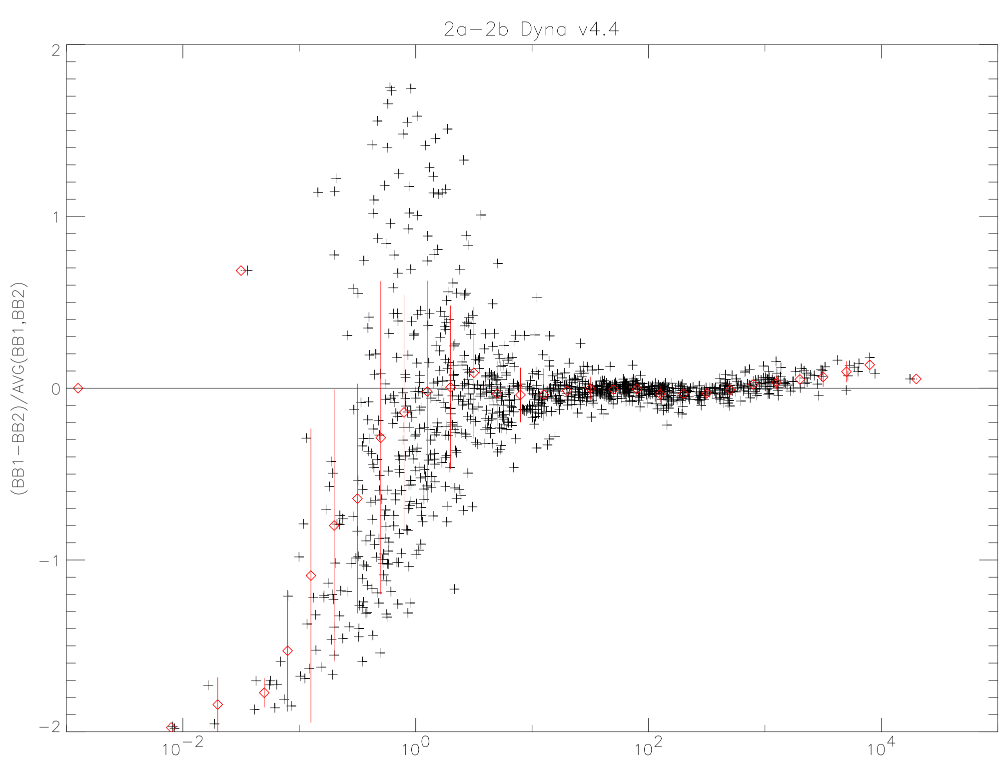

Figure 4.12: Band border ratio for 2A-2B.

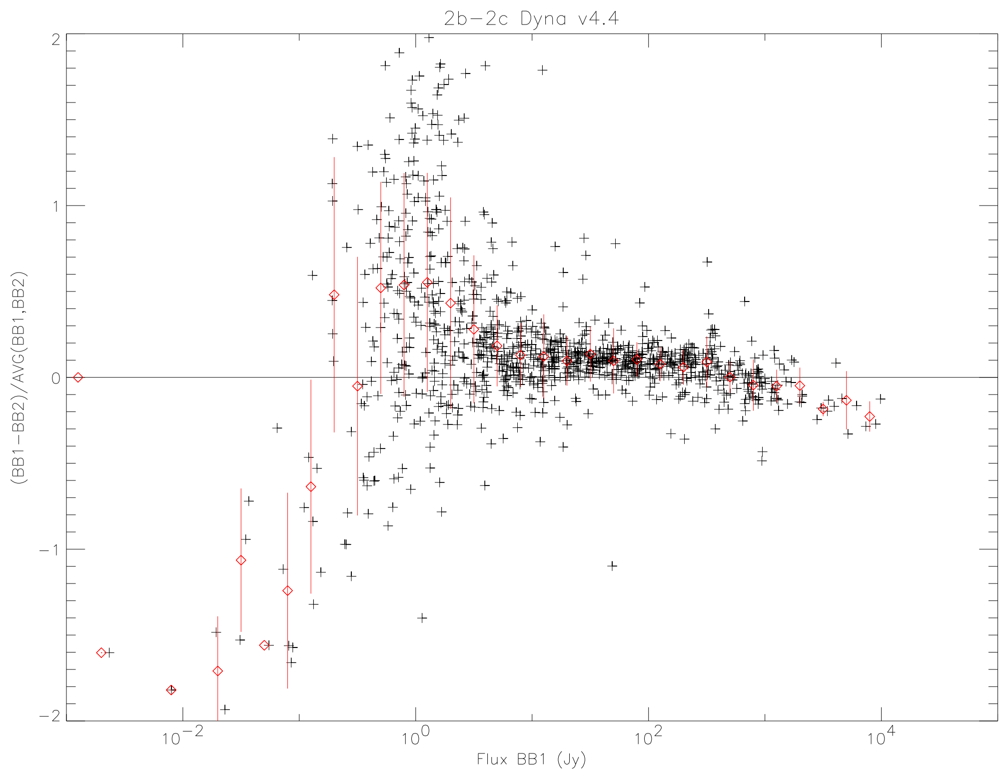

Figure 4.13: Band border ratio for 2B-2C.

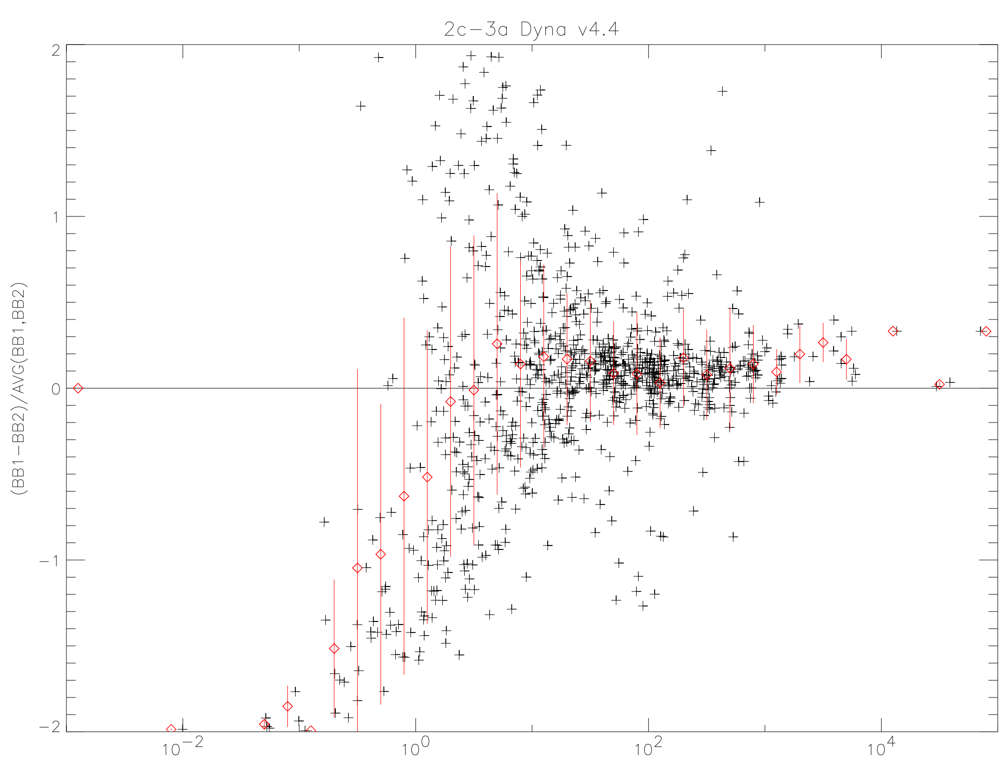

Figure 4.14: Band border ratio for 2C-3A.

We ran them through DARK and through DYNADARK. In DYNADARK we set the no-run-flag weight to one and the resolution to 400. In these observations the run-flag is not set at all as they were not meant to be valid observations. We want to treat them as normal, with normal weights. So we had to reset the no-run-flag weight (nrfwgt=1). The resolution is needed only to get an estimate of the incoming flux. It was set to 400 and not to the default which is automatic. The automatic calculation assumes that we are scanning so that the same wavelength is seen by all detectors at a certain moment. Here that is not the case. The scanner is standing still. There is no overlap. So the automatic calculation fails. We have to set it ourselves. At a resolution of 400 each detector is averaged individually.

For most observations with a flux in band 2 of the order of a few hundred or higher, DYNADARK reported "det dd, model is not optimal." and/or "20 cycles without complete convergence." From discussions with Boris Fouks, indeed the originator of the Fouks-Schubert model which DYNADARK implements, we already knew that these particular kind of observations are not very well suited for the rather simple Fouks-Schubert model. In deriving this model from a much more complicated set of coupled differential equations, a term was ignored which contains the logarithm of the flux step. Mostly this flux step is small indeed, especially when scanning over a spectrum. In these observations we have a (large) flux step at the begin of every grating setting. So the Fouks-Schubert model is not completely optimal for these kind of observations. In normal observations of true spectra we can expect to perform better. Still, even though we are working with a suboptimal model, we will see how it is performing.

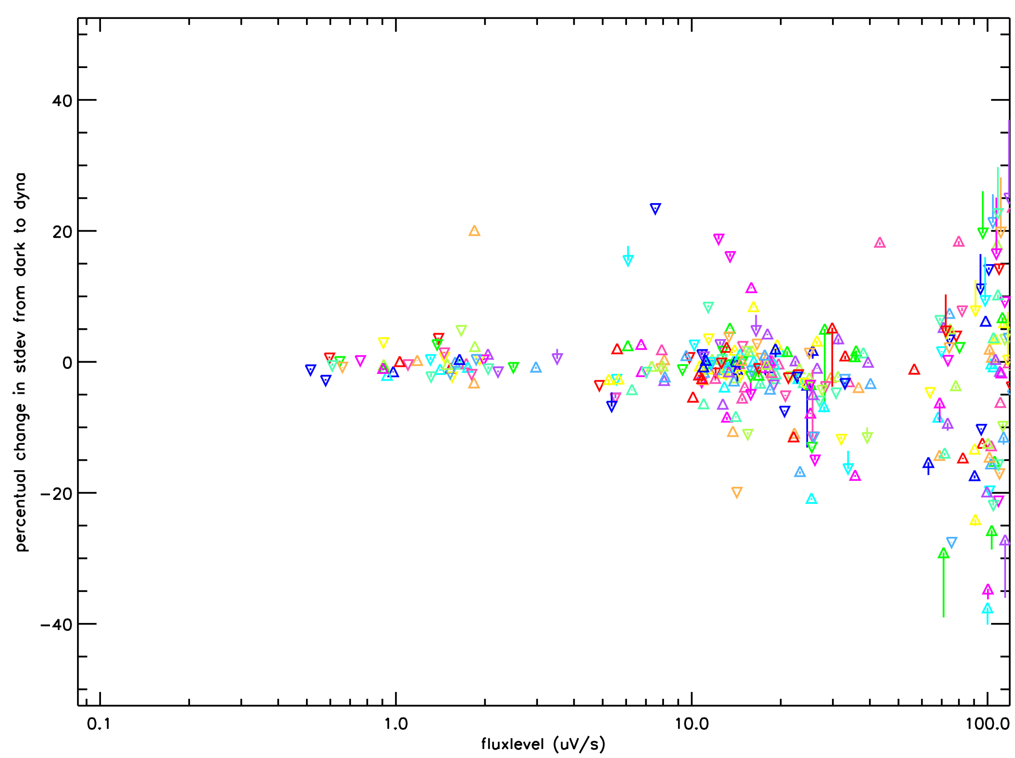

Figure 4.15: The percentual change in standard deviation versus flux level at the lower flux end. Different colors indicate different detectors.

For both the DARK-subtracted SPD and the DYNADARKed one we calculated the mean per detector and per grating setting in band 2. Multiple grating setting to the same value were averaged together. And we calculated the standard deviations pertaining to all of them. Now, the DARK-mean might be different from the DYNA-mean and it is unclear which one (if any) is the right one, but they should be constant. Constancy is a necessary condition, not a sufficient one. So a measure of the quality of the model is the standard deviation. If the standard deviation of one model is less than the other, the former model is better.

Let us now try to define a 'best' model as one that follows the global transient evolution, but not the noise. Because we would like to know how much of the standard deviation we found, is intrinsic noise and how much is systematic, due to imperfect models. As we are only interested in the noise, we differentiate the signal: $F_k - F_{k-1}$. Similarly as above we determine the average (very much zero) and the standard deviation. This standard deviation is our best possible result with respect to which we will draw our conclusions. As this standard deviation is the result of a difference of two (Gaussian?) errors, we divide it by the square root of 2. Note also that by differentiating the flux we got another noise realization than in the original. So the 'best' stdev need not necessarily be the smallest, it might fluctuate somewhat. (TBD a number here)

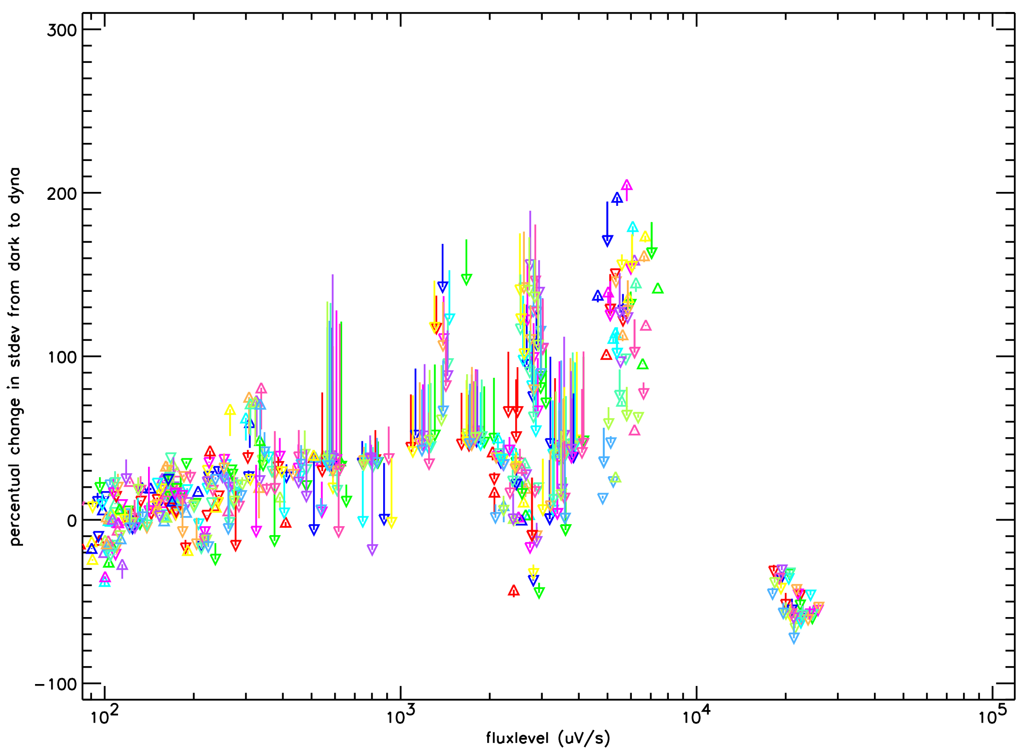

Figure 4.16: The percentual change in standard deviation versus flux level at the higher flux end.

For both DARK and DYNADARK we calculated the percentual difference in the stdev to the best as

$$100 \times (\sigma_{dark} - \sigma_{best})/\sigma_{best}.$$

We plotted the DARK and the DYNADARK difference for each detector and grating position as a function of average flux. The DARK and DYNADARK points are connected by an arrow pointing in the DYNADARK direction in figures 4.15 and 4.16.

At the lower flux levels not much is happening, even the standard deviations are very similar, to each other and to the 'best' model. At around 100 μV/s the effects of the transients are setting in.

Most of the arrows point down, implying that DYNADARK produces more consistent, more constant results than DARK.

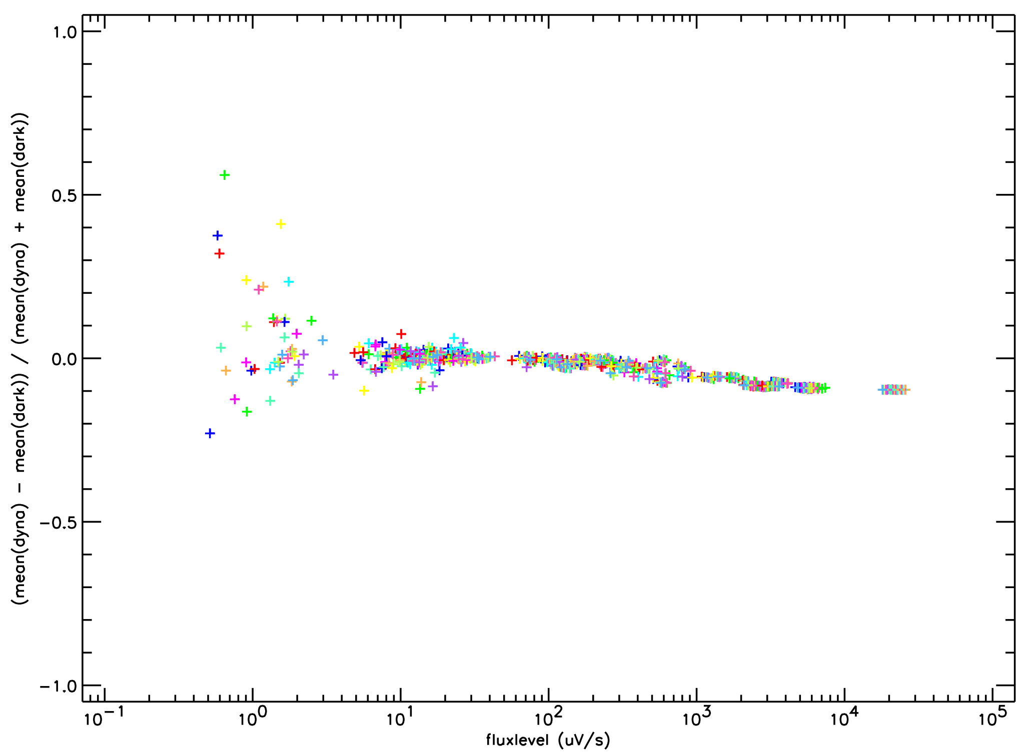

Figure 4.17: The relative difference in flux between DYNA and DARK as a function of flux level.

In figure 4.17 the relative difference between DYNADARK and DARK is displayed as a function of flux level. At low flux levels we see a fanning out due to the low flux itself. Then from a few μV/s to about 100 μV/s the difference is zero, indicating that DYNADARK and DARK are actually doing the same. And from 100 μV/s onward we see that DYNADARK is lower, decreasing to 90 % of the values DARK reaches. We display here raw, uncalibrated data and this discrepancy is caused by the fact that α_k 'eats' more into the data than DARK. In the final calibrated result the difference is compensated by a larger multiplication factor.

4.4 Implementation in OSIA/pipeline

As of version 10 of the SWS pipeline, band 2 SWS data is corrected for memory effects using this adapted Fouks-Schubert method.

Electrical glitches and saturation above a given level became the new limiting factors. As below this saturation level the Fouks 1-D model is good enough to describe any flux change, it is under investigation that this saturation is coming from cross-talk between pixels, change of the illumination profile on the detector surface (point source problem) or it is a true saturation problem.

As already mentioned, the 'pulse-shape' correction tool was implemented in OLP v9.5.

Chapter 5

Transient effects in CAM data

5.1 Impact on CAM detectors

In general, transients are the dominant error source in CAM images.

The SW CAM CID In:Sb 32×32 matrix array is affected by transient effects without instantaneous jump ($\beta = 0$). This is, there is some time lag when responding to a flux variation. This default, which is not well understood (in particular, it does not correspond to a simple time constant) must be corrected for during data processing. A general description of transients in ISOCAM SW detectors can be found in Tiphène et al. (1988). In the case of the SW detectors long term transient effects are not a real concern, as shown by the CAM daily calibration measurements (Boulade & Gallais 2000), and will not be considered here.

Severe transients are also observed in LW CAM detectors (Si:Ga based). A general description of transients in ISOCAM LW detectors can be found in Coulais & Abergel (2000). They show that, for uniform (low gradient) illumination, the Fouks-Schubert model allows us to describe the LW response to upward and downward steps of flux with an accuracy of better than 1%. This is a factor of 10 better than than the accuracy obtained in the past with empirical inversion methods (see Section 5.2.4 below). For each pixel, only two parameters have to be used, which are found to be constant over the whole life of ISO. However, the approach is not valid for non-uniform (high gradient) illumination, which is typically the case of point sources. The correction is very good for low contrast illumination (extended sources and/or faint sources over a high background).

Most of the CVF observations are usually performed after a discrete filter observation, thus implying a large decrease in the incident flux on the detector. This can introduce important transient effects that last several readouts and hence several wavelength steps which are not yet corrected for in the pipeline. The result is a larger than true flux for the first wavelength steps. We also know that transients are more important for weak sources than for bright sources.

In LW CAM detectors, a slow and continuous increase in the response is observed quite frequently after a positive flux step. This rise is gradually attenuating on a variable time scale which can be up to several hours and seems to be smaller for small flux steps. Unlike the short term transient, no analytical or physical description has been developed to correct for this specific effect, which seems to be a general behaviour of this type of detector (Vinokurov & Fouks 1991). The temporal evolution of the detector response (see Fig. 5.1), although globally rising, show also oscillations with typical amplitudes of about 5% of the total sky emission. This is an additional limitation when observing faint extended emission structures with contrasts smaller than a few percent of the zodiacal light.

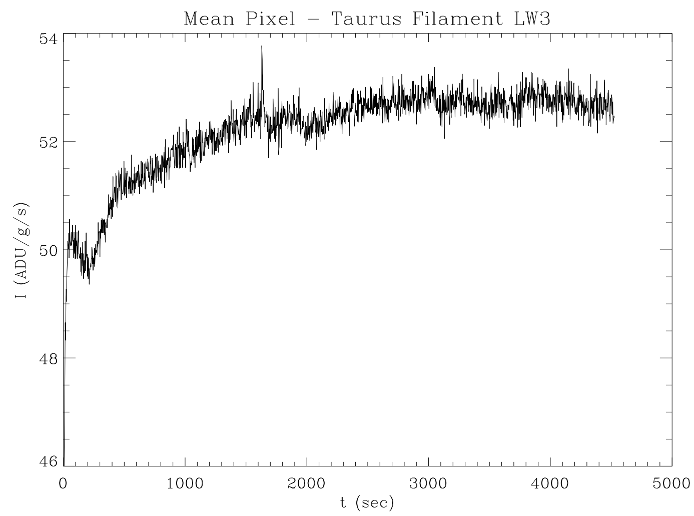

Figure 5.1: *Mean temporal evolution of the flux observed by one of the ISOCAM LW detectors (LW3) on a faint extended emission field in Taurus. Note the long term drift and the small amplitude oscilations up to the 5% level.*

5.2 Efforts developed to correct CAM data for transient effects

5.2.1 Transient effects in SW detectors

Despite its original technology (CID = Charge Injection Device), which makes it unique among the ISO detectors, this array is affected by transient effects appearing as a time lag when responding to flux variations. The time evolution of the signal has no simple behaviour that could be easily predicted, in which case a straightforward correction algorithm could be applied during data processing, at least to approximate the asymptotic stabilized level. One clear property of the CAM-SW transient effects is the dependence of the stabilization time scale on the current level of charges stored in the considered pixel: the lower the charge, the longer the stabilization time. Prompted by this clue, a phenomenologic approach was developed finding that a general model of this effect gives a fairly good approximation in most cases. It allows in particular to build 'asymptotic' images with, a priori, a better relative photometry between pixels.

Figs. 5.2 and 5.3 show the transient effect in two cases: (i) a small step of flux starting practically from dark and to which corresponds a slowly increasing signal and (ii) a steep decrease after a hit by a particle (glitch). The behaviour of the signal depends esentially on the value of two parameters: the charge at the beginning and the step of charge; any situation where these two parameters are identical will produce the same evolution of the signal with the number of exposure. This last point is important: we must speak of number of exposures rather than of time, since the behaviour is only dependent on the number of exposures and on the charge at that exposure, not on the actual duration of the observation. A consequence of this is that the best strategy when observing with ISO at very low fluxes was in general to choose a longer integration time rather than a large number of exposures for a given duration of the observation.

In addition, to overcome this problem, it was found that good results were obtained by a pre-flash of the array done with the internal calibration device at the beginning of the observations. The astronomical sources are then observed during the slow decay of the array after the pre-flash.

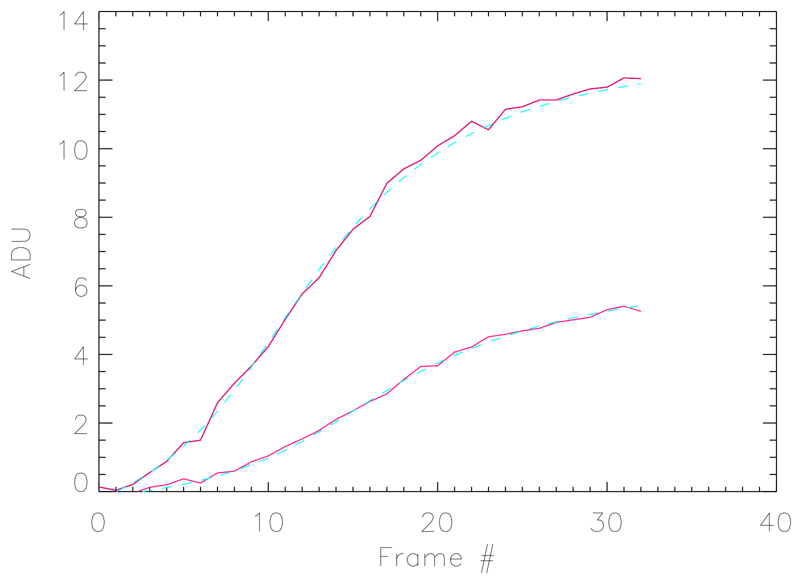

Figure 5.2: *Two examples of the evolution of the signal on two pixels after a flux step (of different magnitude for each pixel). Solid line: evolution of the signal (in ADUs) of two given pixels subjected to a positive but small flux step. The transient effect (no stabilization) is clear. Dashed line: fit of the signal by the model. X-axis units correspond to the image number in the sequence; the Y-axis unit is ADUs*

In a second step, we reproduced the same flash and slow decay, while the entrance wheel of the camera is closed. Subtraction of the reference decay permits to reveal the faint sources. The pre-flashing procedure reproduces the flash with a few percent accuracy and allows to detect sources in the mJy range, within 20 minutes of observing time, while a normal observation would have required several hours due to the slow stabilization.

Modelling

Although models for the correction of the transient effect in CAM-LW detectors have been succesfully developed (see next subsection), they were not able to simulate the very specific behaviour of CAM-SW detectors. Several attempts were made to model this behaviour using combinations of exponential functions with different time constants, but none of them were successful: this is not unexpected since, as previously said, the characteristic time is itself dependent on the level of charges. We then allowed the time constant to vary according to some function of the instantaneous value of the charge in the pixel. Then it was found that a universal law was able to reproduce quite well almost any situation. The parameters of this law must be tuned for each pixel to have a precise fitting, but there is rather low dispersion among those values as long as the pixels follow the same history. The law is such that the temporal evolution is the same as the charge or discharge of a capacitor where the time constant would be inversely proportional to the charge. In other words, the charge $s(n)$ of a pixel after exposure n is the solution of the functional equation:

$$s(n) = s_F + (s_I - s_F)exp[-ns(n)/s_0] \tag{5.1}$$

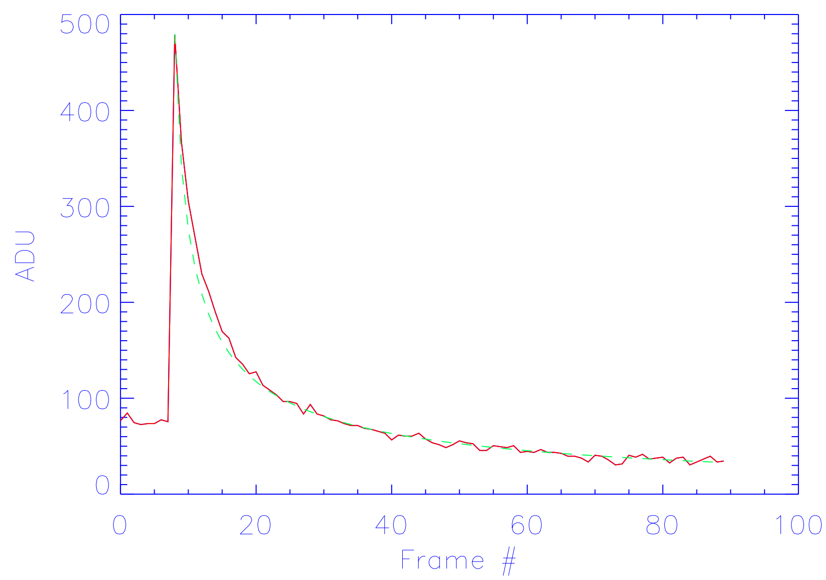

Figure 5.3: *Solid line: same as Fig. 5.2 but in the case where a particle hits the pixel during the exposure: here, the signal decreases after the hit. Dashed line: the fit of the signal by the model*

where s_F is the charge when full stabilization is reached (could be extremely long), s_I is the charge at the beginning of the set of exposures and s_0 is a constant with dimensions of a charge. One has to solve this equation in $s(n)$ for each pixel. This is done by standard math routines (for instance *Newton* with IDL). Figs. 5.2 and 5.3 show the fit of the actual signal obtained through the solution of this equation when parameters s_I, s_F and s_0 are properly adjusted: in most cases the fit is very good. Once this solution is obtained, it is then possible to derive the asymptotic value s_F which must correspond to the stabilized value of the signal. Some care however must be taken in the interpretation of this asymptotic value at very low flux levels, since the uncertainty becomes higher: the signal evolution is practically a noisy straight line and cannot provide a good enough constraint to the model. A self-consistent package of IDL functions has been developed at the Observatoire de Paris-Meudon (Tiphène et al. 2000) in order to optimize the processing of a complete cube of images. Unfortunately, it was never implemented in the CAM Interactive Analysis Software (CIA), nor in the CAM pipeline.

A detailed physical explanation for the modelled behaviour of the detector has not been established but it is believed that the correlation found between the 'time constant' and the charge is likely related to the surface traps in the semiconductor (InSb): those traps have to be filled first with the photo-charges before the well begins to actually store free charges. When examining the trend at low signal, one finds that the amount of trapped charges should be of the order of s_0, i.e. typically 70,000 electrons. In terms of trap surface density this corresponds to 7 10^8 e^-cm^{-2}, a realistic figure for this type of detector (Tiphène, 1987).

5.2.2 Transient effects in LW detectors

Under quasi uniform illumination (low gradient of illumination on the pixel surface and between adjacent pixels), the transients of CAM-LW matrix array have several properties (Pérault et al. 1994; Abergel et al. 2000; Coulais & Abergel 2000):

- an instantaneous jump of the current after a flux change, of ~50% of the new steady state current;
- a time constant inversely proportional to the incoming flux;
- the transients are non linear (see Fig. 9 in Pérault et al. 1994);
- they are highly reproducible when the pre-history is the same;
- they strongly depend on the pre-history (see Fig. 6 in Coulais & Abergel 2000);
- when $J^{\infty}_{n+1}/J^{\infty}_{n} > 2.$, the upward step is characterized by an inflection point, the position of this point being related to the ratio $J^{\infty}_{n+1}/J^{\infty}_{n}$;
- downward steps are hyperbolic-like.

As a consequence, the response should be described with a non-linear and non-symmetrical model.

For a wide dynamical range, the comparison of the Fouks-Schubert model with experimental data for the CAM-LW detector has shown its high exactness. For 90% of the pixels, it is possible to adjust β and λ parameters to fit the transient response with an accuracy better than 5 % for each readout $J_n(t)$ during a block, then the accuracy on the computed value of J^{∞}_{n} is about a few percent. The parameters (β, λ) for each pixel of the matrix array have been adjusted on a limited number of data sets but, apparently, they were unchanged during the life of ISO in space (~28 months) (Coulais & Abergel 2000). The comparison of J^{∞}_{n} with steady-state calibration of the detectors allows us to estimate that the incident fluxes derived with this method have a precision better than a few %.

The worst situations ocurr in two cases: a) illuminating the array previously at dark position of the entrance wheel, or b) after a saturating flux.

The first problem could be reduced by keeping always light on the array (e.g. the ISOCAM parallel mode) and sorting the observations by decreasing fluxes. Dark calibration have been placed at the end of the observations or in those revolutions without a ISOCAM science activity in prime mode.

5.2.3 Cross-talk : the problem with point sources

Eq. (2.1) reproduces the experimental data only under homogeneous irradiation of the array. The transients for point-sources are different. This is due to 3-D effects inside the array. These effects are caused by the fact that the screening length for the charges, created in the bulk of low-background detectors under a time-variable irradiation, is very long. As a result, the field of the charges penetrates through the bulk and spreads to all sides creating a 3-D picture of the force lines of the field (Vinokurov & Fouks 1988; Fouks et al. 1994; Vinokurov et al. 1992). However, under homogeneous irradiation, the influence of the 3-D field effects on the transient current in the detector can be described with a good exactness in one dimensional (1-D) approximation with the use of the field averaged along the contact planes and with the re-normalization of the contact parameter E_j (Fouks 1997). For highly inhomogeneous irradiation such approach is impossible, and 3-D equations must be used. They are :

$$\text{the continuity equation :} \quad \nabla(p\mathbf{v}) = -\frac{p(\mathbf{r},t)}{\tau} + G\left(\mathbf{r},t\right), \tag{5.2}$$

$$\text{the Poisson equation :} \quad \nabla\mathbf{E} = \frac{4\pi e}{\kappa}\rho\left(\mathbf{r},t\right), \tag{5.3}$$

and the trap recharging equation written in the form : $$\frac{\partial \rho(\mathbf{r},t)}{\partial t} = \frac{p(\mathbf{r},t)}{\tau} - G(\mathbf{r},t). \quad (5.4)$$

Here $p(\mathbf{r},t)$ is the hole concentration, τ the capture time, $\mathbf{v}(\mathbf{r},t)$ the drift velocity of the holes, $G(\mathbf{r},t)$ the generation rate, $\rho(\mathbf{r},t)$ the density of the charge accumulated in the traps. In principle, these equations have to be supplemented by the boundary conditions describing the equipotentiality of the contacts and the absence of current through the free surfaces of detectors.

Below we will consider the simplified plane geometry case. We suppose that the detectors represent continuous photoconductive media confined by two contact planes (at $z = 0$ and $z = l$) with fixed potentials (0 and V_0). This provides the steady-state field $E_0 = V_0/l$ directed along the z-axis. The following consideration is carried out under the condition :

$$E_0 \gg E_j \quad (5.5)$$

which is always true for usual Si:Ga detectors. This permits to ignore the effect of non-stationary fields on the drift velocity and rewrite Eq. (5.2) as :

$$v\frac{\partial p(\boldsymbol{\rho},z,t)}{\partial t} = -\frac{p(\boldsymbol{\rho},z,t)}{\tau} + G(\boldsymbol{\rho},z,t), \quad (5.6)$$

where $v = \mu E_0$ and $\boldsymbol{\rho}$ is the transverse coordinate. Next we suppose that the generation is independent on the coordinate z : $G(\boldsymbol{\rho},z,t) = G(\boldsymbol{\rho},t)$. In this case the solution of Eq. (5.6) has the form :

$$p(\boldsymbol{\rho},z,t) = p(\boldsymbol{\rho},0,t)\, e^{-\frac{z}{\tau v}} + \tau G(\boldsymbol{\rho},t)\left(1 - e^{-\frac{z}{\tau v}}\right). \quad (5.7)$$

The substitution of this formula for the hole concentration in Eq. (5.4) gives the expression for the time derivative of the charge density :

$$\frac{\partial \rho(\boldsymbol{\rho},z,t)}{\partial z} = \left[\frac{p(\boldsymbol{\rho},0,t)}{\tau} - G(\boldsymbol{\rho},t)\right] e^{-\frac{z}{\tau v}}. \quad (5.8)$$

From Eq. (5.3) we can deduce the equation that links the z-field component at the contact plane $z = 0$ with the charge density in the detector bulk :

$$\frac{\partial E_z(\boldsymbol{\rho},0,t)}{\partial t} = \int d\boldsymbol{\rho}_0 \int_0^l dz_0 E_z(\boldsymbol{\rho},0,\boldsymbol{\rho}_0,z_0)\, \frac{\partial \rho(\boldsymbol{\rho}_0,z_0,t)}{\partial t}, \quad (5.9)$$

where the Green function of the Poisson equation for the used plane geometry is defined by the expression taking into account the effect of image charges :

$$E_z(\boldsymbol{\rho},0,\boldsymbol{\rho}_0,z_0) = -\frac{2e}{\kappa} \sum_{n=-\infty}^{n=\infty} \frac{(2n-1)\,l + z_0}{\left([(2n-1)\,l + z_0]^2 + (\boldsymbol{\rho} - \boldsymbol{\rho}_0)^2\right)^{3/2}}. \quad (5.10)$$

Now using the boundary condition, which has the form for the 3-D case :

$$p(\boldsymbol{\rho},0,t) = p(\boldsymbol{\rho},0,0)\, exp\left[\frac{\Delta E_z(\boldsymbol{\rho},0,t)}{E_j}\right] \quad (5.11)$$

(here $\Delta E_z(\boldsymbol{\rho},0,t)$ is the non-stationary z-component of the field in the contact plane) and, from Eqs. (5.8) and (5.9), one obtains the integral-differential equation for this field component :

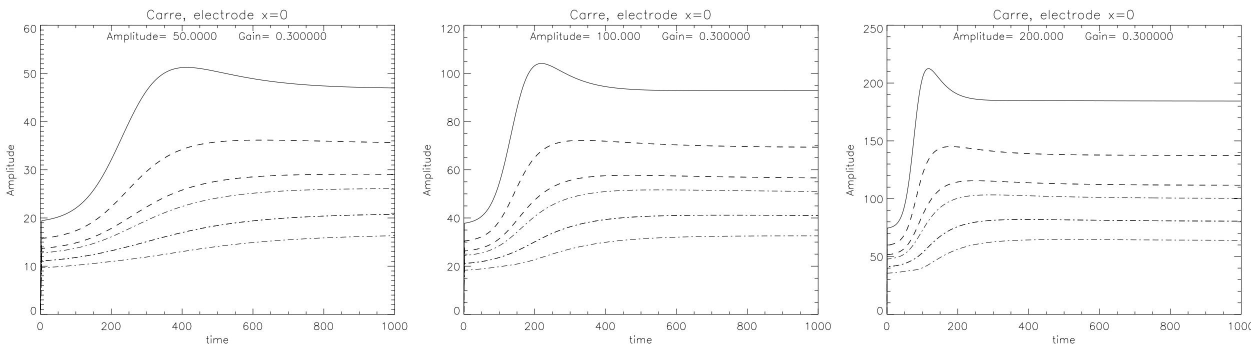

Figure 5.4: Three transient responses for the same point spread function profile with three different amplitudes. The source is off-centered by (1/4,1/4) of pixel size. The continuous line shows the transient response for the central pixel, the dashed lines are for the the 4 adjacent pixels (only 2 lines because of symmetry) and the dot-dashed lines are for the diagonal pixels (3 lines). The computed results illustrate the current spreading (the appearance of the current in dark regions neighboring to the illuminated ones) that results from the spreading of field lines and the current overshooting that results from a high current density in the region under a high-density flux. The presented results give rather good qualitative description of the transients under point-source illumination. In order to obtain an exact quantitative description of the transients the theory has to take into account the real topology of the detectors and their conductive surroundings.

$$\frac{\partial E_z\left(\boldsymbol{\rho},0,t\right)}{\partial t} = \int d\boldsymbol{\rho}_0 K(\boldsymbol{\rho}-\boldsymbol{\rho}_0)\left[G(\boldsymbol{\rho}_0,t) - \frac{p\left(\boldsymbol{\rho},0,0\right)}{\tau}\right] exp\left[\frac{\Delta E\left(\boldsymbol{\rho}_0,0,t\right)}{E_j}\right] \tag{5.12}$$

with the kernel described by the expression :

$$K\left(\boldsymbol{\rho}\right) = \frac{2e}{\kappa}\int_0^l dz \sum_{n=-\infty}^{n=\infty} \frac{2nl+z}{\left[\left(2nl+z\right)^2+\boldsymbol{\rho}^2\right]^{3/2}} e^{-\frac{z}{\tau v}}. \tag{5.13}$$

Under homogeneous irradiation, $G\left(\boldsymbol{\rho},t\right) = G\left(t\right)$, one can deduce from Eqs. (5.12) and (5.13) the following equation :

$$\frac{\partial E_z\left(0,t\right)}{\partial t} = \frac{4\pi\beta}{\kappa}\left[e\tau v G\left(t\right) - evp\left(0,0\right) exp\left[\frac{\Delta E\left(0,t\right)}{E_j}\right]\right], \tag{5.14}$$

where $\beta = 1-g\left(1-e^{-1/g}\right)$ and $g = \tau v/l$. This equation permits to deduce analytically Eq. (2.1) for uniform illumination (Fooks & Schubert 1995). Under inhomogeneous irradiation Eq. (5.13) - with Eq. (5.14) - has to be solved by numerical computations. The computed field distribution along the contact plane, separated into individual squared detector areas of side a with the centers $x = na$ and $y = ma$, where n and m are the whole numbers, permits to find the currents through these detectors :

$$J_{n,m} = \int_{S_{n,m}} d\boldsymbol{\rho}\left[evp\left(\boldsymbol{\rho},0,0\right) exp\left[\frac{\Delta E\left(\boldsymbol{\rho},0,t\right)}{E_j}\right] + \frac{\kappa}{4\pi}\frac{\partial E_z\left(\boldsymbol{\rho},0,t\right)}{\partial t}\right], \tag{5.15}$$

where the areas $S_{n,m}$ are restricted by the conditions : $na-\frac{a}{2} \leq x \leq na+\frac{a}{2}$, $ma-\frac{a}{2} \leq y \leq ma+\frac{a}{2}$. The computational results for different inhomogeneous fluxes and different pixels are presented in Fig. 5.4. These results are compared with real data in Section 5.3.3.

5.2.4 Application of inversion methods to CAM-LW detectors

Prior to the application of the Fouks-Schubert model to correct CAM-LW data for transient effects several inversion methods were tried. They describe the response of a detector in two phases: an instantaneous response which accounts only for a fraction of the final signal plus an exponential-like variation term for the remaining fraction. The latter term includes all the influence from the past illumination history. The flux is recovered after linearization of the equations and resolution of the system of linear equations by LU decomposition.

The simplest models use simple exponential formulae to describe the response starting from a stabilized level to a new one. However, such an approach generally fails because (1) it does not take into account the whole history of illumination and (2) observed upward and downward responses are not symmetrical.

An integral description of the response which takes into account the illumination history was later proposed by Abergel et al. (1996, 2000). This so-called *'Old IAS model'* was systematically used during a large fraction of the ISO mission, but it was still not able reproduce the asymmetry in the response curve observed between upward and downward steps, this meaning that the final precision could not be better than $\sim$10%. In addition, the downward transients to the dark levels are considered to be exponential-like while we know that the decreases appear to be rather hyperbolic in reality. Finally, this inversion method does not work for pixels with high gradient of illumination (especially point sources) since it neglects the charge coupling.

As we have already mentioned, these inversion methods were abandoned in the case of LW detectors at the end of the ISO mission in favour of the above refered Fouks-Schubert description of the problem, which turned out to provide much more accurate results (see Fig. 5.5).

5.2.5 Spatial and temporal filterings: use of redundancy

In several observations the main error for data processing under quasi uniform illumination do not come from transients but from glitches, Long Term Drifts (LTDs) or Small Amplitude damped Oscillations (SAOs). Especially observations of very faint point sources or extended structures on top of uniform illumination (e.g. zodiacal emission) with CAM-LW can be contaminated by glitches, LTDs and SAOs.

When the scientific objective is to extract real faint point sources (e.g. cosmological surveys), LTDs and SAOs can be more or less easily removed using spatial or temporal filterings. In that case, the limiting factor are the glitches (Agnèse et al. 1991; Fouks 1996), especially the strongest and the faintest ones. Methods based on wavelets (Starck et al. 1999) or temporal filtering (Désert et al. 1999) have been used to reject artefacts due to glitches.

On the contrary, when the scientific objective is to measure the emission of low contrasted extended structures (e.g. diffuse interstellar clouds) the limiting factors are LTDs and SAOs. Because different sky positions have been generally observed several times, a method based on the use of the redundancy can be applied (Miville-Deschênes et al. 2000).

For spectroscopic observations with the Circular Variable Filter of CAM-LW, the spectra are often observed with direct and reverse scanning direction. If the transient model and the transient correction are perfect, these direct and reverse scans after correction must be superimposed. This strong constrain can be used to estimate very accurately the initial conditions J_0^∞, which are generally unknown, in Eq. (2.1) for the transient correction. On the contrary, observations with only one scanning direction cannot be transient corrected without ambiguity when they start at low level because of the very long memory effect at such low levels.

In many cases it is possible to use the spatial redundancy of raster scans to extract the long-term transients from the data. If we suppose that:

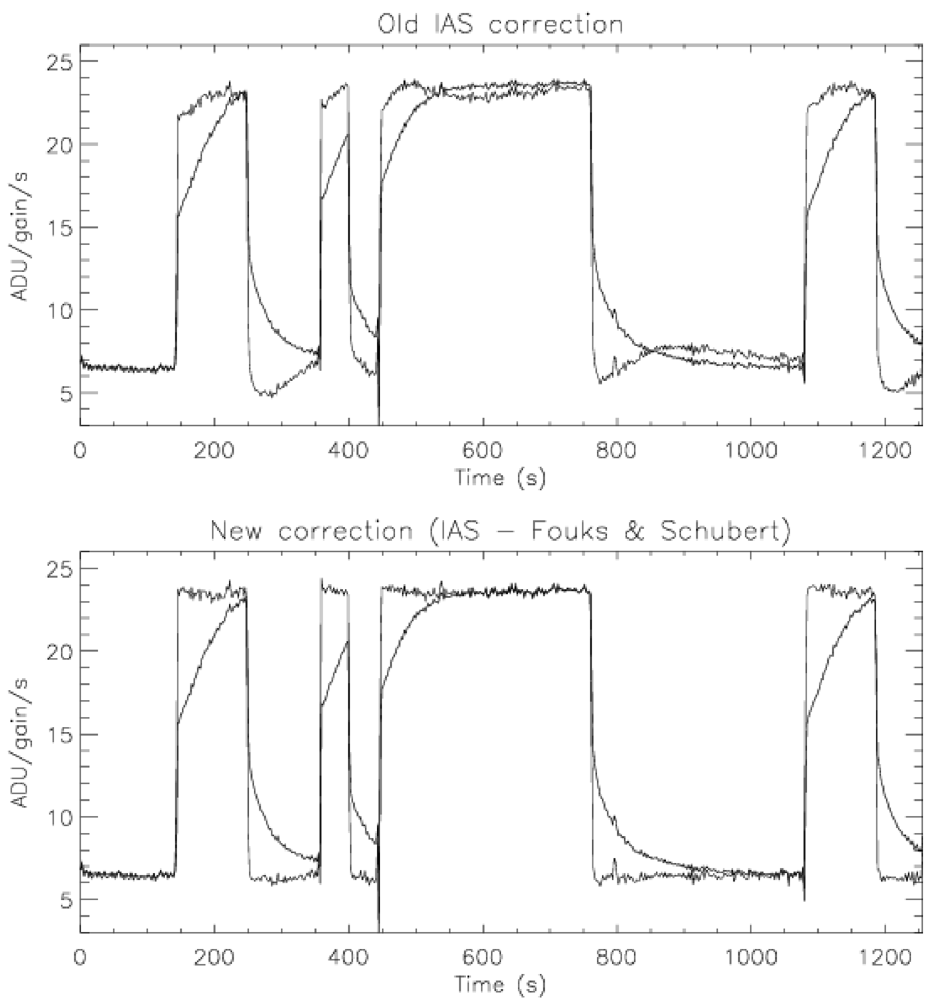

Figure 5.5: *Correction of transients with the 'old IAS method' (upper panel) and with the Fouks-Schubert model (lower panel)*

$$I_{obs}(x, y, t) = F(x, y, t)\ I_{inc}(x, y, t) + \Delta(t, I) \tag{5.16}$$

where $I_{obs}(x, y, t)$ is the observed flux at time t on pixel (x, y), $I_{inc}(x, y, t)$ is the incident flux at time t on pixel (x, y), $F(x, y, t)$ is the time-dependent flat-field and $\Delta(t, I)$ is the long-term transient, the problem is then to find $\Delta(t)$ which minimizes the differences between pixels that have seen the same sky. Note that the LTT is found to be from the observations an offset effect and not a gain effect.

By comparing pixels that have seem the same position on the sky, we obtain a set of linear equations that can be solved preserving the real sky structure and behave well always when the long-term transient effect is at least a factor of 2 larger than the noise. This way, it is possible to separate the contribution of the sky emission and of instrumental effects to the observed signal.

In principle, the processing of astronomical data with spatial redundancy could be treated in a global manner, as an inversion problem. However, ISOCAM's response is still not well understood and it is impossible to address the problem just by a single inversion. Thus, a sequential approach where the instrumental effects are treated one by one was adopted. In particular, the ISOCAM long term frift can be addressed by a least square minimization technique based on the fact that, if the detector is slowly reaching stabilization, the measured flux is also approaching the real flux. Here we suppose that every pixel of the array is affected by the same long-term drift, something which is not totally true, since pixel to pixel variations (few percents) are visible. On the other hand, using a variable flat-field allows us to take into account most of these variations.

Once the LTT is removed, the other response variations (slow glitches, ghosts and residual transient effects) are corrected by comparing the data cube to the sky image. This is done in two steps. First, a variable flat-field is computed that takes into account pixel-to-pixel response variations. Second, pixels that have a flux that departs significantly from the sky image are flagged out. This last operation removes slow glitches and ghosts. Iterating these two operations will improve the sky image.

The occurrence of LTT seems to be correlated with flux steps (when the detector sees a strong flux after being on a low level flux for a long period of time). A correlation with detector temperature variations has also been searched for. This was justified by the fact that the LTT is generally rising while the detector temperature is usually decreasing during an observation (the temperature increases each time the filter wheel is moved). Contradictory cases were observed: some observations with identical temperature have significantly different long-term transient.

A more detailed description of how the ISOCAM data processing can be improved by using spatial redundancy can be found in Miville-Deschênes et al. (2000).

5.3 Results achieved

5.3.1 Transient correction in SW detectors

It is difficult to assess whether the model proposed in Sect. 5.2.1 brings an actual improvement to the quality of the data as long as we cannot compare a calibrated image of an extended faint object with one produced with this algorithm. However, as an example, we show in Fig. 5.6 a comparison of a cut through two images of the edge-on galaxy NGC 891 obtained on one hand with ISOCAM-LW (filter LW1 centered at 4.5 μm, see Rouan et al. 1997 for a description of the ISO programme) and on the other hand with ISOCAM-SW (filter SW1 centered at 3.6 μm), after processing with our algorithm. One does not expect large differences between the

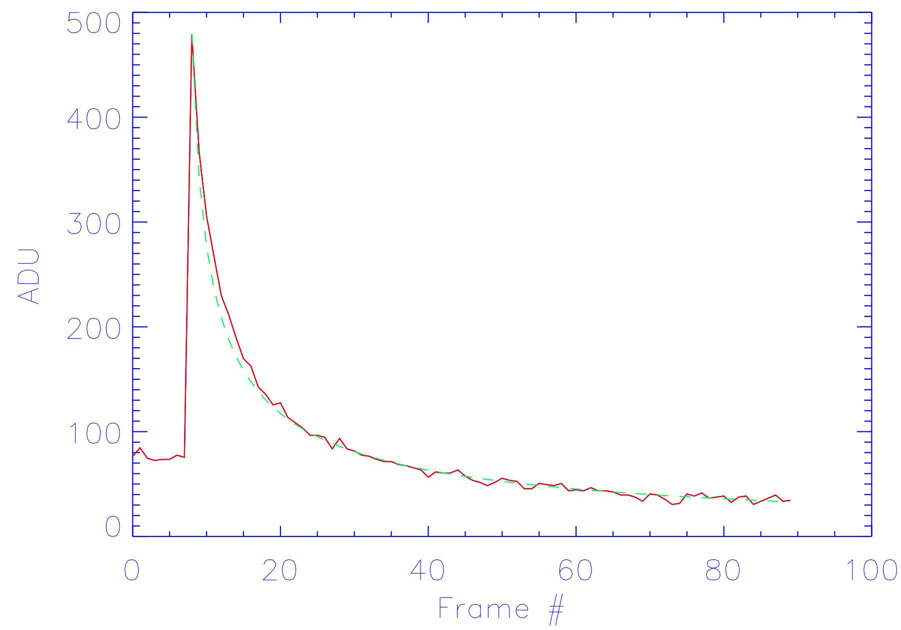

Figure 5.6: *Comparison of cuts along the main axis of the edge-on galaxy NGC 891 in two images obtained with ISOCAM. Solid line: image obtained in the short wavelength channel (SW1 filter at 3.6 μm), the cube being processed as described in the text; dotted line: image obtained with the long wavelength channel of ISOCAM (LW1 filter at 4.5 μm).*

two images which are at rather close wavelengths; the good overall fit of the relative variations in flux can be considered as a rather positive indication of the validity of the process.

5.3.2 Transient correction under quasi-uniform illumination in LW detectors

The transient correction based on the Fouks-Schubert model is in principle only valid for low gradient illumination conditions. Thus, only the photometry of extended sources and of very faint point sources is expected to improve significantly.

A first example of the kind of improvements achieved has already been shown in Fig. 5.5, where we illustrated the quality of the correction of real data in comparison with the results obtained using the *'old IAS method'*.

In order to show the effect in more detail we can have a look at the CAM-CVF observation of the faint extended source IC 443. Fig. 5.7 shows the OLP v9.5 spectrum of IC 443 (with Fouks-Schubert transient correction included) compared to the same spectrum reduced with OLP v8.4 (which does not include this correction). We can see that the peak strengths of the emission lines are noticeably stronger and the line bases are narrower. At the same time the baseline at short wavelengths has become much closer to the zero emission level.

Figure 5.8 shows another example of the improvements introduced in OLP v9.5 by the transient corrector. A reconstructed raster map of the spiral galaxy M51 is presented (taken from OLP's CMOS product file). The left image is that of OLP v9.5; the right comes from OLPv9.1 (with no transient correction). Both images are copied using exactly the same set of upper and lower cuts (0.005 and 0.003 respectively). The first most evident difference is the almost total removal

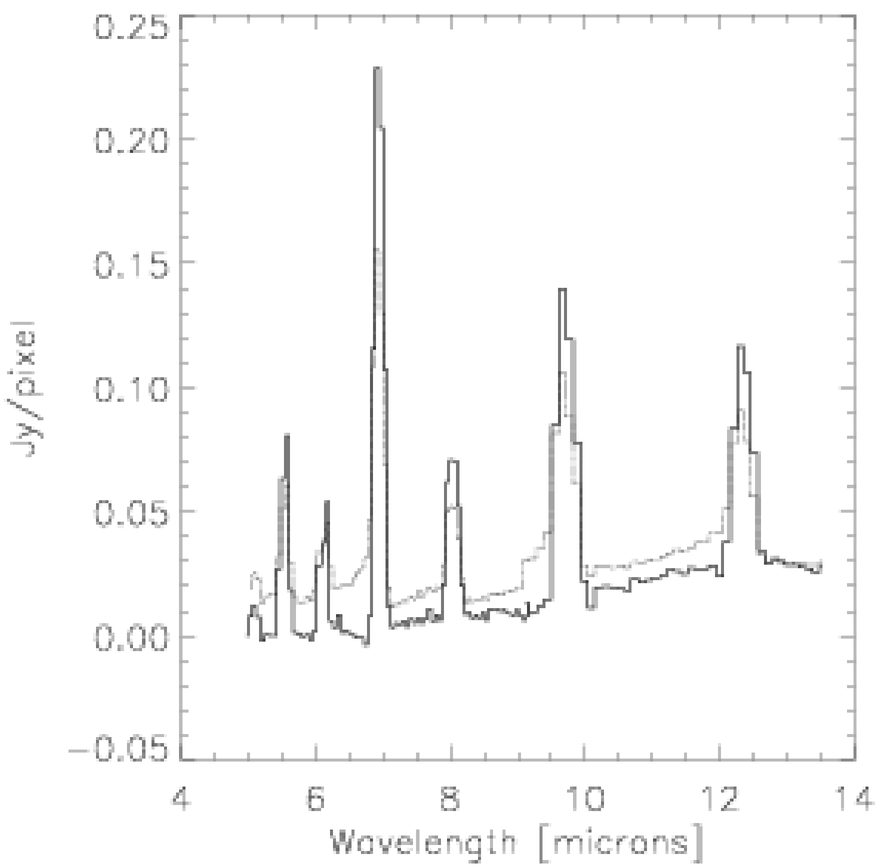

Figure 5.7: *OLP v9.5 spectrum of IC 443, with the Fouks-Schubert transient correction (solid) and without transient correction (dotted)*

of the ghost image of the bright companion, the leftmost bright object in the images. The second obvious difference is the elimination of the fuzziness between the spiral arms, due to rem effects. The third obvious difference is the enhanced arm-interarm contrast visible in the OLP v9.5 image.

5.3.3 Transient correction of point sources

When the observed field contains high spatial gradients, the Fouks-Schubert model cannot describe the observations and the corrections proposed by the model generally fail. This is critical for point sources since the responses measured for bright sources are actually never properly corrected.

For the same initial and final levels (after stabilization), the response of all pixels where the point source has been detected departs form the uniform illumination response. For the brightest pixel the response is (1) generally non-monotonous; (2) faster than the Fouks-Schubert one; and (3) a peak appears for strong sources (brighter than 80 ADU/G/s above the background). The brighter the source, the higher that peak.

Alain Coulais, at IAS, in collaboration with Boris Fouks, are still trying to find a possible

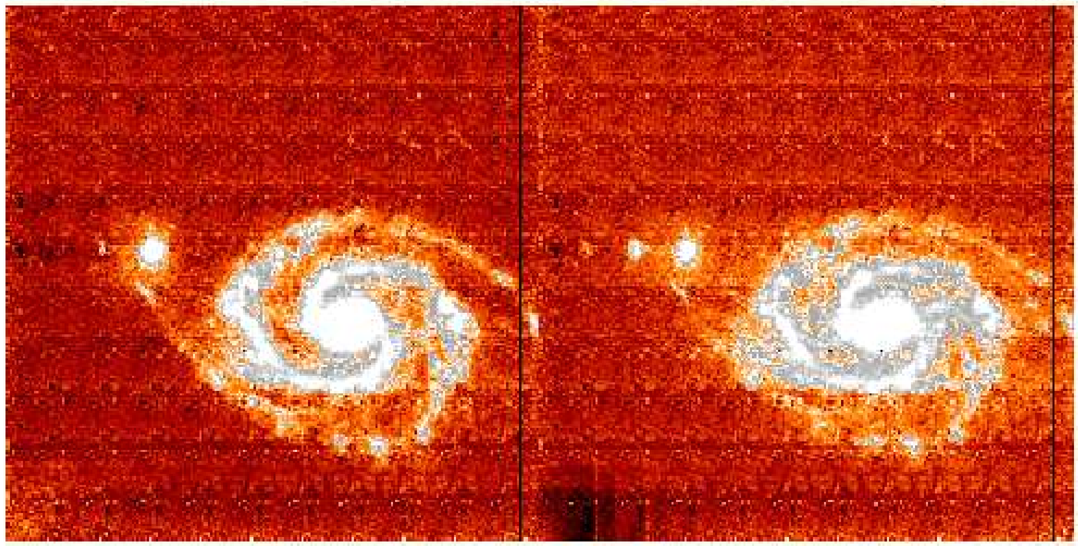

Figure 5.8: *Image of M51 with transient correction (OLP v9.5, left) and without (OLP v9.1, right). Note that most ghost images have almost disappeared, particularly the ghost of the strong companion to M51, and the enhanced arm-interarm contrast in the transient corrected image.*

solution to the problem of describing the transient behaviour of point sources in ISOCAM data.

Efforts are concentrated on in-flight data taken with CAM with the $1.5''$ lens and filters LW10 and LW3 (largest PSF) where the lowest spatial gradients on individual pixels are expected.

Unfortunately, none of the empirical models tested so far give correct responses (closer than 10% for each pixel and each readout).

Recently, an innovative 3-D approach is being tried which looks promising. First attempts were based on an inaccurate knowledge of some important parameters of the detectors (both geometrical and electrical). Part of these missing parameters were unknown, others were not published because they were not considered useful in the past. The new model takes into account the true geometry and good parameters of the detectors in order to derive an adapted semi-analytical model (only recently it was found that between each contact there is another electrode which can have an important effect on the model, and the sizes of bottom and upper contacts have been determined).

Additional tuning of the model is still on-going (taking into account the reflecting plane, for instance, or the rectangular geometry of the pixels, so far considered circular). This is needed in order to obtain satisfactory quantitative results (may be up to the 5-10% level of accuracy). Still there are problems not solved, like how to deal with the different behaviour in the transient response as a function of the precise part of the pixel which is illuminated by a given point source (the behaviour is not the same if the point source falls at the centre of the pixel or at the edges).

The new 3-D equations have been obtained with the current conservation condition (1-D) replaced by the continuity equation (3-D) and some new boundary conditions. The kernel so created is the 3-D equivalent to the 1-D description of the problem and shows how the field of the charges created under a flux change in one point of the (x, y) plane penetrates through the bulk and spreads to all sides creating a 3-D picture of the force lines of the field. This effect is strong because the screening length for the charges, created in the bulk of low-background detectors under a time-variable irradiation, is very long, creating cross-talkings (current spreading). A pixel is illuminated, but the charge from it creates currents in neighbouring pixels (see Fig. 5.9). Under homogeneous irradiation, the influence of the 3-D field effects on the transient current in the detector can be described with a good exactness in one dimensional (1-D) approximation with the use of the field averaged along the contact planes and with the re-normalization of the contact parameter E_j. For highly inhomogeneous irradiation such approach is impossible, and 3-D equations must be used.

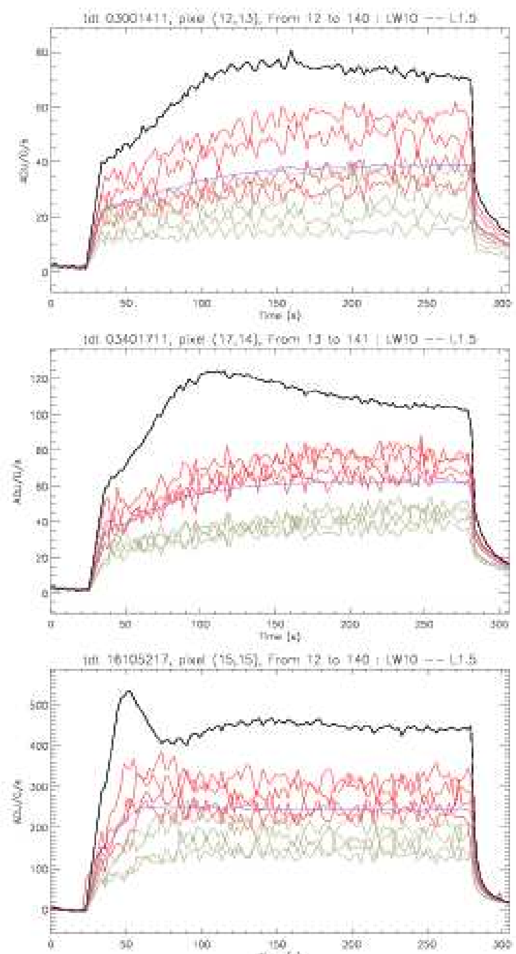

Figure 5.9: *Signals coming from the 3x3 pixels around point sources detected with CAM are shown in the left panels for three different flux levels. The central pixel is plotted in dark; in red, the four closest neighbour pixels; in yellow the four pixels in the corner; the blue line is the mean of the 9 pixels - Alain Coulais*

The computed results derived from the currently simplified 1-D model (see Fig. 5.9) illustrate the current spreading (the appearance of the current in dark regions neighboring to the illuminated ones) that results from the spreading of field lines and the current overshooting that results from a high current density in the region under a high-density flux. The presented results give rather good qualitative description of the transients under point-source illumination. In order to get an exact quantitative description of the transients the theory has to take into account the real 3-D topology of the detectors and their conductive surroundings.

Unfortunately, the amount of work pending is considerable and it will not be possible to include any tool to correct point source fluxes for transients in the ISOCAM pipeline.

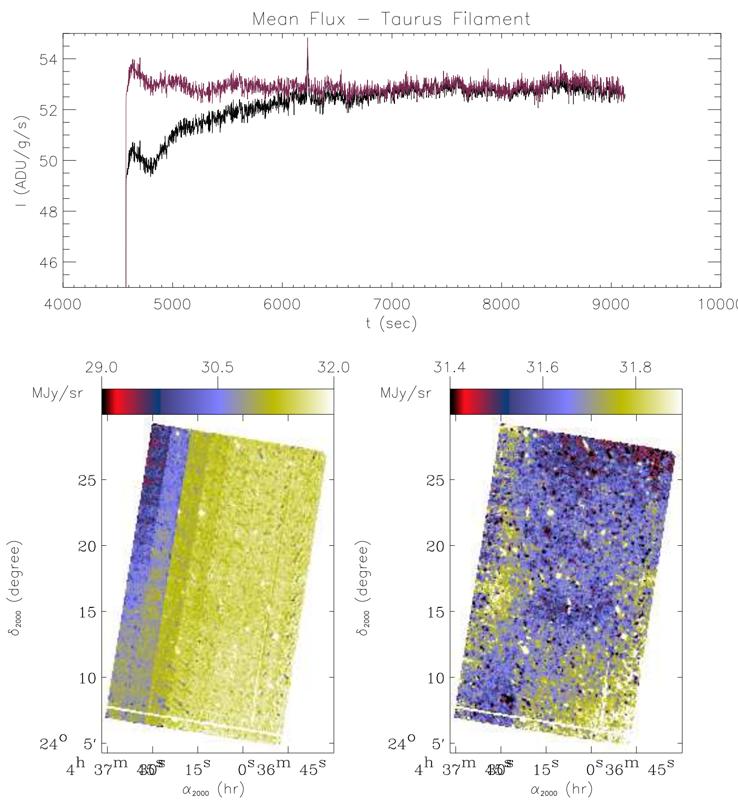

Figure 5.10: An example of the application of the long-term transient correction to ISOCAM observations of diffuse galactic clouds. In the upper panel the mean flux detected in the LW3 filter on the same faint extended emission field in Taurus shown in Fig. 5.1 is plotted before and after long-term transient correction. The full CAM image is displayed below before and after the application of the correction - Marc-Antoine Miville-Deschênes

5.3.4 The use of redundancy in raster maps

In practice, the implementation of the minimization algorithm described in Section 5.2.5 to correct raster maps for LTT effects is a non-straightforward procedure. An extensive use of the LTT inversion method has demonstrated the extreme importance of an accurate flat-field and of a field-of-view distortion correction. Both effects introduce noise which may be correlated with the signal, making the LTT correction to converge to a wrong solution.

In spite of this, the results obtained on several raster maps for which independent data exist taken at several epochs suggest that the LTT correction applied is able to restore properly the large scale structure of diffuse emission in the fields observed. Furthermore, almost all point-like structures are preserved giving confidende to the bad pixels identification.

An example of the results obtained is shown in Fig. 5.10. With this processing technique it is possible to detect structures as faint as 30-40 μJy at 5σ level. Instrumental effects are so well controlled in the data reduction that the noise in the final map is dominated by the readout and the photon noises.

5.4 Implementation in CIA/pipeline

As we have already mentioned, it has not been possible to find a model able to describe the transient behaviour of SW detectors in ISOCAM. Thus, no transient correction is applied in the pipeline to measurements taken with ISOCAM-SW, nor is there any tool available to correct for this effect in CIA.

The situation is somewhat better for LW detectors. The Fouks-Schubert method is now fully implemented in CIA and, as of version 9.5, also in the CAM pipeline. Note that the method is in principle only valid for low gradient illumination conditions. Thus, only the photometry of extended sources and of very faint point sources is improved significantly. In spite of this the method can be applied blindly in the pipeline to any source observed with ISOCAM-LW in the pipeline, including point sources, because it does not have a negative impact on their absolute photometry. Analysis performed on a number of test cases indicate that, esentially, the transient corrector is non-operant in the case of point-like sources (at least the absolute flux photometry did not become worse).

Access to the long-term transient correction and variable flat-field algorithms routines above described is possible via the SLICE package (developed by M.-A. Miville-Descênes) only in CIA. Of course, in this case, the high degree of interactivity needed does not allow its implementation in an automated pipeline.

Chapter 6

Transient effects in LWS data

6.1 Impact on LWS detectors

All LWS detectors exhibit transient behaviour. This falls into two main categories, a long term transient due to the steady accumulation of particle hits during each revolution and a short term transient caused by changes in flux. In terms of calibration the transients cause two problems, the correct determination of line strength and wavelength and the determination and application of a steep edged spectral response function.

Figure 6.1 shows the response of the three detector types in LWS to a illuminator sequence. The Ge:Be detector SW1 has a long time constant (several minutes) in response to illuminator 1 and this is also apparent when the illuminator is switched off. The unstressed detectors have a fairly flat response whereas the stressed detectors have a hook response.

One of the major effects of transient behaviour is in the determination and application of the relative spectral response function (RSRF). LWS is operated in a mode where the grating is scanned forward and backward through the spectral range. For most detectors the scans pass through steep sided RSRFs and the resultant profiles are clearly split with the photocurrent dependent on scan direction. The calibration stategy up to now in the derivation of the spectral response function has been to average all data before dividing by the Uranus model. However when this averaged RSRF is applied in the pipeline it leads to scan dependent behaviour in the resultant spectra. Figure 6.2 shows a spectrum of Uranus for the two worse affected detectors SW1 (Ge:Be) and LW2 (Ge:Ga(s)). In the case of SW1 the response function is triangular leading to a cross over effect at the top of the response function (around 48 μm). LW2 has a steep sided response at the long wavelength side and has a relatively long time constant (a few seconds). One possible approach is to use two RSRF functions, each derived only from scans in one direction. Attempts at this calibration stategy have so far led to promising results.

The transient behaviour of the LWS detectors also affects the line flux accuracy. The effect is dependent on both the line flux and illumination history, and at this time no correction is done. The effect however is minor with the worst case stressed Ge:Ga detectors only affecting the line flux by a few percent. The unstressed Ge:Ga detectors although exhibiting transient behaviour have very short time constants and have a negligible effect on line fluxes. The detector most affected is the Ge:Be detector which has time constants of the order of minutes, however very few bright lines have been observed in this wavelength range (43-51 μm).

In the case of Fabry-Pérot observations made with LWS, it has been observed that the line profiles observed using AOT LWS04 are generally asymmetric, with the long wavelength wing at a higher level than the short wavelength one. This phenomenon is partially attributed to memory effects, also present in grating spectra. Various methods for removal of transient effects

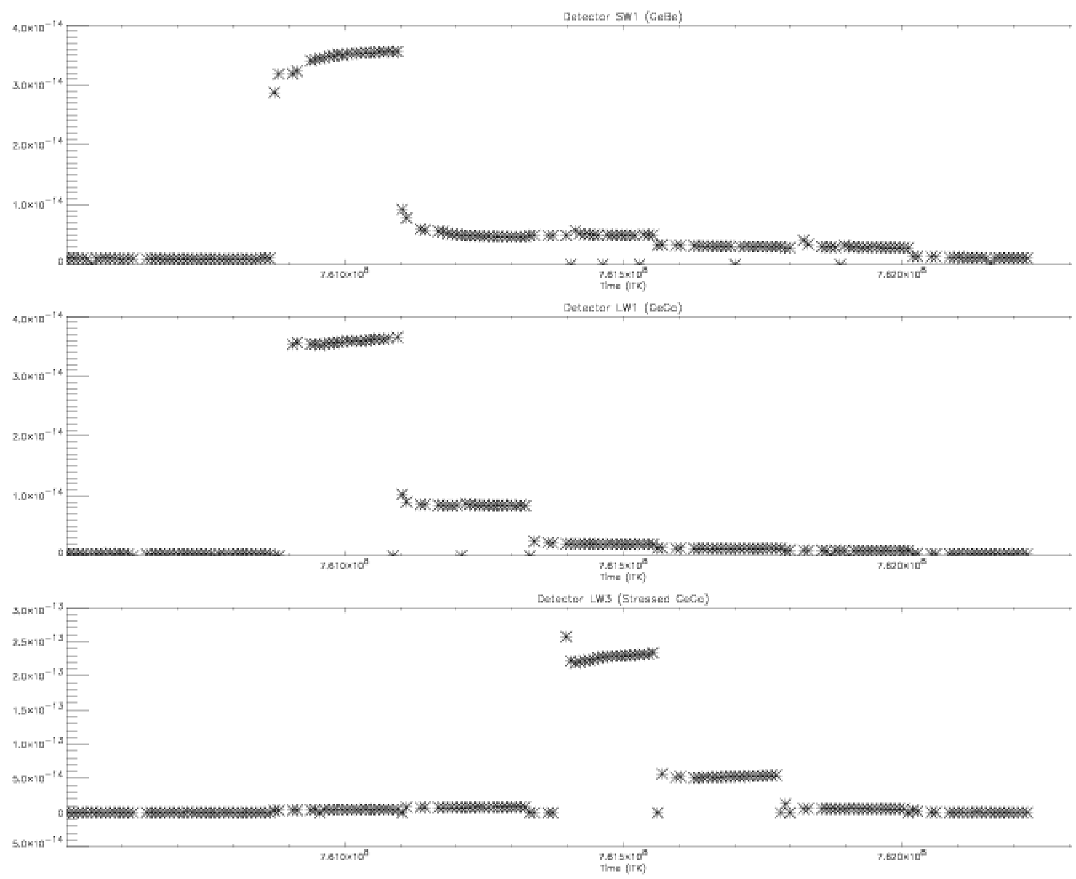

Figure 6.1: *The response to an illuminator sequence of the three detector types used by LWS: Ge:Be SW1 (top); unstressed Ge:Ga LW1 (middle); stressed Ge:Ga LW3 - Tanya Lim*

are being investigated. The effect on line flux depends on the line-to-continuum ratio. For example, for a line with no continuum, the line flux can change by as much as 30%. The effect on the velocity shift is relatively small (about ± 3 km s^{-1}). It is also possible that some of the profile asymmetry observed may well be due to loss of parallelism as the Fabry-Pérot line is scanned.

6.2 Efforts developed to correct LWS data for transient effects

Emmanuel Caux is working on the correction for memory effects in LWS data applying a correction based on the Fouks-Schubert model adapted for LWS data.

Although the Fouks-Schubert model, as we have already mentioned, is in principle not applicable

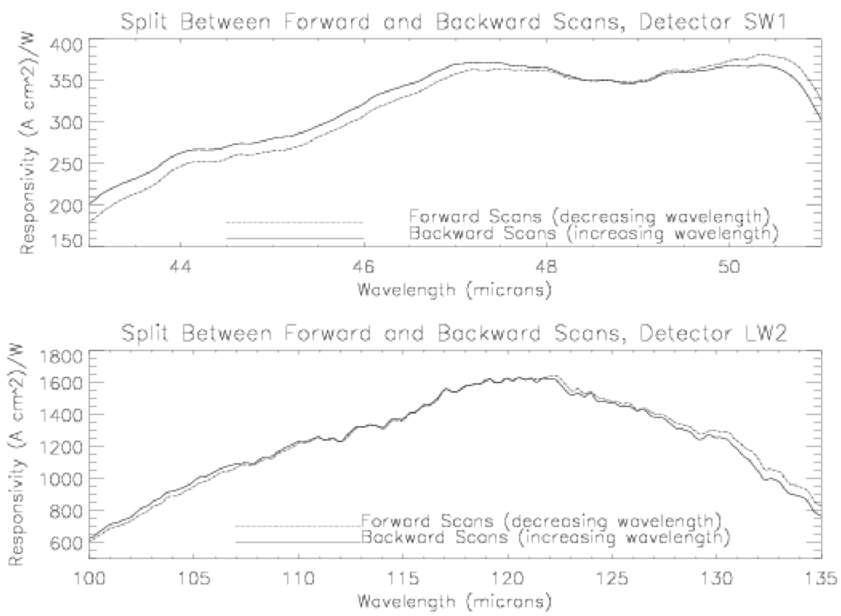

Figure 6.2: *Spectrum of Uranus showing split between forward and backward scans for the two detectors worse affected by transient behaviour - Tanya Lim*

to Ge-based detectors (with the exception may be of LWS parallel mode observations), memory effects can be at least partially removed for LW detectors which are based on Ge:Ga (note that the stronger memory effects are observed in the stressed Ge:Ga detectors LW2 to LW5) by the application of this correction (see Figure 6.3)

Satisfactory results are obtained in all cases when the modified Fouks-Schubert method was applied. The method also consider overshooting effects for big flux jumps.

The situation is worse for Ge:Be detectors (the case of SW1) where Fouks-Schubert model simply does not work.

...

Emmanuel, here you must include the basics of your approach using Fouks-Schubert model. Formulae, figures and other details concerning how you apply the model should be included. You can take the info from your contribution to the Proceedings of the Calibration Legacy Conference.

...

Exploring all space parameters for α, β and E the analysis performed so far leads to the following conclusions:

1. β is rather constant (0.74 to 0.95, depending on the detector considered)
2. α and E are not independent ($\alpha = a - blog(E)$)

The routine used to find the Fouks-Schubert parameters is stable, but it still remains to check posible dependences on the spectral shape of the source.

The quadratic difference of forward/backward scans is more important for detectors presenting

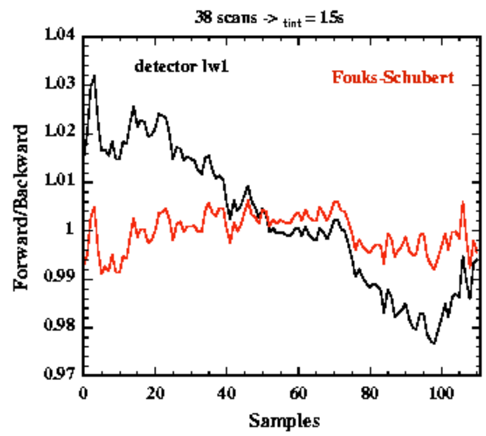

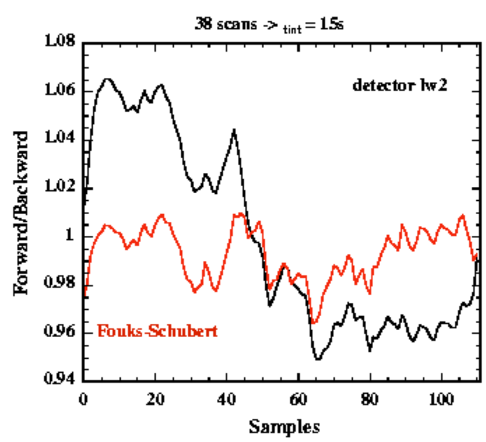

Figure 6.3: *Ratio of LWS forward/backward scans before and after the application of the transient correction based on the Fouks-Schubert model - Emmanuel Caux*

a large memory effect (SW1, LW2 and LW3). This gain depends also on the type of source observed; extended sources with large fringing lead to a much more important effect than point sources observed with the same detector and similar photocurrent on the detector.

This has to be expanded, Emmanuel. I do not have access to the text and figures you presented at our last meeting in Orsay, nor do I have your contribution to the Proceedings of the Calibration Legacy Conference.

The implication of this transient effect correction on line flux calibration, wavelength calibration and spectral resolution has to be discussed.

6.3 Results achieved

This has to be written , Emmanuel (show some examples!). Some results on grating and Fabry-Pérot LWS observations were presented at the Legacy Conference.

6.4 Implementation in LIA/pipeline

Transient corrected RSRFs (at least for LW detectors) using the adapted Fouks-Schubert model, are now being produced at CESR by Emmanuel Caux. The new RSRFs so obtained differ by just a few percent with respect to the old ones. The impact on the whole LWS calibration will be investigated by Tanya Lim at RAL. The improved RSRF will be implemented in LIA, but never in OLP v10. The goal is to issue a dedicated LIA routine to perform the transient correction.

Chapter 7

Lessons applicable to the Future

Several important facts about transients of low background IR detectors have been learned during the ISO mission. Furthermore, dedicated signal processing methods have been set up for correcting these transients.

One very important result, true for all the Ge:Ga and Si:Ga detectors which have been analyzed is that all of them present reproducible memory effects and non linear transient behavior.

The models to describe such transients must be non linear and data pre-processing (dark correction) must be as accurate as possible since the response depends on the value of the measured signal above the dark level. This problem is obviously more critical at low level.

For most of the Si:Ga detectors on-board ISO under quasi uniform illumination, a 1D non linear model based on physics describes with a precision of a few % the transient responses observed during the flight. Other effects (Long Term Drift, Small Amplitude Oscillations, limited hook effect at very high flux steps, ...) have been predicted before ISO mission (Vinokurov & Fouks 1988) and have been observed in SWS, PHT and CAM transients. Unfortunately, due to time constrains during the ISO life, a limited number of tests were performed to characterize these second order effects. Moreover the data sets are often perturbated by parasitic effects (time discontinuity for CAM ground based data, glitches during flight, ...). In any case, the experience from ISO will be very useful to optimize future generation of Si:Ga detectors used in astronomy.

Another result concerns the electrical cross-talk between pixels in linear and matrix arrays which can be very strong. Unfortunately, point source measurements are often not optimal (too short observations, unproper initial conditions, limited number of configurations) in order to characterize accurately the cross-talk during the flight. For Si:Ga matrix array, promising qualitative results have been achieved with the simplified 3D model described in Sect.5.2.3.

Physics predict a much more difficult behavior of Ge:Ga detectors to describe using analytical models (less simplification in non-linear differential equations and more technical difficulties to make such detectors ...). Nevertheless it may be possible to describe the transients in Ge:Ga detectors with acceptable exactness by computations based on Fouks general model, but this work is complex and it could be complicated by extra physical (quantum) effects inherent to Ge:Ga detectors and especially the stressed ones. The next generation of Ge:Ga matrix arrays for SIRTF and ASTRO-F may also present complicated transient effects. For these future detectors, ground based tests using what we have learned form ISO have to be systematically performed in order to design the best observing strategy and prepare adequate transient corrections.

7.1 Acknowledgements

DK would like to thank all the people who contributed to the correction of band 2 data for transient effects by critically evaluating the results of the DYNADARK procedure. And especially Russ Shipman and Helmut Feuchtgruber for providing the band-border ratio plots.

AC thanks CNES, CEA SaP and IAS for financial support. AC is debtfull with B. Fouks, his incredible knowledge of the physics of low background IR detectors, his kindness and pedagogy. AC also thanks L. Vigroux, A. Agnèse and P. Mottier, designers of CAM-LW, as well as M.-A. Mivile-Deschênes, K. Okumura, S. Bouaissi and F. Balleux.

Bibliography

[1] Abergel A., D'esert F.-X., Aussel H., 1996, A&A 315, L329

[2] Abergel A., Miville-Deschêne, M.A., Désert F.-X., Pérault M., Aussel H., Sauvage M., 2000, ExA 10, 353

[3] Agnèse P., Lucas C., Maillart P., Mottier P.L., 1989 *Proceedings of SPIE* 1070, 124

[4] Agnèse P., Engelmann J.J., Mottier P.L., 1991 IEEE Trans. on Nuclear Science 38, 953

[5] Bertsekas D.P., 1995 *Non-linear programming.* Athena Scientific, Belmont, Massachussets, USA

[6] Biviano A., ESA Technical Report (check SAI number) 1998

[7] Boulade O. & Gallais P., 2000 ExA 10, 227

[8] Castañeda H.O., Klaas U., ExA 10, 369

[9] Caux E., 1999 CESR Technical Report - CNRS, France

[10] Cesarsky C. et al., 1994 Optical Engineering 33, 751

[11] Cesarsky C., Abergel A., Agnese P. et al., 1996, A&A 315, L32

[12] Church S.E., Price M.C., Griffin M.J., et al. 1992, in *Photon Detectors for Space Instrumentation*, ESA-SP 356, p. 261

[13] Church S.E., Griffin M.J., Price M.C. et al. 1993, *Proceedings of SPIE* 1946, 116

[14] Church, S.E., Price, M.C., Haegel N.M., Griffin M.J., Ade, P.A.R., 1996 Applied Optics 35, 1597

[15] Coulais A., Abergel A., 2000 A&AS 141, 533

[16] Demoment E., 1989 in *IEEE Trans. Acoust. Speech, Signal Processing*, ASSP 37, 2024

[17] Désert F.-X., Puget J.-L., Clements D.L. et al., 1999 A&A 342, 363

[18] Fouks B.I., 1981 Sov. Phys. Semicond. 15(9), 974 + 980

[19] Fouks B.I., 1992 in *Photon Detectors for Space Instrumentation*, ESA-SP 356, p. 167

[20] Fouks B.I., 1996 *Proceedings of SPIE* 2817, 160

[21] Fouks B.I., 1997 *Proceedings of SPIE* 3122, 441

[22] Fouks B.I., Schubert J. 1995 *Proceedings of SPIE* 2475, 487

[23] Fouks B.I., Kocherov V.F., Taubkin I.I., Vinokurov L.A., Zaletaev N.B., 1994 Optical Engineerning 33, 1485

[24] Fujiwara M., Hiromoto N. and Araki K. 1995 *Proceedings of SPIE* 2552, 421

[25] Gabriel C., Acosta-Pulido J.A., 1999, in *The Universe as seen by ISO*, Eds. P. Cox & M.F. Kessler, ESA-SP 427, p. 73

[26] Gabriel C., Acosta-Pulido J.A., Heinrichsen I., Skaley D., Morris H. and Tai W-M., 1997 *Proceedings of ADASS VI Conf.*, eds. G. Hunt and H.E. Payne, p. 108

[27] de Graauw T. et al. 1996 A&A 315, L49

[28] Groezinger U., Kirches S., Lemke D., Schubert J., Schulz B., Beeman J.W. 1992, in *Photon Detectors for Space Instrumentation*, ESA-SP 356, p. 329

[29] Haegel, N.M., Latasa, C.A. and White, A.M., 1993 Appl. Phys. A., 56, pp. 15

[30] Haegel, N.M., Newton, C., Simoes, J.C. and White, A.M., 1996 30th ESLAB Symp., 15

[31] Haegel N.M., Simoes J.C., White A.M., Beeman J.W., 1999, Applied Optics, 38(10), 1910

[32] Hartung J. 1991, *Statistik - Lehr und Handbuch der angewandten Statistik*, Ed. R. Oldenburg (Verlag)

[33] Idier J., 1999 in *3rd International Conference on Inverse Problems in Engineering*, p. 1, Port-Ludlow, USA

[34] Kessler M., Teinz J. A., Anderegg M.E., 1996, A&A 315, L27

[35] Kester D., 1999, SRON Technical Report (check code number if any)

[36] Kester D., 2000 in *ISO beyond the Peaks* Eds. A. Salama, M.F. Kessler, K. Leech, B. Schulz. ESA-SP 456, p. 275

[37] Laureijs R., Klaas U., Richards P.J., Schulz B., Ábrahám P., 2000 *The ISO Handbook - Volume V - PHOT: The Imaging Photo-Polarimeter V1.1*, ESA SAI/99-069/Dc

[38] Leech, K. et al., 2000 *The ISO Handbook - Volume VI - SWS: The Short Wavelength Spectrometer* ESA SAI/2000-008/Dc

[39] Leeks S.J., Swinyard B., Lim T., P.E. Clegg, in *The Universe as seen by ISO*, Eds. P. Cox & M.F. Kessler. ESA-SP 427, p. 81 (1999)

[40] Lemke D., Wolf J., Schubert J., Patrashin M., 1993 *Proceedings of SPIE* 1946, 261

[41] Lemke. D., Klaas, U., Abolins, J. et al. 1996, A&A 315, L64

[42] Miville-Deschênes M.-A., Boulanger F., Abergel A., Bernard J.-P., 2000, A&AS 146, 519

[43] Patrashin M.A., Fouks B.I., Lemke D., Juergen W., 1995, *Proceedings of SPIE* 2475, 476

[44] Pérault M., Désert F.-X., Abergel A., et al. 1994, Optical Engineering 33, 762

[45] Press W.H., Teukolsky S.A., Vetterling W.T., Flannery B.P., 1992 *Numerical Recipes, 2nd Edition* (Cambridge University Press).

[46] Rouan D., LeCoupanec P., Lacombe F., Tiphène D., Gallais P., Giard M., Léger A., 1997, in *Diffuse Infrared Radiation and the IRTS*, ASP Conference Series 214, p.343

[47] Sclar, N. (1984) Prog Quant. Electr. 9, 149

[48] Schubert J. , Ph.D. Thesis, Max-Planck Institut für Astronomie, Heidelberg, 1995

[49] Schubert J., Roth G., Wolf D., Lemke D., Fouks B.I., 1994 *Proceedings of SPIE* 2268, 283

[50] Schubert J., Fouks B.I., Lemke D., Wolf J., 1995 *Proceedings of SPIE* 2553, 461

[51] Sée J., 1999 Technical report, Stage de magistère.

[52] Siebenmorgen R., Blommaert J., Sauvage M., Starck J.-L., 2000 *The ISO Handbook - Volume III - CAM: The ISO Camera V1.1* ESA SAI-99-057/Dc

[53] Sorenson H.W., 1980 in *Parameter Estimation*, volume 9 of *Control and System Theory*. Marcel Dekker, Inc., New-York and Basel

[54] Starck J.-L., Aussel H., Elbaz D., Fadda D., Cesarsky C., 1999 A&AS 138, 365

[55] Tiphène D., 1987, Ph.D. Thesis, Universit'e Paris XI

[56] Tiphène D., Lacombe F., Rouan D., 1988 *Proceedings of SPIE* 865, 122

[57] Tiphène D., Rouan D., Epstein G., LeCoupanec P., 2000 ExA 10, 347

[58] Vinokurov L.A., Fouks B.I., 1988, Sov. Phys. Semicond. 22(11), 1258

[59] Vinokurov L.A., Fouks B.I., 1991, Sov. Phys. Semicond. 25(11), 1207

[60] Vinokurov L.A., Zaletaev N.B., Kocherov V.F., Fouks B.I., 1992 Sov. Phys. Semicond. 26(4), 433

[61] Wensink J.W. et al. 1992, in *Photon Detectors for Space Instrumentation*, ESA-SP 356, p. 339

[62] Wolf J., 1994 Optical Engineering 33(5), 1492

Appendix A

A.1 SWS: Some Algebra used in the application of Fouks-Schubert model to band 2

The original Fouks-Schubert model gives the evolution for a step-like increases in incoming flux.

$$J_n(t) = \beta J_n^{\infty} + \frac{(1-\beta)(J_n^0 - \beta J_n^{\infty})J_n^{\infty}}{J_n^0 - \beta J_n^{\infty} + (J_n^{\infty} - J_n^0)\exp(-(t-t_n)/\tau)}, \tag{A.1}$$

where

$$\tau = \frac{\varepsilon E_j}{4\pi\beta J^{\infty}} = \frac{1}{\beta\Lambda J^{\infty}} \tag{A.2}$$

If we define the evolution during one reset interval as

$$J_n^+ \equiv J_n(t_n + \Delta t) \tag{A.3}$$

then we can write the continuity equation, also given by Fouks-Schubert as

$$J_n^0 = J_{n-1}^+ + \beta(J_n^{\infty} - J_{n-1}^{\infty}). \tag{A.4}$$

We furthermore identify the 'relaxed' signal with the incoming flux:

$$F_n \equiv J_n^{\infty} \tag{A.5}$$

We can write the evolution of the flux as

$$J_n^+ = \beta F_n + \frac{(1-\beta)(J_{n-1}^+ - \beta F_{n-1})F_n}{(J_{n-1}^+ - \beta F_{n-1}) - ((J_{n-1}^+ - \beta F_{n-1}) - (1-\beta)F_n)\exp(-\beta\Lambda\Delta t F_n)}. \tag{A.6}$$

And with the definition of α as

$$\alpha_n \equiv J_n^+ - \beta F_n \tag{A.7}$$

we get

$$J_n^+ = \beta F_n + \alpha_n, \tag{A.8}$$

where

$$\alpha_n = \frac{(1-\beta)\alpha_{n-1}F_n}{\alpha_{n-1} - (\alpha_{n-1} - (1-\beta)F_n)\exp(-\beta\Lambda\Delta t F_n)}. \tag{A.9}$$

For zero incoming fluxes (so called dark current measurements) we use l'Hôpital's rule to get

$$\alpha_n = \frac{(1-\beta)\alpha_{n-1}}{(1-\beta) + \alpha_{n-1}\beta\Lambda\Delta t}. \tag{A.10}$$

A.2 SWS: Temperature Dependency

The original Fouks-Schubert formula can be extended with temperature variations ΔT.

$$J_n(t) = \beta J_n^\infty + \frac{(1-\beta)(J_n^0 - \beta J_n^\infty)J_n^\infty \exp[(t-t_n)/\tau + \Delta T(t)/T]}{(1-\beta)J_n^\infty + (J_n^0 - \beta J_n^\infty)\int_{t_n}^t \frac{dt'}{\tau}\exp[\frac{-t'}{\tau} + \frac{\Delta T(t')}{T_j}]} \tag{A.11}$$

For SWS we assume that ΔT is constant during a reset interval. The integral in the denominator now can easily be solved. It becomes

$$\exp[\frac{\Delta t}{\tau} + \frac{\Delta T}{T_j}] - \exp[\frac{\Delta T}{T_j}] \tag{A.12}$$

$$J_n(t) = \beta J_n^\infty + \tag{A.13}$$

$$\frac{(1-\beta)(J_n^0 - \beta J_n^\infty)J_n^\infty}{J_n^0 - \beta J_n^\infty - (J_n^0 - J_n^\infty(\exp(-\frac{\Delta T}{T_j}) + \beta(1-\exp(-\frac{\Delta T}{T_j})))\exp(-\frac{\Delta t}{\tau})} \tag{A.14}$$

With the same definitions as before, for J^0, J^+, J^∞ and α we get

$$J_n^+ = \beta F_n + \frac{(1-\beta)\alpha_{n-1}F_n}{\alpha_{n-1} - (\alpha_{n-1} - (1-\beta)F_n\exp[-\frac{\Delta T}{T_j}])\exp(-\beta\Lambda\Delta t F_n)} \tag{A.15}$$

A.3 SWS: Error messages in dynadark and subsidiaries.

DYNADARK tries to fit the data of band 2 to a very specific model: model = influx + memory + zero level, where the influx is some average over the up and down scans of all detectors, memory is the Fouks-Schubert model for Si:Ga detectors and the zero level is a calculated piecewise linear function which makes the dark current samples minus the memory model equal to zero. This very specific modeling allows to do a *quality check in software* on some aspects of the observation. Most error messages that are generated by DYNADARK have to do with this quality check, telling the user that even the best fit of the data to the model leaves something to be wished. These messages are admonitions for the user to more closely inspect the data.

When an error is generated by DYNADARK, there are 3 possibilities

1. Something is seriously wrong with the data. E.g. detector jumps, pointing jitter which causes pepper noise, or one of various other unexplainable things. We are not claiming here that all, or even a large fraction of the detector jumps etc. are caught by DYNADARK.

2. The model has reached its limitations for this particular observation. The Fouks-Schubert model is an approximation of a much more complicated set of coupled differential equations. In general they cannot be integrated. For the Si:Ga detectors some approximations can be made and some terms can be neglected. This gives us a simplified model (Fouks-Schubert). One of the terms that is neglected contains the log of the flux step. In general the flux step is quite small in SWS, except in high flux observations of a few thousand Jansky or more. Some effects can also be seen at the start of the 'upscan'.

3. There is an error in the algorithm. Although the code has been successfully run on numerous observations, still there might be some occasions where a hidden assumption in the code is violated. In general these errors are easy to correct, once it is clear what assumption was wrong. All crashes of the code fall by definition in this category.

Below is a list of errors which can be generated by DYNADARK or one of its subsidiaries. For each message the code is given, its seriousness (W: Warning, S: Serious), it frequency of occurrence

1. Never yet
2. Rare < 1 %
3. Sometimes < 5 %
4. Fairly often < 10 %

And the actual message which is displayed. After that a short explanation follows which explains what condition was met and how it might affect the final product.

dynadark

SDY0 S 1 SPD too short to be processed
SPD is shorter than 10 samples. The original SPD is returned.

SDY3 W 2 simplex reports convergence problems
The simplex downhill algorithm has used, for at least one detector more than maxcall (=100) iterations. Although unusual, this condition is most likely corrected in the next overall cycle.

SDY4 S 3 20 cycles without complete convergence. $Delta\chi^2$ = xx
Most SPDs converge in half a dozen cycles. If it takes more than 20 something funny is going on which is certainly worth checking. This is not the same as saying that the solution found is totally wrong.

SDY2 W 3 1st cycle xx % better than last.
The SPD does not contain much memory to begin with. The overall χ^2 has increased a few percent. Start worrying when the percentage is larger than 25

SDY1 W 4 det dd, model is not optimal
The average of the residuals for this detector is larger than the standard deviation. The average of the residual for ALL detectors is a fortiori zero. Here we have the situation where at least one det is misbehaving. This could be due to our incomplete model.

init_zeropol

SZP0 W 3 No dark found for scan from itk0 to itk1 ... merging
There was no preceding or following dark-current for this particular section of the observation. It was merged (for zero level calculation only) with the preceding section.

make_stdev

SDY7 S 2 Infinites in matrix

SDY8 S 2 Determinant < 0

SDY9 S 2 Negative χ^2
All these conditions should not occur. Conditions like these should be reported as they could point to some error in the algorithm. These conditions only affect the calculation of the dark current errors. The dark itself could be perfectly OK.

fouks_model

SDY5 W 2 det dd, zero polynome corrupt... Corrected
The matrix used to calculate the polynome contains a row (column) with all zeroes. Although this should not happen it might occur when for some subscan all weights are zero. The matrix is repaired by placing a 1.0 on the diagonal. It has no effect on the other parameters and for the repaired parameter it does not matter as its effects were nil to begin with.

Appendix B

B.1 Inversion methods

B.1.1 Inverse problems

Inverse problems play an important role in numerous branches of engineering and applied physics : medical imaging, geophysics, astrophysics, *etc,* ... . In such fields, objects of interest (denoted $x \in \mathbb{R}^N$) can only be observed through a measurement system (denoted H). Such a system often involves blurring effects, transient response, high frequencies cut-off, *etc,* ... . Hence, the experimentalist, must start with an observed data set (denoted $y \in \mathbb{R}^P$), which is a degraded version of the true object x. In our context, measurements *i.e.* readouts $J_n(p)$, $p = 1, \ldots, P$ are a degraded version of the stabilized values J_n^∞, $n = 1, \ldots, N$. This degradation is essentially due to transient effects. Computations are then needed in order to *inverse* the distortion of the measurement system. Such a problem is usually decomposed in two sub-problems.

1. A *direct problem* founded on physical equations. Given the *true* object x and the physical properties of the observation system, one mathematically describes experimental readouts y. Such a model usually reads $y = H(x) + b$, where b accounts for model and measurement errors. The model H must be accurate enough in order to account for detailed physical phenomena at work and simple enough in order to allow efficient computations.

2. An *inverse problem* founded on data processing methods. Given the observed data set y and the physical model H, one inverses the data flow and decodes the true object from the observed data. In other words, the aim is to build an estimation $\hat{x}$ of the object x on the basis of the data set y and using the model H.

In spite their apparent diversity, most of the inverse problems encountered in applied physics suffer from a common feature (Demoment 1989; Idier 1999): *ill-posedness*, especially if $P < N$ or $P \simeq N$. Roughly speaking, this is due to the degradation achieved by observation systems : they definitely "corrupts" information from the true object into the data. So, information is missing in order to robustly inverse the system. Under such circumstances, reconstruction of the sought object x becomes tricky or even impossible on the sole basis of the data : small errors in the observed data may result in large errors in the reconstructed objects.

Numerous methods have been proposed to cope with ill-posedness (see Demoment 1989 - and references therein). In order to construct a reliable object, structural information is needed concerning the sought object. Solutions are brought by restricting the class of admissible solutions given suitable informations. A widely used and powerful framework for this task is the *regularization* one. This tool accounts for foreknown informations about the sought objects, in order to compensate, at least partially, the lack of information provided by the data.

Accounting for model and data

Observed data y and mathematical model H are taken into account by means of a measure of discrepancy between observed data y and model output $H(x)$. The most simple choice for this measure is a quadratic distance, *i.e.* a Least Square (LS) criterion (Sorenson 1980):

$$Q_{\mathrm{LS}}(x) = \| \, y - H(x) \, \|^2 \, . \tag{B.1}$$

The usual fitting procedure, often used in experimental data processing, yields the LS estimate :

$$\hat{x}_{\mathrm{LS}} = \arg\min_x Q_{\mathrm{LS}}(x) \, . \tag{B.2}$$

Accounting for prior information

As mentioned above, a commonly used way of dealing with ill-posedness is the regularization framework which consists in accounting for available prior information. This can be achieved by means of at least three strategies : *penalization*, *constraint* or *re-parameterization*. Moreover, a combination of these strategies is clearly possible if needed.

Penalization — A penalized form yields a regularized least squares criterion :

$$Q_{\mathrm{RLS}}(x) = Q_{\mathrm{LS}}(x) + \alpha \, \varphi(x) \tag{B.3}$$

where $\varphi(x)$ measures a discrepancy to a prior information. Such a criterion strikes a compromise between information provided by the data and prior information. The hyperparameter, namely α, controls the trade off between the two sources of information.

Constraint — A constrained approach yields another class of optimization problem :

$$\min_x Q_{\mathrm{LS}}(x) \qquad \text{s.t.} \quad x \in \mathcal{D} \, , \tag{B.4}$$

that is a constrained optimization problem (s.t. stands for “subject to”). The set $\mathcal{D}$ must be specified according to the context. For example, if the sought object is a light flux or an energy, hence positive, a natural choice reads $\mathcal{D} = \mathbb{R}_+^P$.

Re-parameterization — Information can also be accounted for by means of a new parameterization, such as $x = x(\theta)$ of the sought object. Parameter θ can then be estimated in a LS framework.

Optimization stage

The key property in numerous optimization problem is *convexity* (Bertsekas 1995). Under such assumption a unique global minimum exists for the previously proposed criterion. Moreover, the global minimizer can be reached by means of classical optimization methods such as gradient or coordinatewise descent algorithm. Unfortunately, the model at work in our context is a non-linear one and convexity property will not be ensured. As a consequence, no guarantee of global minimization will be provided.

Appendix C

C.1 Implementation of the dynamic calibration method in PIA

C.1.1 Program to fit Chebyshev polinomials to a given measurement

```
c
c This program reads ASCII data file, containing PHT-S spectra from
c calibration stars.
c It computes all Chebyshev expansion within a range of terms.
c It will produce a file containing the coefficients for all polynomials
c and the normalization values.
c It calls routine E02ADF from the NAG library. The program should be
c compiled with the option -lnag
c
c

character nom*20,fich*30, admn*20
integer ifail,grmax,grado,grmin,npt
real*8 x(1000),yp(1000),w(1000),w1(3000),w2(42),tol0
real*8 a(21,21),s(21)
real y(1000,128)
c external hand
c integer ieee.handler,hand,ieee.flags

c i=ieee.handler('set','common',hand)
open(0,file='errores')
grmax=30
do while (grmax.lt.1.or.grmax.gt.20)
print*,'Minimum and maximum degree for fitting: '
read (*,*) grmin,grmax
enddo
c grmax=20
c grmin=4
tol0=2d-2
do i=1,1000
w(i)=1d0
enddo

print*,'Input list file: '
read (*,'(a)') nom
```

```
open (1,file=nom,status='old')

do while (.true.)
 read (1,'(a)',end=1) nom
 open(2,file=nom,status='old')
 n2 = index(nom,'.dat')-1
 print*,nom(1:n2)
 read (2,*) admn

c Store all coef in a file

write(fich, '("cheb.",a,".coef")') nom(1:n2)
print*,fich
     open(100, file=fich)

npt=0
do while (.true.)
 read (2,*,end=2) x(npt+1),(y(npt+1,i),i=1,128)
 npt=npt+1
 enddo
2 print*,'read file ',nom,' with ',npt,' points'
 if (npt-2.ge.grmin) then

 grado=min(npt-2,grmax)
 write(100,'(a)') admn
 write(100,'("Npts",i5," t1= ",f7.3," t2= ",f7.1," Degree min=",i2,", max=",i2 )'),npt,x(1),x(npt),grmin,grmax

do j=1,128

 do k=1,npt
yp(k)=dble(y(k,j))
 enddo

 ifail=0
 call e02adf (npt,grado+1,21,x,yp,w,w1,w2,a,s,ifail)
 if (ifail.ne.0) then
print*,'ifail= ',ifail
stop
 endif

         write(100,'("Pixel ",i3)') j
c print*,s(1),s(2),(a(1,m),m=1,2)
  do l=grmin, grmax
   write(100,'(d13.4,2x,21(d17.9,1x))') s(l+1), (a(l+1,m),m=1,l+1)
  enddo

 enddo
 else
  print*,'There is no enough points for fitting'
 endif
```

```
 close (100)
enddo | close loop of files
1 continue
end
```

C.1.2 Program to select best Chebyshev polinomials to a given measurement

```
c This program selects the best Chebyshev polynomial expansion to
c a given measurement. The minimum degree of the polynomial expansion
c which has deviation (RMS) less than the noise of the data.
c The noise of the data is computed from the difference between consecutive
c signals.

character nom*100,fich*30
real y(1000,128),x(1000),xmin,xmax,volts(6)
real*8 rms,coef(21),xc,fit
integer grmin,grmax,grado
open(0,file='errores')

print*,'List file: '
read (*,'(a)') nom
open (1,file=nom,status='old')

print*,'Output file: '
read (*,'(a)') nom
open (20,file=nom)

do while (.true.)
 read (1,'(a)',end=1) nom
 open(2,file=nom,status='old')
 read(2,'(4x,i5,5x,f7.3,5x,f7.1,11x,i2,6x,i2)')
         : npt,xmin,xmax,grmin,grmax
 n1=index(nom,'.')+1
 n2=index(nom,'.')-1
 open(3,file=nom(n1:n2)//".dat",status='old')
 do i=1,npt
  read (3,*) x(i),(y(i,l),l=1,128)
 enddo
 write (20,*) 'Read file ',nom(n1:n2),' with ',npt,' pts'

 do i=1,128
c
c Computation of noise for pixel i
c

 ruidom=0
 do j=2,npt
  ruidom=ruidom+y(j,i)-y(j-1,i)
 enddo
```

```
 ruidom=ruidom/real(npt-1)
 ruido=0
 do j=2,npt
  ruido=ruido+(y(j,i)-y(j-1,i)-ruidom)**2
 enddo
 ruido=sqrt(ruido/real(npt-1))
c
c Look for polynomial expansion where the RMS is less than data noise
c

 read(2,'(a)')
 rms=2*ruido
 grado=grmin
 do while (rms.gt.1d-10.and.rms.gt.1.414*ruido.and.grado.le.grmax)
  read(2,*) rms,(coef(l),l=1,grado+1)
grado=grado+1
  enddo
  grado=grado-1
c print*,'Pixel: ',i,' Degree: ',grado,' RMS: ',rms,' Noise: ',ruido
 write (fich,'("phts.",i3.3,".mod")') i
 open (30,file=fich)
 do while (.true.)
read (30,'(a)',end=3)
 enddo
3 do k=1,6
volts(k)=-99
xr=16*2**(k-1)
if (xr.le.xmax) then
 xc=((xr-xmin)-(xmax-xr))/(xmax-xmin)
 ifail=0
 call e02aef (grado+1,coef,xc,fit,ifail)
if (ifail.ne.0) then
print*,'ifail= ',ifail
stop
endif
volts(k)=real(fit)
endif
  enddo
  write (30,'(a,i4.3,6e14.6,2f9.3,i3,21d17.9)')
    : nom(n1:n2),i,volts,xmin,xmax,grado,(coef(l),l=1,grado+1)
  close (30)

  do l=1,grmax-grado
   read(2,*) rms
  enddo
 enddo
enddo
1 continue
end
```

Appendix D

D.1 Documentation

D.1.1 Technical Reports/Papers

Most of the contents of this WG Final Report have been extracted from the documents listed below. Internal Technical Reports are available upon request contacting the ISO Helpdesk at *helpdesk@iso.vilspa.esa.es.*

Transient response of IR detectors used in space astronomy: what we have learned from ISO satellite by A. Coulais et al. presented at the SPIE 45th Annual Meeting, July 30th - August 4th 2000, San Diego (California, USA)

Optimizing ISOCAM data processing using spatial redundancy by M.-A. Miville-Deschenes, F. Boulanger, A. Abergel and J.-P. Bernard (A&AS 2000, 146, 519)

The transient behaviour of the long wavelength channel of ISOCAM by A. Abergel et al. (ExA 2000, 10, 353)

Transient correction of the LW-ISOCAM data for low contrast illumination by A. Coulais & A. Abergel (A&AS 2000, 141, 533)

A modified IAS model for the ISOCAM LW transient correction by F.-X Desert (March 1999)

Modelling transients effects in the IR array of the Short Wavelength channel of ISOCAM, the camera onboard the ISO satelllite by D. Tiphène et al. (March 1999)

Dynamical calibration for ISOPHOT-s by J. Acosta (March 1999)

Transients effects in ISOPHOT data: status of modelling and correction procedures by J. Acosta et al. (April 1999)

Memory Effects and their Correction in SWS Si:Ga detectors by D. Kester (November 2000)

Long term performance of doped Ge:Ga photoconductors in the space environment by T.Lim et al., presented at the SPIE Annual Meeting - 1998 - 3354, 347

D.1.2 Relevant contributions presented at the ISO Calibration Legacy Conference

Below there is a list of papers that were presented at the Conference held at VILSPA ISO on *The Calibration Legacy of the ISO Mission* (February 5-9, Madrid) which we consider relevant to the activities carried out by this Transients WG.

- *Physical approach to the problems of space low-background detectors* by B. Fouks
- *Properties of Germanium photoconductor detectors* by E. Young
- *What can be characterized for low Background IR Detectors from ground based experiments?* by A. Coulais et al.
- *SWS transients effects: models and corrections* by D. Kester et al.
- *Transient effects correction for LWS detectors* by E. Caux
- *A simple approach to transient correction in ISO LWS data* by C. Lloyd
- *Transient Correction for ISOPHOT C-100 Detectors* by A. Coulais et al.
- *Current status of modelization of point source transient response for LW-ISOCAM* by A. Coulais & B. Fouks
- *Optimizing ISOCAM data processing using spatial redundancy* by M.-A. Miville-Deschênes
- *Analysis of ISOPHOT Chopped Observations* by P. Ábrahám & J. Acosta-Pulido
- *Laboratory Measurements of Transient Behavior of Stressed Ge:Ga Detectors* by H. Kaneda

D.1.3 A bibliographic database on 'Transients in IR detectors'

(see next pages)

Bibliographic Database about transients in IR detectors

A. Coulais

March 7, 2000

References

[1] A. Abergel and A. Coulais, *New method to correct ISOCAM-LW transient effects : first results*, tech. rep., IAS Lab., Septembre 1998.

[2] A. Abergel, F. X. Desert, and H. Aussel, *Ias model for ISOCAM LW transient correction*, technical report, Décembre 1996.

[3] A. Abergel et al., *ISOCAM mapping of the ρ-Ophiuchi main cloud.*, Astron. Astrophys., 315:L329–L332, Novembre 1996.

[4] A. Abergel, M. A. Miville-Deschêne, F. X. Désert, M. Pérault, H. Aussel, and M. Sauvage, *IAS model for ISOCAM LW transient correction*, accepted in Experimental Astronomy, Février 1999.

[5] A. Abergel and M. Pérault, *Flight model LW channel : noise due to transients*, tech. rep., IAS lab., Juin 1994.

[6] J. A. Acosta-Pulido, C. Gabriel, and H. O. Castañeda, *Transient effects in ISOPHOT data: status of medelling and correction procedures*, tech. rep., ESA, 1998.

[7] P. Agnèse, J. J. Engelmann, and P. Mottier, *Results of radiation tests performed on the ISOCAM infrared detector array*, IEEE Trans. on Nuclear Science, 38:953–963, Août 1991.

[8] P. Agnèse, C. Lucas, P. Maillart, P. L. Mottier, Y. Lepennec, and P. Masse, *ISOCAM camera long-wavelength channel detector*, Proceedings of SPIE, 1070:124–128, Juillet 1989.

[9] A. Biviano et al., *The ISOCAM dark current calibration report*, tech. rep., ISOCAM, Novembre 1998.

[10] A. Biviano et al., *The ISOCAM flat field calibration report*, tech. rep., ISOCAM, Novembre 1998.

[11] I. Blokhin, V. V. Osipov, and I. I. Taubkin, *Coordinate dependence of photosensitivity and other pecularities of extrinsic photoconductor detectors at low backgrounds*, Infrared Physics, 33(1):9–26, 1992.

[12] J. Blommaert, *ISOCAM photometry report*, tech. rep., ESA Vilspa, Spain, Mai 1998.

[13] S. Bouaissi, *étude des différents modèles de phénomènes transitoires sur le satellite ISO*, tech. rep., Stage de license, 1999.

[14] N. Bourot, *Imagerie en astronomie : correction des transitoires de la caméra ISOCAM*, tech. rep., Stage de magistère, 1998.

[15] C. J. Cesarsky, *ISOCAM*, in Infrared Astronomy with ISO. L'astronomie infrarouge et la mission ISO., T. Encrenaz and M. Kessler, eds., Les Houches, France, June 13-27, 1991, Nova Science, Commack, N.Y., 1992, pp. 31–50.

[16] C. J. Cesarsky et al., *ISOCAM in flight.*, Astron. Astrophys., 315:L32–L37, Novembre 1996.

[17] S. E. Church, M. J. Griffin, P. A. R. Ade, M. C. Price, R. J. Emery, and B. M. Swinyard, *Performance testing of doped-germanium photoconductors for the ISO long wavelength spectrometer*, in ESA SP-356 Photon Detectors for Space Instrumentation, Décembre 1992, pp. 255–260.

[18] S. E. Church, M. J. Griffin, M. C. Price, P. A. Ade, R. J. Emery, and B. M. Swinyard, *Performance characteristics of doped-Ge photoconductors for the Infrared Space Observatory Long Wavelength Spectrometer*, Proceedings of SPIE, 1946:116–125, Octobre 1993.

[19] S. E. Church, M. C. Price, M. J. Griffin, P. A. R. Ade, R. J. Emery, and B. M. Swinyard, *Non-linear effects in doped-germanium photoconductors for the ISO long wavelength spectrometer*, in ESA SP-356 Photon Detectors for Space Instrumentation, Décembre 1992, pp. 261–264.

[20] S. E. Church, M. C. Price, N. M. Haegel, M. J. Griffin, and P. A. R. Ade, *Transient response in doped germanium photoconductors under very low background operation*, Applied Optics, 35:1597–1604, 1996.

[21] A. Coulais, *Étude des équations de Fouks*, tech. rep., IAS lab., Octobre 1998.

[22] A. Coulais, *État de l'étude des transitoires LW-ISOCAM sous fort gradient d'illumination*, tech. rep., IAS lab., Mai 1999.

[23] A. Coulais and A. Abergel, *Transient correction of the ISOCAM data with the Fouks-Schubert model: first results*, tech. rep., IAS Lab., Septembre 1998.

[24] A. Coulais and A. Abergel, *Transient correction of the LW-ISOCAM data with the Fouks-Schubert model : first results*, in ISO Conference, Paris, ESA, ESA, Octobre 1998.

[25] A. Coulais and A. Abergel, *Correction des transitoires de la caméra infrarouge du satellite ISO*, GRETSI'99, Septembre 1999.

[26] A. Coulais and A. Abergel, *Transient correction of the LW-ISOCAM data for low contrasted illumination*, Astron. Astrophys. Suppl. Ser., 141, Février 2000.

[27] C. J. Delattre, *About transients, the fitting method*, technical report, Juillet 1996.

[28] C. Delettrez, M. J. Griffin, C. Le Naour, S. Church, and J. Chabaud, *The detector signal processing chain of the ISO Long Wavelength Spectrometer*, Experimental Astronomy, 4:213–235, 1994.

[29] F.-X. Désert, *A modified IAS model for ISOCAM LW transient correction*, tech. rep., LAOG, Mars 1999. Version 2.0.

[30] F. X. Désert, J. L. Puget, D. L. Clements, M. Pérault, A. Abergel, J. P. Bernard, and C. J. Cesarsky, *A classical approach to faint extragalactic source extraction from ISOCAM deep surveys. Application to the Hubble Deep Field*, Astron. Astrophys. Suppl. Ser., 342:363–377, Février 1999.

[31] G. G. Fazio, J. L. Hora, S. P. Willner, J. R. Stauffer, M. L. Ashby, Z. Wang, E. V. Tollestrup, J. L. Pipher, W. J. Forrest, C. R. McCreight, S. H. Moseley, W. F. Hoffmann, P. Eisenhardt, and E. L. Wright, *Infrared array camera (IRAC) for the Space Infrared Telescope Facility (SIRTF)*, Proceedings of SPIE, 3354:1024–1031, Août 1998.

[32] A. M. Filachev, B. I. Fouks, and D. Greenfeld, *Nature of distortions of the surface pattern produced by precise electron-beam processing of insulators*, Proceedings of SPIE, 3155:78–88, Septembre 1997.

[33] B. I. Fouks, *Injection properties of contacts to high-resistivity semiconductors. I*, Sov. Phys. Semicond., 15(9):974–980, Septembre 1981.

[34] B. I. Fouks, *Injection properties of contacts to high-resistivity semiconductors. II*, Sov. Phys. Semicond., 15(9):980–986, Septembre 1981.

[35] B. I. Fouks, *Nonstationary behaviour of low background photon detectors*, in ESA SP-356 Photon Detectors for Space Instrumentation, Décembre 1992, pp. 167–174.

[36] B. I. Fouks, *Nonstationary processes in extrinsic photoconductors*, Proceedings of SPIE, 1762:519–530, Janvier 1993.

[37] B. I. Fouks, *Problems of operation of low-background IR detectors*, Proceedings of SPIE, 2553:489–500, Septembre 1995.

[38] B. I. Fouks, *Active modes of operation of low-background extrinsic IR detectors*, Proceedings of SPIE, 2790:38–46, Avril 1996.

[39] B. I. Fouks, *Phenomena in low-background IR detectors under high-energy particles*, Proceedings of SPIE, 2817:160–171, Octobre 1996.

[40] B. I. Fouks, *Theory of photoresponse of low-background IR detectors*, Proceedings of SPIE, 3122:441–452, Octobre 1997.

[41] B. I. Fouks, V. F. Kocherov, I. I. Taubkin, L. A. Vinokurov, and N. B. Zaletaev, *Photoelectric cross talk between the elements of an extrinsic photoconductor detector array at low backgrounds*, Proceedings of SPIE, 2269:727–735, Octobre 1994.

[42] B. I. Fouks, V. F. Kocherov, I. I. Taubkin, L. A. Vinokurov, and N. B. Zaletaev, *Photoresponse of low-background extrinsic infrared detector arrays*, Optical Engineering, 33:1485–1491, Mai 1994.

[43] B. I. Fouks and J. Schubert, *Precise theoretical description of photoresponse for detectors of ISOPHOT's Si:Ga array*, Proceedings of SPIE, 2475:487–498, Juin 1995.

[44] M. Fujiwara, N. Hiromoto, and K. Araki, *Moderate-fast transient response of the Ge:Ga photoconductors*, Proceedings of SPIE, 2552:421–429, Septembre 1995.

[45] K. Ganga, G. Helou, R. Hurt, M.-S. Kong, J. Li, E. Valjavec, and D. Van Buren, *ISO/CAM transient removal at IPAC*, tech. rep., IPAC Lab., Août 1998.

[46] K. Ganga, M. Kong, L. Jing, and D. Van Buren, *Transient removal with the IPAC method*, tech. rep., IPAC Lab., Juillet 1998.

[47] U. Groezinger, S. Kirches, D. Lemke, J. Schubert, B. Schulz, and J. Wolf, *Characterization of detectors and calibration of the ISOPHOT experiment*, in ESA SP-356 Photon Detectors for Space Instrumentation, Décembre 1992, pp. 329–333.

[48] N. Haegel, J. W. Beeman, P. N. Luke, and N. Haller, *Transient photoconductivity in Ge:Be due to Be^+ formation*, Physical Review B, 39(6):3677–3682, Février 1989.

[49] N. Haegel, C. Brennan, and A. White, *Transport in extrinsic photoconductors: a comprehensive model for transient response*, Journal of Applied Physics, 80(3):1510–1514, Août 1996.

[50] N. Haegel, C. Latasa, and A. White, *Transient response of infrared photoconductors : the roles of contacts and space charge*, Applied Physics, A 56:15–21, 1993.

[51] N. Haegel, C. Newton, J. Simoes, and A. White, *Modeling of transient response in far infrared photoconductors*, in Submillimeter and far infrared space instrumentation, 30th ESLAB Symp, ed., no. SP-388, ESTEC, Décembre 1996, ESA, ESA, pp. 15–20.

[52] N. Haegel, J. Simoes, A. White, and B. J.W., *Transient behavior of infrared photoconductors: application of a numerical model*, Applied Optics, 38(10):1910–1919, Avril 1999.

[53] N. Haegel and A. White, *Modeling of near-contact field and carrier distributions in extrinsic germanium photoconductors*, Infrared Physics, 29(5):915–923, 1989.

[54] N. Hiromoto, T. Itabe, H. Shibai, H. Matsuhara, T. Nakagawa, and H. Okuda, *Three-element stressed Ge:Ga photoconductor array for the infrared telescope in space*, Applied Optics, 31:460–465, Février 1992.

[55] IPAC group, *ISOCAM transient treatment at IPAC*, tech. rep., IPAC Lab., 1997.

[56] M. F. Kessler et al., *The Infrared Space Observatory (ISO) mission.*, Astron. Astrophys., 315:L27–L31, Novembre 1996.

[57] C. Lari, *IRA model for ISOCAM LW transient correction*, tech. rep., IRA, Juin 1997.

[58] M.-A. Miville-Deschênes, F. Boulanger, A. Abergel, and J.-P. Bernard, *Original data processing for ISOCAM raster imaging of extended emission.* accepted in A&A, 1999.

[59] A. Moneti, ed., *ISO detector workshop, viewgraphs of the presentations, 14–16 Jan.*, vol. I–II, Villafranca del Castillo, 1998, ESA.

[60] P. Mottier, P. Agnese, and P. O. Lagage, *Si:Ga focal plane arrays for satellite and ground-based telescopes*, Proceedings of SPIE, 1494:419–426, Septembre 1991.

[61] P. Mottier, C. Lucas, M. Ravetto, and P. Agnese, *Recent developments on ISOCAM long wavelength channel detector*, Proceedings of SPIE, 1341:368–374, Novembre 1990.

[62] K. Okumura, *ISOCAM PSF report*, tech. rep., ESA, Vilspa, Juin 1998.

[63] A. I. Patrashin and G. A. Ivanov, *Testing unit for measuring photoelectric characteristics of IR arrays*, Proceedings of SPIE, 3379:555–560, Juillet 1998.

[64] M. Patrashin, B. Fouks, U. Grozinger, D. Lemke, and J. Wolf, *Residual conductivity of stressed Ge:Ga photoconductors after low-dose gamma irradiation*, Journal of Applied Physics, 82(3):1450–1453, Août 1997.

[65] M. A. Patrashin, B. I. Fouks, D. Lemke, and J. Wolf, *Radiation-induced effects in extrinsic far-infrared detectors*, Proceedings of SPIE, 2475:476–486, Juin 1995.

[66] M. A. Patrashin, M. Fujiwara, N. Hiromoto, and B. I. Fouks, *Far-infrared Ge:Ga detector for low-background space-based astronomical observations*, Proceedings of SPIE, 3354:232–239, Août 1998.

[67] M. Pérault, F. X. Desert, A. Abergel, F. Boulanger, C. Dupraz, A. Soufflot, C. J. Cesarsky, and L. G. Vigroux, *Infrared Space Observatory camera calibration facility and preflight characterization*, Optical Engineering, 33:762–770, Mars 1994.

[68] W. Press, S. Teukolsky, W. Vetterling, and B. Flannery, *Numerical Recipes in* `FORTRAN`*, second edition*, Cambridge University Press, 1992.

[69] J. Schubert, *Die Eichung des Infrarot-Gitterspektrometers im Satelliten-Experiment ISOPHOT und die Korrektur der Transienten seiner Detektoren*, PhD thesis, Max Planck-Institut für Astronomie, Heidelberg, 1995.

[70] J. Schubert, B. I. Fouks, D. Lemke, and J. Wolf, *Transient response of ISOPHOT Si:Ga infrared photodetectors: experimental results and application of the theory of nonstationary processes*, Proceedings of SPIE, 2553:461–469, Septembre 1995.

[71] J. Schubert, G. Roth, J. Wolf, D. Lemke, and B. I. Fouks, *Correction and curing of in-orbit-induced nonideal behavior of ISOPHOTS's photodetectors*, Proceedings of SPIE, 2268:283–294, Septembre 1994.

[72] N. Sclar, *Properties of doped silicon and germanium infrared detectors*, Prog. Quant. Electr., 9:149–257, 1984.

[73] J. See, *correction des effets mémoire de l'instrument ISOPHOT C-100*, tech. rep., Stage de magistère, 1999.

[74] M. Sheinkman and A. Y. Shik, *Long-term relaxation and residual conductivity of semiconductors (review)*, Sov. Phys. Semicond., 10(2):128–143, Février 1976.

[75] R. Siebenmorgen et al., *First results from the ISOCAM parallel mode*, Astron. Astrophys., 315:L169–L172, Novembre 1996.

[76] R. Suris and B. I. Fouks, *Theory of transient processes in compensated semiconducteurs. I*, Sov. Phys. Semicond., 12(12):1380–1384, Décembre 1978.

[77] R. Suris and B. I. Fouks, *Theory of transient processes in compensated semiconducteurs. II*, Sov. Phys. Semicond., 13(1):79–86, Janvier 1979.

[78] R. Suris and B. I. Fouks, *Noise in finite compensated semiconductors. I. Generation-recombinaison noise*, Sov. Phys. Semicond., 14(6):641–646, Juin 1980.

[79] R. Suris and B. I. Fouks, *Noise in finite compensated semiconductors. II. johnson noise and contact noise*, Sov. Phys. Semicond., 14(6):647–652, Juin 1980.

[80] R. Suris and B. I. Fouks, *Theory of nonlinear processes in compensated semiconducteurs*, Sov. Phys. Semicond., 14(8):896–901, Août 1980.

[81] B. Swinyard, P. Clegg, S. Leeks, M. Griffin, T. Lim, and M. Burgdorf, *Space operation and performance of doped germanium photoconducting detectors in the far infrared: experience from the ISO LWS*, tech. rep., ESA, 1998.

[82] S. Teitsworth, B. A. Lynn, and R. Westervelt, *Chaotic dynamics in a simple model of extrinsic photoconductors*, Physical review letters, T 14:71–75, 1986.

[83] S. Teitsworth and R. Westervelt, *Chaos and broadband noise in extrinsic photoconductors*, Physical review letters, 53(27):2587–2590, Décembre 1984.

[84] D. Tiphène, D. Rouan, G. Epstein, and P. Le Coupanec, *Modelling transient effects in the IR array of the short wavelength channel of ISOCAM, the camera onboard the ISO satellite*, accepted in Experimental Astronomy, Mai 1999.

[85] L. G. Vigroux, C. J. Cesarsky, O. Boulade, Y. Rio, M. Perault, A. Abergel, F. X. Desert, D. Rouan, and F. Lacombe, *ISOCAM–the Infrared Space Observatory camera: results of testing and calibrations*, Proceedings of SPIE, 1946:281–292, Octobre 1993.

[86] L. A. Vinokurov and B. I. Fouks, *Spreading of the current in a photosensitive medium exhibiting an extrinsic photoconductivity*, Sov. Phys. Semicond., 22(11):1258–1262, Novembre 1988.

[87] L. A. Vinokurov and B. I. Fouks, *Nonlinear photoresponse of extrinsic photoconductors*, Sov. Phys. Semicond., 25(11):1207–1211, Novembre 1991.

[88] L. A. Vinokurov, N. B. Zaletaev, V. F. Kocherov, and B. I. Fouks, *Spreading of time dependent photocurrrent in Si:Ga*, Sov. Phys. Semicond., 26(4):433–435, Avril 1992.

[89] J. W. Wensink, W. Luinge, D. Beintema, E. A. Valentijn, T. Degraauw, R. Katterloher, L. Barl, and E. T. Young, *Characteristics of the ISO short wavelength spectrometer detectors*, in ESA SP-356 Photon Detectors for Space Instrumentation, Décembre 1992, pp. 339–344.

[90] R. Westervelt and S. Teitsworth, *Nonlinear transient response of extrinsic Ge far-infrared photodetectors*, Journal of Applied Physics, 57(2):5457–5469, Juin 1985.

[91] A. M. White, *The characteristics of monority-carrier exclusion in narrow direct gap semoconductors*, Infrared Physics, 26(6):729–741, 1985.

[92] J. Wolf, *Low-background far-infrared detectors and arrays*, Optical Engineering, 33(5):1492–1500, Mai 1994.